

**MEASUREMENT OF MULTIJET CROSS-SECTION RATIOS
IN PROTON-PROTON COLLISIONS WITH THE CMS
DETECTOR AT THE LHC**

A THESIS

**Submitted to the
FACULTY OF SCIENCE
PANJAB UNIVERSITY, CHANDIGARH
for the degree of**

DOCTOR OF PHILOSOPHY

2018

ANTERPREET KAUR

**DEPARTMENT OF PHYSICS
CENTRE OF ADVANCED STUDY IN PHYSICS
PANJAB UNIVERSITY
CHANDIGARH, INDIA**

*Dedicated to
my Parents*

Acknowledgement

I would like to take this opportunity to thank the many people who helped make this dissertation possible.

In the first and foremost place, I gratefully express my sincere gratitude to my supervisor Prof.(Mrs.) Manjit Kaur for her invaluable assistance, support, guidance and blessings. She inspired me greatly to work in this project. Her willingness to motivate me contributed tremendously to this project.

I am highly obliged to Prof. C.S. Aulakh Chairperson of the Department of Physics, Panjab University, Chandigarh, for his helping hand in providing a good environment and adequate facilities to complete this project successfully.

I feel deeply indebted to my parents for their unconditional love, understanding, support, strength, blessings and for everything.

I am greatly thankful to my well wishers, my friends Anu, Sohail, Junaid, Mandeep and my classmates for all that they meant to me during the crucial times of the completion of my project.

I owe my very special thanks to Mr. Inderpal Singh, Mrs. Prabhdeep Kaur, Mrs. Manuk Z. Mehta, Ms. Ritu Aggarwal, Ms. Ruchi Gupta, Ms. Monika Mittal and Ms. Genius, the members of high energy physics Laboratory, Dept. of Physics, P.U. for helping me out from all kinds of problems with their constant support, suggestions and encouragement.

Finally and the most importantly, I would like to pay my greatest regards to the Almighty God for His blessings and kindness, a boundless and an endless source of inspiration for me always.

Abstract

The hadrons colliding at very high center-of-mass energies provide a direct probe to the nature of the underlying parton-parton scattering physics. The scattering of the elementary quarks and gluons, constituents of the incoming hadron beams, produces a high momentum partons which then fragment and hadronize producing a spray of particles. These particles get clustered in the form of jets. The jets being the final structures observed in the detector, preserve the energy and direction of the initial partons. Hence jets can serve as a direct test of theory of strong interactions called Quantum Chromodynamics. The inclusive multijet production cross-section is an important observable which provides the details of parton distribution functions of the colliding hadrons and the precise measurement of the strong coupling constant α_S . Instead of individual cross-sections, the ratio of cross-sections is a better tool to determine the value of α_S as many theoretical and experimental uncertainties cancel in the ratio.

A measurement of inclusive multijet event cross-sections and the cross-section ratio is presented using data from proton-proton collisions collected with the CMS detector at a center-of-mass energy of 8 TeV corresponding to an integrated luminosity of 19.7 fb^{-1} . Jets are reconstructed with the anti- k_t clustering algorithm for a jet size parameter $R = 0.7$. The inclusive 2-jet and 3-jet event cross-sections as well as the ratio of the 3-jet over 2-jet event cross-section (R_{32}) are measured as a function of the average transverse momenta p_T of the two leading jets in a phase space region ranging up to jet p_T of 2.0 TeV and an absolute rapidity of $|y| = 2.5$. The measurements after correcting for detector effects are well described by predictions at next-to-leading order in perturbative quantum chromodynamics and additionally are compared to several Monte Carlo event generators. The strong coupling constant at the scale of the Z boson mass is extracted from a fit of the measured R_{32} which gives $\alpha_s(M_Z) = 0.1150 \pm 0.0010 \text{ (exp)} \pm 0.0013 \text{ (PDF)} \pm 0.0015 \text{ (NP)} {}^{+0.0050}_{-0.0000} \text{ (scale)}$ using MSTW2008 PDF set. The current measurement agrees well with the world

average value of $\alpha_s(M_Z) = 0.1181 \pm 0.0011$ as well as previous measurements.

Contents

List of Figures	xv
List of Tables	xxi
<hr/>	
1 Introduction	1
2 Theoretical Background	5
2.1 Standard Model	5
2.2 Quantum Chromodynamics	8
2.2.1 Perturbative Quantum Chromodynamics	12
2.2.2 Renormalization and Running of the Strong Coupling	14
2.3 Hadronic Collisions	16
2.3.1 Parton Shower and Hadronization	19
2.3.2 Underlying Event	21
2.4 Jets	23
2.4.1 Jet Algorithms	24
3 Experimental Setup	29
3.1 The Large Hadron Collider	30
3.1.1 Luminosity Measurement	32

3.1.2	Pileup Interactions	34
3.2	The Compact Muon Solenoid	35
3.2.1	Coordinate System	38
3.2.2	Inner Tracker System	39
3.2.3	Electromagnetic Calorimeter	42
3.2.4	Hadronic Calorimeter	43
3.2.5	Superconducting Magnet	46
3.2.6	Muon System	47
3.2.7	Trigger and Data Acquisition System	49
3.2.7.1	Jet Triggers	51
3.2.7.2	Data Acquisition System	52
3.2.8	Data Management	52
3.3	Software Tools	53
3.3.1	CMSSW Framework	54
3.3.2	ROOT	54
3.3.3	NLOJET++ and FASTNLO	55
4	Event Generation, Simulation and Reconstruction	57
4.1	Event Generation and Simulation Software	57
4.1.1	PYTHIA	59
4.1.2	MADGRAPH5	59
4.1.3	HERWIG	60
4.1.4	POWHEG	60
4.2	Detector Simulation	60
4.3	Event Reconstruction	62
4.3.1	Particle Flow Algorithm	64

4.3.2	Jet Energy Corrections	66
5	Measurement of the Differential Inclusive Multijet Cross-sections and their Ratio	69
5.1	Data Samples	70
5.1.1	Monte Carlo Samples	71
5.2	Event Selection	72
5.2.1	Trigger Selection	72
5.2.2	Primary Vertex Selection	74
5.2.3	Missing Transverse Energy	76
5.2.4	Jet Identification	77
5.2.4.1	Jet ID Efficiency	78
5.2.5	Jet Selection	81
5.3	Comparison with Simulation	82
5.3.1	Pileup Reweighting	82
5.3.2	Comparison of Cross-sections and their Ratio	82
5.4	Jet Energy Resolution (JER)	85
5.5	Unfolding	90
5.5.1	Response Matrices	92
5.5.1.1	Inclusive Cross-sections	92
5.5.1.2	Cross-section Ratio, R_{32}	95
5.5.2	Closure Test	96
5.5.3	Unfolding of the Measurement	98
5.6	Experimental Uncertainties	99
5.6.1	Statistical Uncertainty	100
5.6.2	Jet Energy Corrections Uncertainty	101

5.6.3	Unfolding Uncertainty	104
5.6.4	Luminosity Measurement Uncertainty	105
5.6.5	Residual Uncertainty	106
5.6.6	Total Experimental Uncertainty	106
6	Theoretical Calculations	109
6.1	Fixed Order NLO Calculations	109
6.1.1	NLO Correction Factors	111
6.1.2	Non-perturbative Corrections	112
6.1.3	Electroweak Corrections	114
6.2	Theoretical Uncertainties	116
6.2.1	Scale Uncertainty	116
6.2.2	PDF Uncertainty	117
6.2.3	Non-perturbative Uncertainty	118
6.2.4	Total Theoretical Uncertainty	118
6.3	Comparison of Theory to Data	120
7	Determination of the Strong Coupling Constant	125
7.1	Sensitivity of Measurements to $\alpha_s(M_Z)$	126
7.2	Determination of $\alpha_s(M_Z)$	127
7.2.1	Fitting Procedure	127
7.2.2	Fit Results	133
7.3	Running of the Strong Coupling Constant	136
8	Summary	141
Appendix A		145

A.1	Cross-section Ratio, R_{32}	146
A.2	Individual Sources of Jet Energy Correction Uncertainties	147
A.3	Experimental Uncertainties	150
A.4	Theoretical Uncertainties	153
	Bibliography	157
	List of Publications	173
	Reprints	201

List of Figures

2.1	The Standard Model summarizing the properties of elementary particles and their forces of interaction.	6
2.2	The fundamental Feynman rules for different processes of quantum chromodynamics.	11
2.3	The Feynman diagrams of leading-order (LO), next-to-leading order (NLO) and next-to-next-to-leading order (NNLO) processes in quantum chromodynamics.	13
2.4	Running of the strong coupling constant evolved at the energy scale Q as a function of Q	16
2.5	Schematic illustration of the factorization theorem in a collision of two protons.	18
2.6	Illustration of the hadronization process in Lund string model.	21
2.7	A proton-proton collision involving the main hard scattering process along with the low momentum transfer underlying event (UE) contributions.	22
2.8	Formation of a jet in a proton-proton collision.	24
2.9	Illustration of infrared and collinear unsafe behaviour of jet algorithms.	25
2.10	The clustering of particles into jets using different jet algorithms.	28

3.1	An overview of the different experiments of the Large Hadron Collider (LHC), a complex particle accelerator and collider located at CERN.	31
3.2	The integrated luminosity delivered by stable beams to CMS during proton-proton collisions.	34
3.3	In a proton-proton collision, the particles produced from the hard interaction are clustered into a jet. The hard interaction corresponds to the main vertex. The particles produced in the interactions other than the hard one, form a pileup jet.	35
3.4	The three dimensional view of the CMS detector along with its sub-detector components.	36
3.5	Front view of the CMS detector along with its various components. .	37
3.6	The right-handed coordinate system used by the CMS detector. . . .	38
3.7	A longitudinal view of the CMS detector is shown in the y - z plane. .	40
3.8	A longitudinal view of the inner tracking system is shown in r - z plane. .	41
3.9	A geometric view of one quarter of the electromagnetic calorimeter (ECAL) in y - z plane.	43
3.10	Longitudinal section of one quarter of the hadronic calorimeter (HCAL) in r - η plane.	45
3.11	A longitudinal view of the CMS muon system showing the location of the three gaseous particle detectors.	48
3.12	Work flow of the L1 trigger system consisting of local, regional and global components.	50
3.13	Architecture of the CMS Data Acquisition (DAQ) system.	52
3.14	The schematic overview of the CMS computing grid.	53

4.1	The comparison between Monte Carlo (MC) simulations generated by event generators and the real data produced by the collisions of observed in the detectors.	58
4.2	Formation of jets in a proton-proton collision at different levels.	63
4.3	The Particle Flow (PF) algorithm is used by the CMS to identify and reconstruct the particles. The PF converts the sub-detector measurements back to physical particle objects.	65
4.4	A schematic diagram of the factorized jet energy corrections (JEC).	66
5.1	Trigger efficiencies turn-on curves for the single jet HLT trigger paths. .	75
5.2	Missing transverse energy fraction of the total transverse energy per event in data and simulated Monte Carlo events.	77
5.3	The fractions of jet constituents for different types of PF candidates for inclusive 2-jet events.	79
5.4	The fractions of jet constituents for different types of PF candidates for inclusive 3-jet events.	80
5.5	The jet ID efficiency is studied as a function of $H_{\mathrm{T},2}/2$ with tag-and-probe technique using dijet event topologies and it always exceeds 99%.	81
5.6	Number of reconstructed vertices before and after the pileup reweighting.	83
5.7	Comparison of differential cross-sections for data with simulated events and CT10-NLO theory predictions.	84
5.8	Comparison of the cross-section ratio for data with simulated events and CT10-NLO theory predictions.	84
5.9	Fitting of the jet energy resolution distribution as a function of $H_{\mathrm{T},2}/2$. .	87

5.10 Comparison of jet energy resolution calculated using Crystal-Ball fit function and Gaussian fit function	88
5.11 Jet energy resolution (JER) is shown as a function of Gen $H_{T,2}/2$	88
5.12 Additional unfolding uncertainty.	90
5.13 Fitted CT10-NLO spectrum of differential cross-section as a function of $H_{T,2}/2$	94
5.14 The response matrices are derived using the Toy Monte Carlo and forward smearing method.	95
5.15 Left : The ratio of cross-sections for inclusive 3-jet to that of 2-jet events as a function of $H_{T,2}/2$. Right : The response matrix is derived using the Toy Monte Carlo and forward smearing method, for the cross-section ratio R_{32}	96
5.16 Closure test of the unfolding technique	97
5.17 Reco differential cross-section distributions unfolded with the response matrices.	98
5.18 The measured differential cross-sections as well as the cross-section ratio R_{32} are unfolded as a function of $H_{T,2}/2$ using the response matrices derived using the Toy Monte Carlo and forward smearing method.	99
5.19 The fractional statistical uncertainties of the unfolded data are compared with those of the measured one.	101
5.20 The unfolding procedure introduces the correlations of the statistical uncertainty through bin migrations.	102
5.21 Experimental uncertainties from different sources affecting the measurement of cross-sections and cross-section ratio.	107
6.1 The k-factors using five different PDF sets.	112

6.2	The nonperturbative (NP) corrections are presented as a function of $H_{T,2}/2$	114
6.3	The electroweak (EW) corrections as a function of $H_{T,2}/2$	115
6.4	Ratio of data over theory obtained using the CT10-NLO PDF set.	116
6.5	The systematic theoretical uncertainties affecting the cross-section measurement and the cross-section ratio.	119
6.6	Comparison of the measured differential inclusive 2-jet and 3-jet event cross-sections as a function of $H_{T,2}/2$ to theoretical predictions.	121
6.7	Cross-section ratio as a function of $H_{T,2}/2$ calculated from data in comparison to that from NLO pQCD predictions obtained using the CT10-NLO PDF set.	121
6.8	Ratio of data over theory using the CT10-NLO PDF set.	122
6.9	Ratio of data over the predictions from Monte Carlo simulations.	123
7.1	Ratio of the measured inclusive 2-jet differential cross-section to theory predictions using different PDF sets.	128
7.2	Ratio of the measured inclusive 3-jet differential cross-section to theory predictions using different PDF sets.	129
7.3	Ratio of the measured cross-section ratio to theory predictions using different PDF sets.	130
7.4	The running $\alpha_S(Q)$ as a function of the energy scale Q	139
A.1	The fractional jet energy correction (JEC) uncertainties from individual sources (Part I).	147
A.2	The fractional jet energy correction (JEC) uncertainties from individual sources (Part II).	148

A.3 The fractional jet energy correction (JEC) uncertainties from individual sources (Part III).	149
--	-----

List of Tables

5.1	Run range and luminosity of the proton-proton collisions data collected at the center-of-mass energy of 8 TeV by CMS experiment in the year of 2012 in four different run periods A, B, C and D.	71
5.2	The official Monte Carlo samples produced in phase space slices in H_T with the generator MADGRAPH5 and interfaced to PYTHIA6.	72
5.3	The single jet HLT trigger paths used in the analysis.	73
5.4	The jet ID removes noise and fake jets based on the properties of the reconstructed jets and the clustered particle candidates.	78
5.5	The jet energy resolution in data is actually worse than in simulation. To match the resolution in data, the reconstructed jet transverse momentum in simulated events need to be smeared by applying the scale factors.	86
5.6	The parameters obtained by fitting the relative resolution as a function of $H_{T,2}/2$	89
5.7	An overview of all experimental uncertainties affecting the measurement of cross-sections and the cross-section ratio.	108
6.1	NLO PDF sets available via LHAPDF6 with various assumptions on the value of $\alpha_s(M_Z)$	111

6.2	Overview of all systematic theoretical uncertainties affecting the measurement of cross-sections and the cross-section ratio.	120
7.1	Determination of $\alpha_s(M_Z)$ from the inclusive 2-jet and 3-jet event cross-sections using five PDF sets.	134
7.2	Determination of $\alpha_s(M_Z)$ from the inclusive 2-jet and 3-jet event cross-sections simultaneously and from their ratio R_{32} using five PDF sets.	134
7.3	Determination of $\alpha_s(M_Z)$ from the inclusive 2-jet event cross-section using five PDF sets at NLO without (left) and with (right) electroweak (EW) corrections.	135
7.4	Determination of $\alpha_s(M_Z)$ from the ratio R_{32} using the two most compatible PDF sets MSTW2008 and MMHT2014.	137
7.5	Determination of $\alpha_s(M_Z)$ from the ratio R_{32} in the $H_{T,2}/2$ range from 0.3 up to 1.68 TeV at the central scale and for the six scale factor combinations for the two PDF sets MSTW2008 and MMHT2014. . .	137
7.6	Uncertainty decomposition for $\alpha_s(M_Z)$ from the determination of α_S from the jet event rate R_{32} in bins of $H_{T,2}/2$	137
7.7	Evolution of the strong coupling constant.	139
A.1	Differential cross-sections ($\times 10^{-3}(\text{pb}/\text{GeV})$) and cross-section ratio R_{32} at detector level in each bin of $H_{T,2}/2$, along with statistical uncertainty (in %).	146
A.2	Experimental uncertainties (in %) affecting the cross-section measurement in each bin of $H_{T,2}/2$ for inclusive 2-jet events.	150
A.3	Experimental uncertainties (in %) affecting the cross-section measurement in each bin of $H_{T,2}/2$ for inclusive 3-jet events.	151

A.4 Experimental uncertainties (in %) affecting the cross-section measurement in each bin of $H_{\mathrm{T},2}/2$ for cross-section ratio.	152
A.5 Theoretical uncertainties (in %), calculated using CT10-NLO PDF set, affecting the cross-section measurement in each bin of $H_{\mathrm{T},2}/2$ for inclusive 2-jet events.	153
A.6 Theoretical uncertainties (in %), calculated using CT10-NLO PDF set, affecting the cross-section measurement in each bin of $H_{\mathrm{T},2}/2$ for inclusive 3-jet events.	154
A.7 Theoretical uncertainties (in %), calculated using CT10-NLO PDF set, affecting the measurement of cross-section ratio in each bin of $H_{\mathrm{T},2}/2$	155

Chapter 1

Introduction

Particle physics deals with the study of the basic constituents of matter and the forces governing the interactions among them. The Standard Model (SM) is the most accepted theory describing the nature and properties of the fundamental particles and their interactions. The elementary particles leptons and quarks, known as fermions, interact through the exchange of gauge bosons and acquire mass through a scalar boson called the Higgs. The four fundamental forces of interaction existing in nature are : the electromagnetic force, the strong force, the weak force and the gravitational force. Quantum Chromodynamics (QCD) is the theory of the strong interactions between the quarks mediated by the massless gluons. The quarks and gluons, together known as partons, have a peculiar property of “color” charge. Due to confinement property of QCD, the quarks cannot exist freely in nature but bind themselves into colorless particles called hadrons such as protons and neutrons together known as nucleons, pions etc. The structure and the properties of sub-atomic particles can be explored by first accelerating them using particle accelerators and then colliding at very high energies. The end products of these collisions get detected in the particle detectors constituting the real data. The data sets are analyzed in details to reveal the structure and characteristic properties of the fundamental particles.

To search the very rare particles or to investigate the physics beyond SM, the particle accelerators have become more bigger and complex. The Large Hadron Collider (LHC) is one of the today's biggest and most powerful collider where the protons are accelerated and collided at extremely high center-of-mass energies to probe their internal structure given by parton distribution functions (PDFs). The PDF sets give the probability to find a parton at an energy scale Q carrying a fractional momentum x of the proton. Since the proton is not elementary and is made up of partons, the proton-proton (pp) collisions are viewed as interactions between their constituent partons. The final products of the scattering are observed by Compact Muon Solenoid (CMS), one of the four detectors of the LHC, located around the interaction points of the collisions. The scattering cross-section can be expressed as a sum in terms of increasing powers of the strong coupling constant α_s convoluted with PDFs. The lowest-order α_s^2 term represents the production of two partons in final states whereas terms of higher-order α_s^3 , α_s^4 etc. signify the existence of multi-partons in final states. The highly energetic final state partons emit quarks and gluons with lower energies and give rise to a parton shower (PS). The colored products of parton shower hadronize to a spray of colorless hadrons known as jets. The jets are the final structures observed in the detector. So they carry the significant information about the energy and direction of the initial partons and hence are important to study. The final partons also have the probability to radiate more gluons and quarks which also hadronize and result in multijets in the final state. At LHC, such events are produced in large number and are an important source for testing the predictions given by QCD. They also serve as an important background in the searches for new particles and physics beyond SM.

The inclusive multijet event cross-section σ_{i-jet} given by the process $pp \rightarrow i \text{ jets} + X$, where every jet counts, is proportional to α_s^i . The study of inclusive jet cross-sections in terms of jet transverse momentum p_T and rapidity y is very important because it provides the essential information about the PDFs and

the precise measurement of α_S . Also the ratio of cross-sections given by Eq. 1.1 is proportional to the QCD coupling α_S and hence can be used to determine the value of α_S .

$$R_{mn} = \frac{\sigma_{m-jet}}{\sigma_{n-jet}} \propto \alpha_S^{m-n} \quad (1.1)$$

Instead of studying inclusive cross-sections, the cross-section ratio is more useful because of the partial or complete cancellation of many theoretical and experimental uncertainties between numerator and denominator. The CMS Collaboration has previously measured the ratio of the inclusive 3-jet cross-section to that of the inclusive 2-jet as a function of the average transverse momentum, $\langle p_{T1,2} \rangle$, of the two leading jets in the event at 7 TeV [1]. This study lead to an extraction of $\alpha_s(M_Z) = 0.1148 \pm 0.0055$, where the dominant uncertainty stems from the estimation of higher-order corrections to the next-to-leading order (NLO) prediction. In this thesis, a measurement of inclusive 2-jet and 3-jet event cross-sections as well as ratio of 3-jet event cross-section over 2-jet R_{32} , is performed using an event sample collected during 2012 by the CMS experiment at the LHC and corresponding to an integrated luminosity of 19.7 fb^{-1} of pp collisions at a center-of-mass energy of 8 TeV. The event scale is chosen as before to be the average transverse momentum of the two leading jets, referred to as $H_{T,2}/2$ in this thesis. The measurements are used to extract the value of the strong coupling constant at the scale of the Z boson mass $\alpha_s(M_Z)$ and the running of α_S with energy scale Q is studied.

This organization of the thesis is as follows :

Chapter 2 gives a brief overview of the Standard Model of particle physics and the theory of strong interactions QCD, theory of hadron collisions as well as formation of jets and jet algorithms.

Chapter 3 deals with experimental apparatus which covers the details of the CMS detector and its various sub-detectors.

Chapter 4 describes the methods of event generation used in different Monte-Carlo event generators, detector geometry simulation and reconstruction of the particles in the detector. This chapter also gives the details of the different approaches of jet reconstruction at CMS and applied jet-energy corrections along with the description of the software framework used in the analysis presented in the current thesis.

Chapter 5 presents the measurement of inclusive differential multijet event cross-sections and the cross-section ratio. The measurements are corrected for detector effects by unfolding procedure which is discussed in details in this chapter. The sources of the experimental uncertainties are studied in details.

Chapter 6 contains a detailed description of the NLO perturbative QCD theory predictions obtained using different PDF sets. compared to data and the extraction of α_S . The NLO predictions are corrected with the non-perturbative and electroweak corrections. The theoretical uncertainties are calculated from various sources. In the end of this chapter, the unfolded measurements are compared with the predictions at NLO in pQCD as well as with predictions from several Monte Carlo event generators.

Chapter 7 describes the method to extract the strong coupling constant at the scale of mass of Z boson $\alpha_s(M_Z)$ from the current measurements and the running of α_S with energy scale Q is presented along with the previous measurements from different experiments.

Chapter 8 summarizes the results and conclusions of the work done in this thesis.

The common unit convention based on International System of Units (SI) as followed in particle physics will be used throughout the thesis. In addition, the units electron volt (eV) and barn (b) are used for energy and interaction cross-section respectively. The reduced Planck constant (\hbar) and speed of light (c) are set to unity, i.e. $\hbar = c = 1$.

Chapter 2

Theoretical Background

Since 1930s, many theories and discoveries in particle physics have revealed the fundamental structure of matter. The matter is made up of fundamental particles and their interactions are mediated by four fundamental forces [2]. The theoretical models describe all the phenomena of particle physics as well as predict the properties of particles. These models must be either confirmed experimentally or totally excluded giving hints of new physics. This interplay between experimental discoveries and the corresponding theoretical predictions leads to a theoretical model called Standard Model, which describes the fundamental particles and their interactions. The world's most powerful particle accelerators and detectors are used by physicists to test the predictions and limits of the Standard Model where it has successfully explained almost all experimental results. This chapter describes the Standard Model with main focus on the theory of strong interactions called Quantum Chromodynamics and its features which serve as the theoretical base of this thesis.

2.1 Standard Model

The Standard Model (SM) of particle physics [3–5] was developed in 1970s. It is a mathematical framework which describes the nature and properties of the fun-

damental particles and the three of the four known forces of interactions between them, as summarized in Fig. 2.1. According to the SM, there are 12 elementary particles i.e. without any internal structure, known as fermions. The fermions have half integral spin and obey Fermi-Dirac statistics. They follow the Pauli exclusion principle according to which two or identical fermions cannot occupy the same quantum state. Each fermion has an associated anti-particle having the same properties but opposite-sign quantum numbers. Depending on how the fermions interact, these

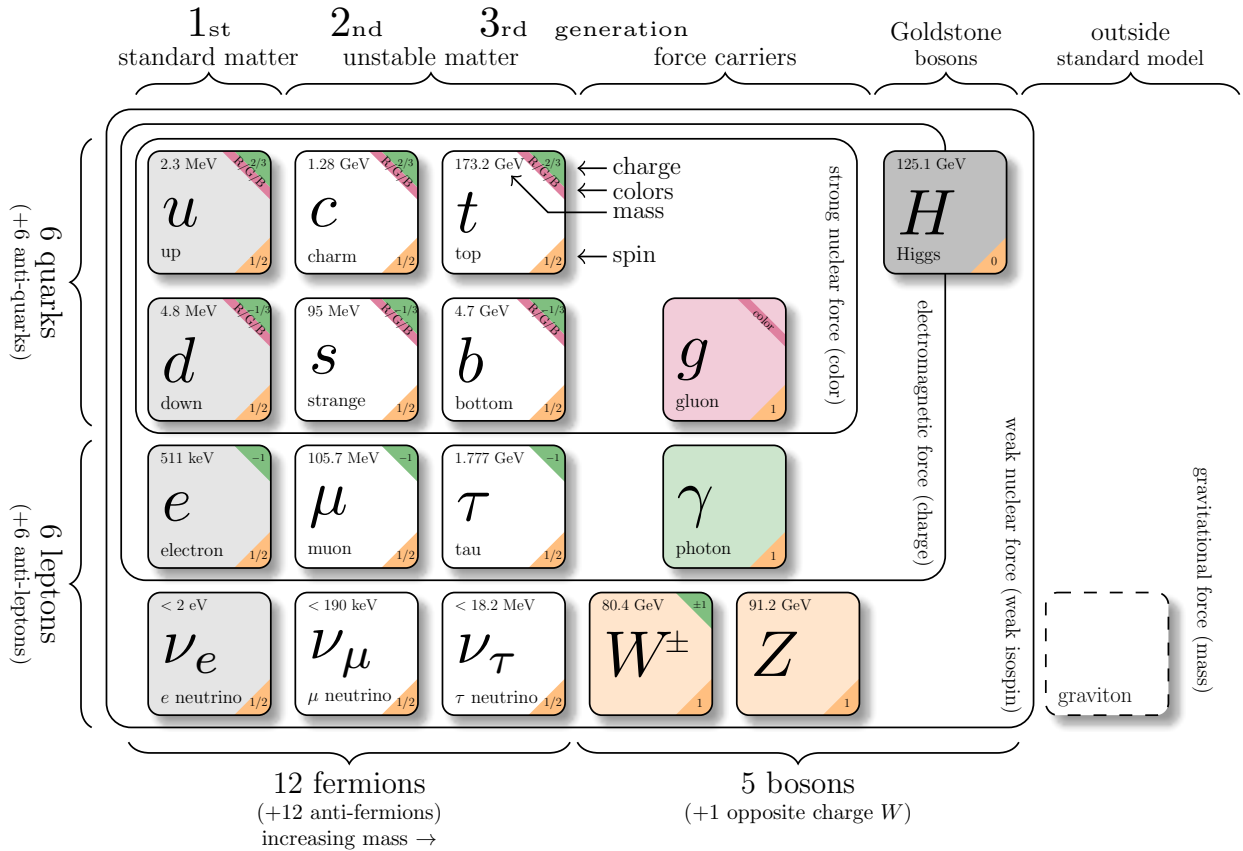


Figure 2.1: The Standard Model¹ summarizing the properties of elementary particles known as fermions (leptons and quarks) grouped into three generations, gauge bosons as mediators for the interactions, the scalar Higgs boson and not incorporated graviton for the gravitational force.

are classified into two categories - leptons (ℓ) and quarks (q). The leptons are of

¹Source : <http://www.texample.net/tikz/examples/model-physics>

six types : electron (e), muon (μ) and tau (τ) with electric charge $Q = -1^2$ and the corresponding neutrinos : electron neutrino (ν_e), muon neutrino (ν_μ) and tau neutrino (ν_τ) having electric charge $Q = 0$. The quarks exist in six “flavors” : up (u), down (d), strange (s), charm (c), bottom (b) and top (t). u , c and t carry electric charge $Q = \pm \frac{2}{3}$ whereas d , s and b carry $Q = \pm \frac{1}{3}$. The quarks and leptons are categorized into three generations. The first generation has the lightest and the most stable particles whereas the heavier and less stable particles belong to the second and third generations.

The four fundamental forces exist in nature : electromagnetic, strong, weak and gravitational force. Every interaction involves the exchange of a gauge boson : the photon (γ) for the electromagnetic force, gluons (g) for the strong force, two W ’s and a Z for the weak force and the graviton (not yet found) for the gravitational force. However, the gravitational force has not been incorporated into SM yet. Along with this, the existence of dark matter or dark energy and the matter-antimatter asymmetry are still missing pieces in the SM. The interaction between fundamental particles acts because of some peculiar property of the particles - charge for the electromagnetic force, color for the strong force and flavor for the weak force.

In the SM, the first three forces are unified into one quantum field theory [6], known as Grand Unified Theory (GUT) [7–9]. The SM framework based on quantum field theories is described by $SU(3)_C \otimes SU(2)_L \otimes U(1)_Y$ gauge symmetry where C stands for the color charge, L for weak isospin and Y for hypercharge. Here $SU(3)_C$, $SU(2)_L$ and $U(1)_Y$ terms give rise to strong, weak and electromagnetic forces, respectively. $U(n)$ are the unitary and $SU(n)$ are the special unitary groups of degree n . The electromagnetic interaction of particles is explained by a well established modern theory called Quantum Electrodynamics (QED). In SM, the weak and electromagnetic interactions are combined by an electroweak theory. The

²all charges are expressed in units of elementary charge e

spontaneous symmetry is broken due to the coupling to the scalar Higgs field which results in the massive W^\pm and Z bosons and the massless photon (γ). The Higgs boson, named after Peter Higgs, is the field quantum of the Higgs field responsible for electroweak symmetry breaking. Its existence was confirmed by the CMS [10] and ATLAS [11] collaborations in 2012, with the properties consistent with the SM. The $SU(3)_C$ term defines the strong interaction between quarks and gluons mediated by gluons, with the three degrees of freedom of the color charge (C). In contrast to the electroweak symmetry, the $SU(3)_C$ of the strong interaction is an exact symmetry and hence the gluons are massless. The strong interaction between quarks and gluons is described by theory called quantum chromodynamics (QCD), explained in details in the next section of this thesis.

2.2 Quantum Chromodynamics

The strong interactions between the quarks and gluons are described by a non-abelian gauge theory called quantum chromodynamics (QCD) [12, 13]. The gauge group of QCD is the special unitary group $SU(3)_C$ with color charges C as the generators of the gauge group. Color charge is the peculiar property of QCD and has a same role as the electric charge in electromagnetic interactions. However, the mediator of electromagnetic interactions i.e. photon, itself does not carry any electric charge whereas the gluon itself carry color charge. This allows the self coupling of gluons and hence make the theory non-abelian. Both the quarks and gluons carry three types of color charges : red (r), green (g) and blue (b), and three types of anti-color charges : anti-red (\bar{r}), anti-green (\bar{g}) and anti-blue (\bar{b}). The quarks carry a single color charge whereas gluons carry a combination of color charges. There are nine eigen states of gluons but one of them $\frac{1}{\sqrt{3}}(r\bar{r} + g\bar{g} + b\bar{b})$ is totally symmetric color singlet which has no net color charge and does not take part in interaction.

The remaining eight eigen states of the gluons are :

$$r\bar{b}, \ r\bar{g}, \ g\bar{r}, \ g\bar{b}, \ b\bar{g}, \ b\bar{r}, \ \frac{1}{\sqrt{2}}(r\bar{r} - b\bar{b}), \ \frac{1}{\sqrt{6}}(r\bar{r} + b\bar{b} - 2g\bar{g}) \quad (2.1)$$

The dynamics of the quarks and gluons are controlled by the gauge invariant QCD Lagrangian \mathcal{L}_{QCD} which is composed of four terms as :

$$\mathcal{L}_{QCD} = \underbrace{-\frac{1}{4}F_{\mu\nu}^A F_A^{\mu\nu}}_{\mathcal{L}_{gluons}} + \underbrace{\sum_{flavors} \bar{q}_a (i\gamma^\mu (D_\mu)_{ab} - m_q) q_b}_{\mathcal{L}_{quarks}} + \mathcal{L}_{gauge} + \mathcal{L}_{ghost} \quad (2.2)$$

where \mathcal{L}_{gluons} describes the kinetic term of the gluon fields \mathcal{A}_μ^A ; \mathcal{L}_{quarks} defines the interaction between spin- $\frac{1}{2}$ quark fields q_a of mass m_q and spin-1 gluon fields \mathcal{A}_μ^A summing over all presently known six flavors of quarks; \mathcal{L}_{gauge} describes the chosen gauge and \mathcal{L}_{ghost} is the so-called ghost term required to treat the degeneracy of equivalent gauge field configurations in non-abelian gauge theories. In Eq. 2.2, the Greek letters $\mu, \nu, \dots \in \{0,1,2,3\}$ are the space-time indices; $a,b,c \in \{1,2,3\}$ and $A,B,C \in \{1,\dots,8\}$ are the indices of the triplet and octet representations, respectively, of the gauge symmetry group $SU(3)_C$. The field tensor $F_{\mu\nu}^A$ is defined as

$$F_{\mu\nu}^A = \partial_\mu \mathcal{A}_\nu^A - \partial_\nu \mathcal{A}_\mu^A - g_s f_{ABC} \mathcal{A}_\mu^B \mathcal{A}_\nu^C \quad (2.3)$$

where g_s is the coupling constant determining the strength of the interaction between colored partons and f_{ABC} are the structure constants of the $SU(3)_C$ group. The last term in Eq. 2.3 is a non-abelian term which distinguishes QCD from QED and gives rise to a three- and a four-gluon vertex. In the term \mathcal{L}_{quarks} , $(D_\mu)_{ab}$ is the covariant

derivative given by Eq. 2.4 and γ_μ are the Dirac γ -matrices.

$$(D_\mu)_{ab} = \partial_\mu \delta_{ab} + ig_s T_{ab}^A \mathcal{A}_\mu^A \quad (2.4)$$

\mathcal{A}_μ^A are the gluon fields with factors T_{ab}^A factors corresponding to the generators of the $SU(3)_C$ gauge group. The generators are represented via $T^A = \lambda^A/2$ by the Hermitian and traceless Gell-Mann matrices λ^A [14]. The generator matrices T^A follow the commutation relations :

$$\left[T^A, T^B \right] = if_{ABC} T^C \quad (2.5)$$

In \mathcal{L}_{QCD} , the classical contribution comes from \mathcal{L}_{gluons} and \mathcal{L}_{quarks} terms which give rise to the free quark- and gluon-field terms, and the quark-gluon interaction terms presented in Fig. 2.2. The cubic and quartic gluon self-interaction vertices proportional to g_s and g_s^2 , respectively, come into play due to the non-abelian property of QCD.

It is impossible to use perturbation theory on a gauge invariant Lagrangian without choosing a specific gauge in which to calculate. The usual gauge-fixing term is given by

$$\mathcal{L}_{gauge} = -\frac{1}{2\xi} (\partial^\mu \mathcal{A}_\mu^A)^2 \quad (2.6)$$

where ξ may be any finite constant. This choice fixes the class of covariant gauges with ξ as the gauge parameter. As QCD is non-abelian, the gauge fixing term must be supplemented by a ghost Lagrangian as

$$\mathcal{L}_{ghost} = \partial_\alpha \eta^{A\dagger} (D_{AB}^\mu \eta^B) \quad (2.7)$$

where η^A is a complex scalar field which obeys Fermi-Dirac statistics. The ghost

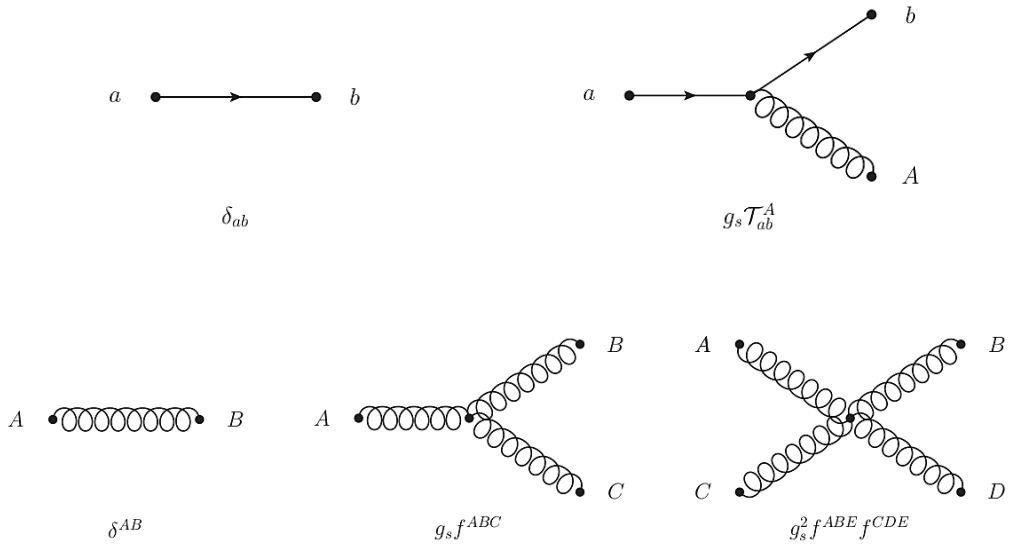


Figure 2.2: The fundamental Feynman rules of a free quark-field term (top left), quark-gluon interaction term (top right), free gluon-field term (bottom left), cubic gluon self-interaction term (bottom middle) and quartic gluon self-interaction term (bottom right). Taken from [15].

fields cancel unphysical degrees of freedom arising due to use of covariant gauges. This completes the QCD Lagrangian shown in Eq. 2.2.

The strength of an interaction is given by a fundamental parameter called the coupling constant α . In QED, the coupling constant $\alpha_e = e^2/4\pi = 1/137$ is constant. In contrast to this, in QCD, the coupling constant $\alpha_S(Q) = g_s^2/4\pi$ is not constant and depends on the separation between the interacting particles. It increases with the increase in the distance or decrease in the energy scale Q . At large distances or low energies, the quarks can never be found as free particles but exit in color neutral bound states known as hadrons. Hadrons are of two types : baryons and mesons. According to the quark model [2] every (anti-)baryon is made up of three (anti-)quarks and every meson is made up of a quark-antiquark pair. When the colored partons within a hadron are pulled farther and farther apart, there is an increase in the strength of force between them. This results in creation of new quark-antiquark pair making difficult to liberate a free quark or gluon. This property of QCD is

known as confinement according to which at low energy, the partons are forever bound into hadrons such as protons (uud), neutrons (udd). Although the gluons are massless but the confinement leads to the finite range of the strong interactions. On the other hand, at small distances, the strength of coupling decreases. The quarks and gluons interact very weakly and are treated as free particles. This property is known as asymptotic freedom. This indicates that perturbative theory is only applicable at high energies or small distances.

2.2.1 Perturbative Quantum Chromodynamics

At high energies, the property of asymptotic freedom allows a perturbative treatment in QCD calculations. In perturbative quantum chromodynamics (pQCD), any physical observable X such as cross-section of a scattering process, can be expanded as a perturbative series in terms of coupling constant α_S as :

$$X = \sum_{i=0}^N \alpha_s^n c_i = c_0 + \alpha_s^1 c_1 + \alpha_s^2 c_2 + \dots \quad (2.8)$$

where c_i are the perturbative coefficients. In a process, the pQCD calculation of X is determined by summing over the amplitudes of all Feynman diagrams contributing to that process. For a given Feynman diagram, the power of α_S is determined by the number of vertices associated with quark-gluon or gluon-gluon interactions. A leading order (LO) prediction sums over only the lowest-order contribution whereas next-to-leading order (NLO) includes terms with the additional powers of α_S . The next-to-next-to-leading order (NNLO) includes emission of another gluon or a virtual gluon loop. The different order of the QCD processes are shown in Fig. 2.3. The calculations become complex with the loop diagrams where the momenta of the virtual particles in a loop are not fully constrained by four-momentum conservation and the associated integrals are divergent. Such ultraviolet (UV) divergences enter

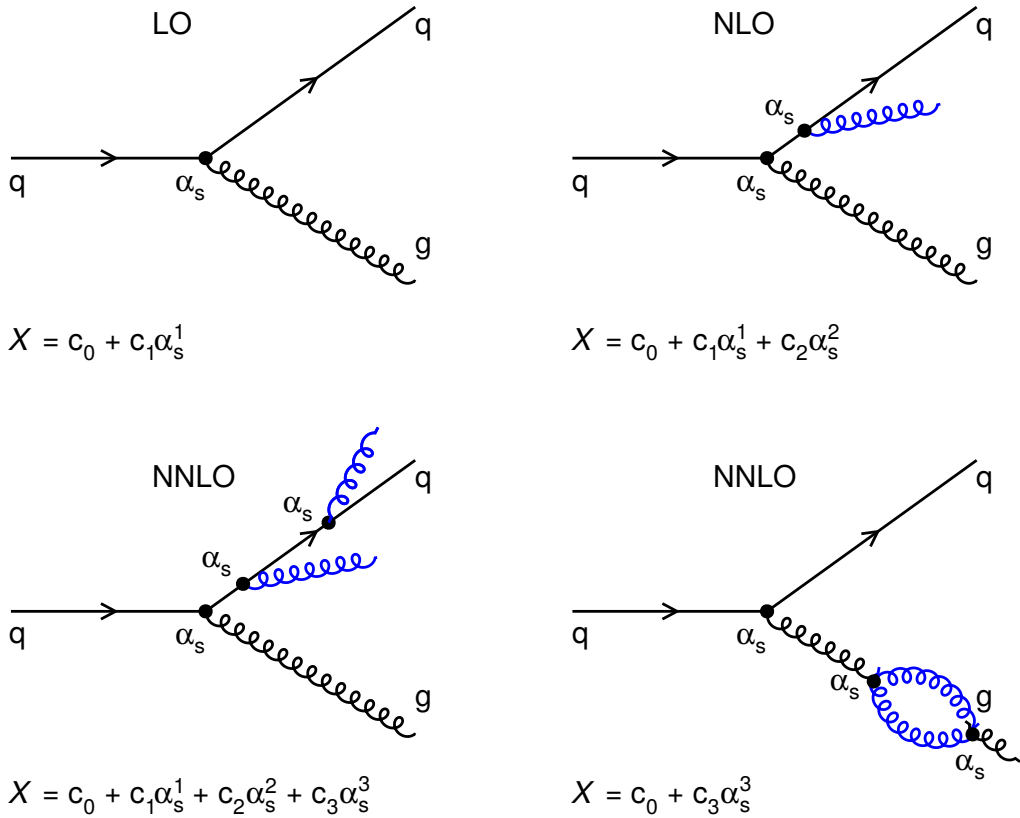


Figure 2.3: The Feynman diagrams³ of leading-order (LO), next-to-leading order (NLO) and next-to-next-to-leading order (NNLO) processes in quantum chromodynamics along with the perturbative expansion of any observable X in powers of the strong coupling constant α_S . At each successive step in perturbation series, the emission of an additional gluon take place.

the calculations beyond LO either due to loop or vertex corrections. These are overcome by a procedure known as renormalization, described in next section. Apart from the UV divergences, the QCD also suffers from infrared and collinear divergences (IRC) due to the presence of massless gluons and neglected quark masses. These need to be handled in pQCD calculations. The observable to be studied must be IRC safe.

³Drawn using ROOT

2.2.2 Renormalization and Running of the Strong Coupling

The renormalization is a mathematical procedure which allows the finite calculation of momenta integrals of virtual loop by removing UV divergences. It introduces a regulator for the infinities, the renormalization scale μ_r . At first, the divergences are regularized temporarily by introducing a cut-off to the loop momenta at μ_r scale. Then the free parameters of the Lagrangian, i.e. the coupling constant are redefined or renormalized to absorb the UV divergences. Due to this, both $\alpha_s(Q)$ and observable X become a function of μ_r . The exact dependence of $\alpha_s(\mu_r^2)$ on μ_r is described by the renormalization group equation (RGE) which determines the running of $\alpha_s(\mu_r^2)$. According to RGE, the dependence of X on μ_r must cancel. Mathematically this can be expressed as :

$$\mu_r^2 \frac{d}{d\mu_r^2} X \left(\frac{Q^2}{\mu_r^2}, \alpha_s(\mu_r^2) \right) = \left(\mu_r^2 \frac{\partial}{\partial \mu_r^2} + \mu_r^2 \frac{\partial \alpha_s(\mu_r^2)}{\partial \mu_r^2} \frac{\partial}{\partial \alpha_s(\mu_r^2)} \right) X = 0 \quad (2.9)$$

Using beta function $\beta(\alpha_s) = \mu_r^2 \frac{\partial \alpha_s(\mu_r^2)}{\partial \mu_r^2}$, Eq. 2.9 can be re-written as

$$\left(\mu_r^2 \frac{\partial}{\partial \mu_r^2} + \beta(\alpha_s) \frac{\partial}{\partial \alpha_s(\mu_r^2)} \right) X = 0 \quad (2.10)$$

By setting the renormalization scale equal to the physical scale i.e. $\mu^2 = Q^2$, $X(1, \alpha_s(Q))$ is a solution to above equation. Q -dependence of the X is only from the renormalization of the theory which is present in the classical theory. Hence measuring the Q -dependence of X will directly probe the quantum structure of the theory. The β function in QCD has a perturbative expansion as :

$$\beta(\alpha_s) = -\alpha_s^2 \left(b_0 + b_1 \alpha_s + b_2 \alpha_s^2 + \mathcal{O}(\alpha_s^3) \right) \quad (2.11)$$

where b_n is the $n+$ 1-loop β -function coefficients giving the dependence of the coupling on the energy scale Q . In the modified minimal subtraction ($\overline{\text{MS}}$) scheme [16, 17], the beta coefficient functions have following values :

$$b_0 = \frac{33 - 2n_f}{12\pi}, \quad b_1 = \frac{153 - 19n_f}{24\pi^2}, \quad b_2 = \frac{77139 - 15099n_f + 325n_f^2}{3456\pi^3} \quad (2.12)$$

where n_f is the number of quark flavours with masses $m_q < \mu_r$. On integration of Eq. 2.11, the energy dependence of α_s is yielded. Neglecting the higher orders, the first order solution of RGE is :

$$\alpha_s(\mu_r^2) = \frac{1}{b_0 \ln(\mu_r^2/\Lambda_{QCD}^2)} \quad (2.13)$$

where Λ_{QCD} is the constant of integration. The perturbative coupling becomes large at the scale Λ_{QCD} and the perturbative series diverge. With $b_0 > 0$, the coupling becomes weaker at higher scales Q , i.e. the effective color charge is small at small distances or large energies. This allows the quarks to behave as free particles within the hadron, leading to the property called asymptotic freedom. It is always convenient to express α_s at some fixed scale. Since some of the best measurements come from Z decays, it is common practise to determine the strong coupling at the scale of the Z boson mass $\alpha_s(M_Z)$. So, Eq. 2.13 can be expressed as :

$$\alpha_s\left(\mu_r, \alpha_s(M_Z)\right) = \frac{\alpha_s(M_Z)}{1 + \alpha_s(M_Z)b_0 \ln(\mu_r^2/M_z^2)} \quad (2.14)$$

Since α_s is the free parameter of QCD theory, it is always extracted from the experimental measurements and evolved to the scale of the Z boson. According to Particle Data Group (PDG) [18], the current world average value of the strong

coupling constant at the scale of mass of Z boson is

$$\alpha_s(M_Z) = 0.1181 \pm 0.0011 \quad (2.15)$$

This value is derived using data from deep inelastic scattering process, electron-positron annihilation processes, hadronic τ lepton decays, lattice QCD calculations and electroweak precision fits. The different experimental determinations of the strong coupling constant evolved at the scale Q are shown as a function of Q in Fig. 2.4 which describe the running of the α_s up to the 1 TeV scale.

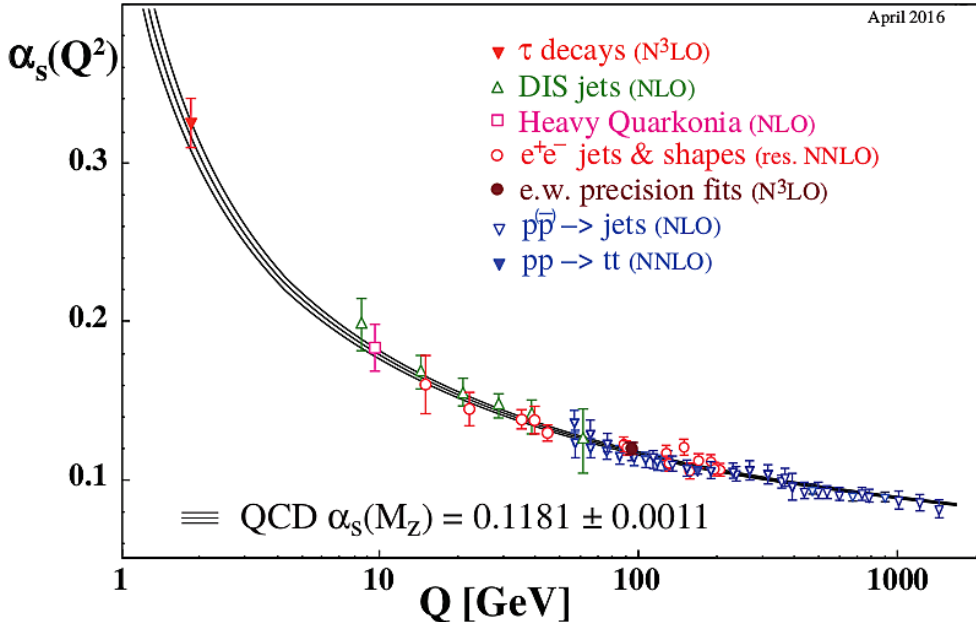


Figure 2.4: The different experimental measurements of the strong coupling constant α_S evolved at the energy scale Q are shown as a function of Q . These describe the running of the α_S up to the 1 TeV scale. Taken from [18].

2.3 Hadronic Collisions

At a large momentum transfer, the collision between two hadrons can be visualized as an interaction between their constituents - quarks and gluons. In this thesis, we

are studying the proton-proton collisions taking place at the Large Hadron Collider (LHC). A proton is a complex composite particle consisting of three valence quarks (uud), gluons for the exchange of the strong force and the sea quarks. The sea quarks consist of quark-antiquark pairs coming into and out of existence rapidly and continuously due to gluon colour field splitting. In any collision, one of the most important quantities to evaluate is the cross-section (σ) of a certain process which gives the probability that the two hadrons interact and give rise to that specific process. In a hadronic collision, the perturbation theory is only valid at the parton-level but due to property of confinement at low energies, free partons cannot exist in nature. Only hadrons with a complex internal structure are available for the high energy collisions. Here, a factorization theorem of QCD [19] comes into play which allows the calculation of σ by separating into two parts : a short-distance partonic cross-section calculable with pQCD, and a non-perturbative long-distance part described by parton distribution functions $f_i(x, \mu_f)$ (PDFs). The PDFs describe the partonic content of the colliding hadrons and give the probability to find a parton i with momentum fraction x within a hadron. μ_f is a factorization scale which corresponds to the resolution with which the hadron is being probed. The particles which are emitted with transverse momenta $p_T > \mu_f$ are considered in the calculation of hard scattering perturbative coefficients. The particles emitted with $p_T < \mu_f$ are accounted for within the PDFs. Applying the factorization theorem in a proton-proton collision, the cross-section of a hard scattering process can be written as :

$$\begin{aligned} \sigma_{P_1 P_2 \rightarrow X} = & \sum_{i,j} \int dx_1 dx_2 f_{i,P_1}(x_1, \mu_f) f_{j,P_2}(x_2, \mu_f) \\ & \times \hat{\sigma}_{ij \rightarrow X} \left(x_1 p_1, x_2 p_2, \alpha(\mu_r^2), \frac{Q^2}{\mu_f^2} \right) \end{aligned} \quad (2.16)$$

where f_i and f_j are the proton PDFs which depend on momentum fractions x_1 and x_2 of parent protons P_1 and P_2 respectively as well as on the factorization scale μ_f .

The sum extends over all contributing initial-state parton flavours i, j . The cross-section for the production of final state X at parton level ($\hat{\sigma}_{ij}$) depends on the final state phase, the factorization scale μ_f and the renormalization scale μ_r . Figure. 2.5 illustrates the factorization into the PDFs and the hard scattering cross-section in a proton-proton collision. The PDFs of the proton are a necessary input to almost

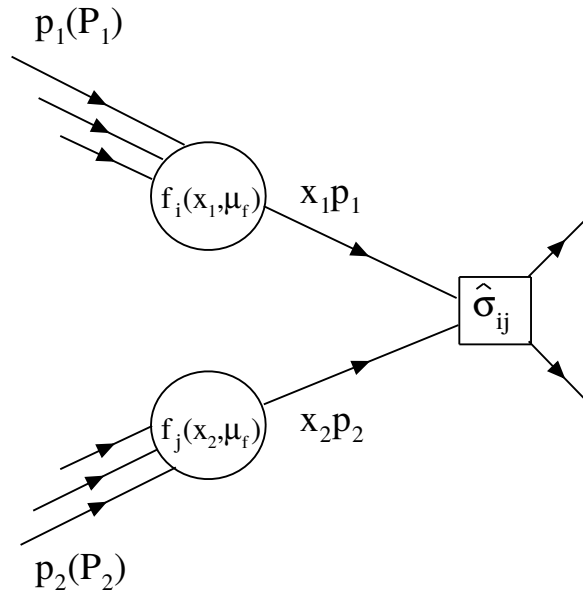


Figure 2.5: Schematic illustration⁴ of the factorization theorem in a collision of two protons P_1 and P_2 having momenta p_1 and p_2 , respectively. In a hard-scattering process at a scale Q^2 , the two partons x_1 and x_2 participate with momenta $x_1 p_1$ and $x_2 p_2$. The total cross-section is factorized into the hard scattering cross-section $\hat{\sigma}_{ij}$ calculable using perturbative quantum chromodynamics and the PDFs $f_i(x_1, \mu_f)$ and $f_j(x_2, \mu_f)$ with factorization scale μ_f .

all theory predictions of a proton-proton collision. The QCD does not predict the parton content of the proton. So the shapes of PDFs are determined in fits to experimental measurements of different experiments. The dependence of PDFs on μ_f is given by the Dokshitzer-Gribov-Lipatov-Altarelli-Parisi (DGLAP) [20–22] equations which use α_S and the RGE as inputs. The knowledge of proton PDFs mainly

⁴Drawn using ROOT

comes from the Deep Inelastic Scattering (DIS) HERA, fixed target and Tevatron data. The LHC data has a potential to improve constraints of the PDFs further as done in one of the recent CMS measurements [23]. There are several groups which determine the PDFs using the different minimization methods, phenomenological approaches and the methods to estimate the uncertainties. The global PDFs are the CTEQ [24], MMHT [25], NNPDF [26], ABM [27] and HERAPDF [28] at LO, NLO and NNLO.

2.3.1 Parton Shower and Hadronization

The partons involved in a hard scattering process get accelerated due to large momentum transfers. These accelerated partons emit QCD radiation in the form of gluons with successively lower energy. Unlike the uncharged photons in QED, the gluons themselves carry color charge and hence also emit further gluons. The emitted gluons in turn splits into $q\bar{q}$ pairs. This successive emission of partons lead to a parton shower. In a parton shower, the main contribution is by the collinear parton splitting and the soft gluon emissions. The parton shower mimics the effect of higher-order corrections to the hard process. These cannot be calculated exactly and are taken into account using the parton shower approximation. The two incoming partons which are constituents of two colliding hadrons and taking part in hard scattering process can also develop parton showers, commonly known as Initial-State Radiation (ISR). The initial partons produce showers till they collide to initiate the hard scattering process. The final outgoing partons produced from a hard scattering process can also undergo parton showering giving rise to Final-State Radiation (FSR). A parton shower terminates when the scale Q is below the hadronization scale ~ 1 GeV for QCD.

At the end of the shower, there is a decrease in the energy of partons due to successive emission of gluons. Due to this the coupling constant of QCD α_s evolves and become large. This leads to the confinement of colored quarks and

gluons into the color-neutral composite particles called hadrons and this process is known as hadronization. The hadronization takes place at low momentum transfer and hence non-perturbative in nature. Although no exact theory for hadronization is known, the different phenomenological models have been developed to simulate the hadronization process. The two main models implemented in Monte Carlo event generators to simulate the hadronization process are :

Lund String Model - In the Lund string model of hadronization [29], the highly energetic gluons are treated as field lines. Due to the gluon self-interaction, the gluons are attracted to each other forming a narrow tube or string of strong color field between a $q\bar{q}$ pair. This model is based on an observation that at distances greater than about a femtometer (fm), the potential energy $V(r)$ of colored quarks grows linearly with the increase in distance between them (r) as :

$$V(r) = \kappa r \quad (2.17)$$

where $\kappa \sim \text{GeV}/\text{fm}^2$ is the tension of the string connecting the quarks. When the q and \bar{q} are pulled apart from each other move apart, the gluonic string stretches. Due to this, the potential energy of the string grows at the expense of the kinetic energy of the quarks. As the potential energy becomes of the order of hadron masses, the string breaks at some point along its length, creating a new $q\bar{q}$ pair. The newly formed two string segments again stretch and break producing further $q\bar{q}$ pairs. This process of stretching and breaking continues until all the potential energy gets converted to $q\bar{q}$ pairs. This whole process is illustrated in Fig 2.6. The $q\bar{q}$ pairs then undergo hadronization due to confinement property. PYTHIA Monte Carlo generator uses the Lund string model.

Cluster Model - The cluster model of hadronization [30, 31] is based on pre-confinement property of QCD [32]. According to this property, at evolution scales Q_0 much less than the hard process scale Q , the partons produced in a shower are

clustered in colourless groups with an invariant mass distribution, depending on nature of hard process and Q_0 , not on Q . This model contains two steps : firstly all gluons split into $q\bar{q}$ pairs at the end of the parton shower and in the second step, a new set of low-mass color-singlet clusters are obtained which decay into either secondary clusters or directly into hadrons. The generator HERWIG is based on the cluster fragmentation model. However, this model has problems in dealing with the decay of very massive clusters.

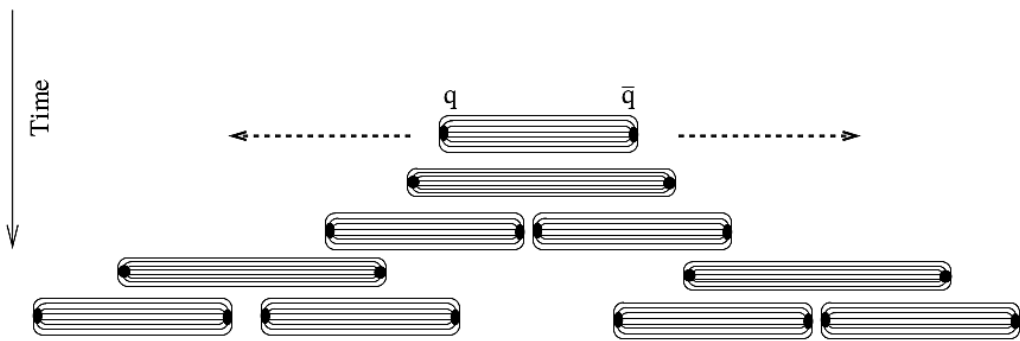


Figure 2.6: Illustration of the hadronization process in Lund string model⁵. When the quark q and anti-quark \bar{q} are pulled apart from each other, the potential energy of the gluonic string connecting the quarks increases. As it becomes of the order of hadron masses, the string breaks and a new $q\bar{q}$ pair is created. The breaking of string and creation of $q\bar{q}$ continues till all the potential energy gets converted to $q\bar{q}$ pairs which then get hadronized.

2.3.2 Underlying Event

Due to the composite nature of the protons, their collisions are not clean events. The event structure is significantly more complex than that of the lepton collisions. The final states of the collisions involves the multi-particle calculations. In a high energy proton-proton collisions, the underlying event (UE) includes the effects which are not coming from the primary hard scattering process. The UE include the contributions from relatively small momentum transfer processes : initial and final-state radiations (ISR, FSR), leftover partons in the collisions called beam remnants

⁵Source : <http://inspirehep.net/record/806744>

and multiple parton interactions (MPI). Due to composite nature of proton, the remaining two partons which do not participate in a hard collision may also interact giving rise to multiple parton interactions. The UE induces an additional energy in an event which is not related to the main hard interaction. This acts an unavoidable background which needs to be removed. Hence, it is very crucial to study and understand the UE. The UE activity increases with Q and the center-of-mass energy \sqrt{s} . Figure 2.7 shows the complex variety of processes taking place in a single proton-proton collision.

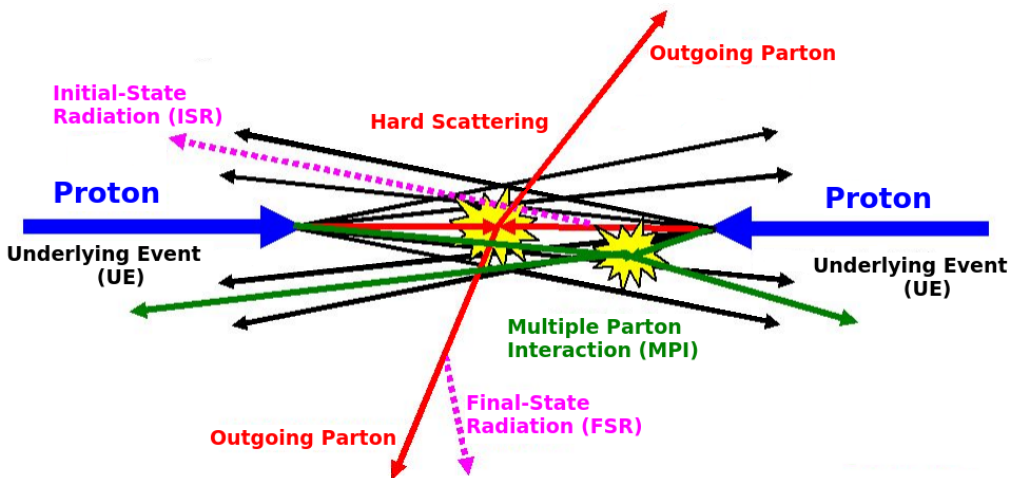


Figure 2.7: A proton-proton collision⁶ involving the main hard scattering process along with the low momentum transfer underlying event (UE) contributions coming from initial- and final-state radiations (ISR and FSR) complemented with multiple parton interactions (MPI) and collisions from leftover partons called beam remnants.

The bunch of hadrons, produced from hadronization of quarks and gluons, gets collimated in the form of “jets” with the direction towards the direction of the initial parton that originated them. The jets are the final structures observed experimentally in the detectors. These act as a bridge between the elementary quarks and gluons of QCD and the final hadrons produced in high energy collisions. Therefore, at large momentum transfer of the interacting partons, the jets and their observables are the best tools to test the predictions of perturbative QCD. Also,

⁶Source : [The Energy Dependence of Min-Bias and the Underlying Event at CDF](#)

the jet production is sensitive to the strong coupling constant α_S . The precise knowledge of the jet production cross-section can help to extract the value of α_S and also to reduce the uncertainties of the PDFs of proton. In LHC, the simplest jet production process is $2 \rightarrow 2$ scattering process at leading-order giving dijet events. But the partons originating from ISR, FSR or MPI can also hadronize to produce jets greater than 2 in a single proton-proton collision. This results in the production of multijet events. The investigation of inclusive multijet event cross-sections permits more elaborate tests of QCD. Also, a precise study of jet variables helps to understand the signal and background modelling for the new physics search in hadronic final states. In this thesis, the inclusive multijet event cross-sections as well as the ratio of cross-sections are exploited to extract the value of strong coupling constant α_S . In the next section, we focus on the definition of a jet.

2.4 Jets

Jets [33] are the conical structures which group the hadrons into a single physics entity. Figure 2.8 shows the outgoing partons of the hard scattering process in a proton-proton collision, undergoing fragmentation and hadronization processes and forming a conical jet with radius R. The jet structure was observed for the first time hadron production of e^+e^- annihilation process at SLAC in 1975 [34]. The partons can not be measured directly by the experiments because they can not exist freely in nature. The information about the dynamics of the partons can be obtained indirectly from jets. The configurations of high-energy quarks and gluons at short distances are truly reflected in the energy and angular distributions of the jets. Hence the jets are important to study. To perform the clustering of particles, a certain set of rules are followed in the form of jet algorithms.

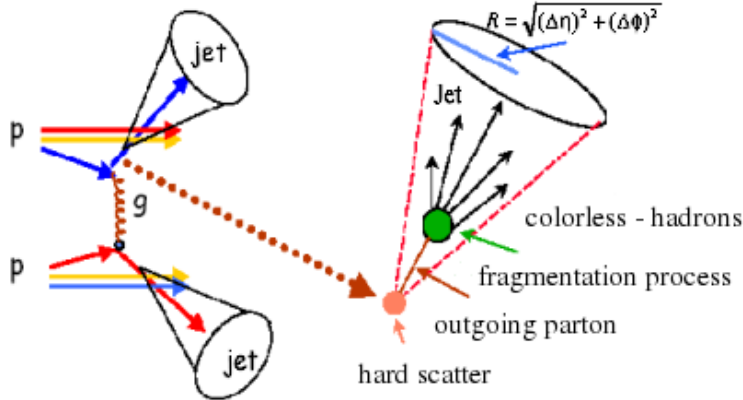


Figure 2.8: In a proton-proton collision, the outgoing partons of the hard scattering process undergo fragmentation and hadronization processes producing a shower of partons which get collimated into a conical jet with radius R .

2.4.1 Jet Algorithms

Jet algorithms [35] provide a set of rules which determine how the particles can be clustered into a jet. In a jet algorithm, usually one or more parameters are involved that indicate how close two particles must be for them to belong to the same jet. These parameters can either measure closeness in coordinate space (cone algorithms) or in momentum space (sequential algorithms). The jet algorithms are applicable on parton, particle and calorimeter levels. A recombination scheme is always associated with a jet algorithm which calculates the momentum assigned to the combined particles. A jet algorithm along with its parameters and a recombination scheme forms a “jet definition”. A jet definition [36] must be simple to implement in an experimental analysis as well as in the theoretical calculation. It should be defined at any order of perturbation theory. It must yield finite cross-section at any order of perturbation theory that is relatively intensive to hadronization. In addition to these requirements, a jet algorithm must be infrared and collinear (IRC) safe. Infrared safety is the property by which the addition of a soft emission i.e. addition of a soft gluon should not change or modify the number of hard jets found in an event. In an infrared unsafe algorithm, a soft gluon emission in the middle of two

cone jets can lead to overlap of the two initial cones, as shown in Fig. 2.9 (top). This produces a single jet instead of initial two jets resulting in the change of number of jets. Collinear safety is the property by virtue of which the collinear splitting

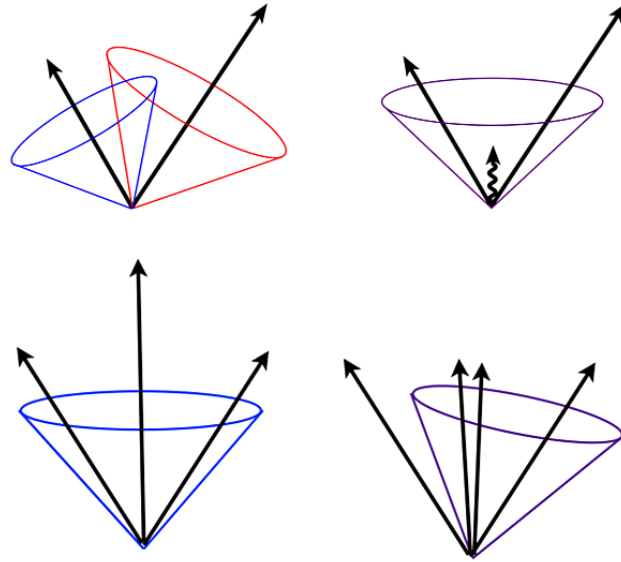


Figure 2.9: Top : Infrared unsafe behaviour of jet algorithm is illustrated where the presence of soft radiation between two jets may cause a merging of the jets that would not occur in the absence of the soft radiation. Bottom : Collinear unsafe behavior of jet algorithm is shown in which the number of jets change due to a collinear splitting⁷.

i.e. replacement of one parton by two at the same place should not modify the number of jets formed in a jet. This implies that the output of the jet algorithm should remain the same if the energy of a particle is distributed among two collinear particles. According to the collinear safety property, the two cases shown in Fig. 2.9 (bottom) should always produce a single jet. If an algorithm produces zero or two jets after collinear splitting, then it is not collinear safe. The jet algorithms can be classified mainly into two types :

Cone algorithms - In the iterative cone (IC) algorithm [37], the jet is defined as a cone with fixed radius R in $\eta\phi$ space drawn around the highest energy seed. The relative distance (d) of all the particles is iteratively calculated and compared

⁷Source : <http://inspirehep.net/record/1251416>

with R . If the calculated $d < R$, the considered particles are clustered together in a jet and the directions of the clustered particles give the direction of the jet. On the other side i.e. if $d > R$, the considered particles initiate two different jets. The algorithm iterates until the cone is stable which means that the direction of sum of momentum of all the particles is same as that of the center of cone. But IC algorithm is not IRC safe. There is another cone algorithm, Seedless Infrared-Safe cone (SIS-Cone) [38], which is an exact seedless i.e. does not rely on seed threshold and is IRC safe. This is a complex approach which tests the stability of all subsets of particles and has a complexity of $\mathcal{O}(N2^N)$ for N particles. But this algorithm is much slower and hence not preferred.

Sequential algorithms - The sequential algorithms [39] cluster the particles by defining a distance between pairs of particles and recombine the pair of closest particles successively. This is collinear and infrared safe algorithm. It is possible for the jet cones to overlap such that one particle is contained in more than one jet but the sequential algorithm never assigns a particle to more than one jet. The sequential algorithm is based on transverse momentum p_T of the particles and follows the below procedure :

1. First the distance d_{ij} between two particles i and j and distance d_{iB} of the particle to the beam are calculated.

$$d_{ij} = \min(p_{Ti}^{2p}, p_{Tj}^{2p}) \frac{\Delta R_{ij}^2}{R^2}, \quad d_{iB} = p_{Ti}^{2p} \quad (2.18)$$

$$\text{where } \Delta R_{ij}^2 = (\eta_i - \eta_j)^2 + (\phi_i - \phi_j)^2$$

2. If $d_{ij} < d_{iB}$, then the particles i and j are merged into a new single particle k , summing four-momenta of two initial particles by recombination scheme and step 1 is repeated.

3. If $d_{iB} < d_{ij}$, particle i is declared as a final-state jet and the particle gets removed from the list.

This procedure continues until all particles get clustered into jets. The value of the parameter p defines the three different sequential algorithms having distinct properties. For $p = 1$, we have k_t algorithm [40, 41], $p = 0$ gives the Cambridge/Aachen (C/A) algorithm [42] whereas $p = -1$ defines the anti- k_T algorithm [43]. The k_t algorithm involves clustering of soft particles first resulting in an area that fluctuates considerably. This algorithm is susceptible to the underlying and pileup events. The C/A algorithm involves energy independent clusterings. Both k_t and C/A produce jets of irregular shapes. Instead of jet analysis, these are widely considered for studying the jet substructure. The anti- k_T algorithm tends to cluster hard particles first and produce jets with circular regular shapes. It is less sensitive to underlying and pileup events. It is the most preferred algorithm for jet studies at the LHC. Figure 2.10 shows the clustering of same particles but using the different jet algorithms.

A jet algorithm must specify how to combine the momenta of different partons or particles going to be clustered into a jet. This is given by the recombination scheme. The most widely used recombination scheme is the E -scheme [37] which corresponds to vector addition of four-momenta where the four-momenta of the jet is obtained by simply adding the four-momenta vector of merging particles.

The sequential clustering algorithms have always been favoured by theorists but not by experimentalists because of slow computational performance. However, the introduction of the FASTJET program [44] enhanced the speed of clustering algorithms and hence are preferred by experimentalists as well. This thesis studies the particles produced in proton-proton collisions by clustering them in to jets using anti- k_t algorithm with distance parameter $R = 0.7$. These jets are observed in the Compact Muon Solenoid detector of the Large Hadron Collider, whose details are discussed in the coming chapter.

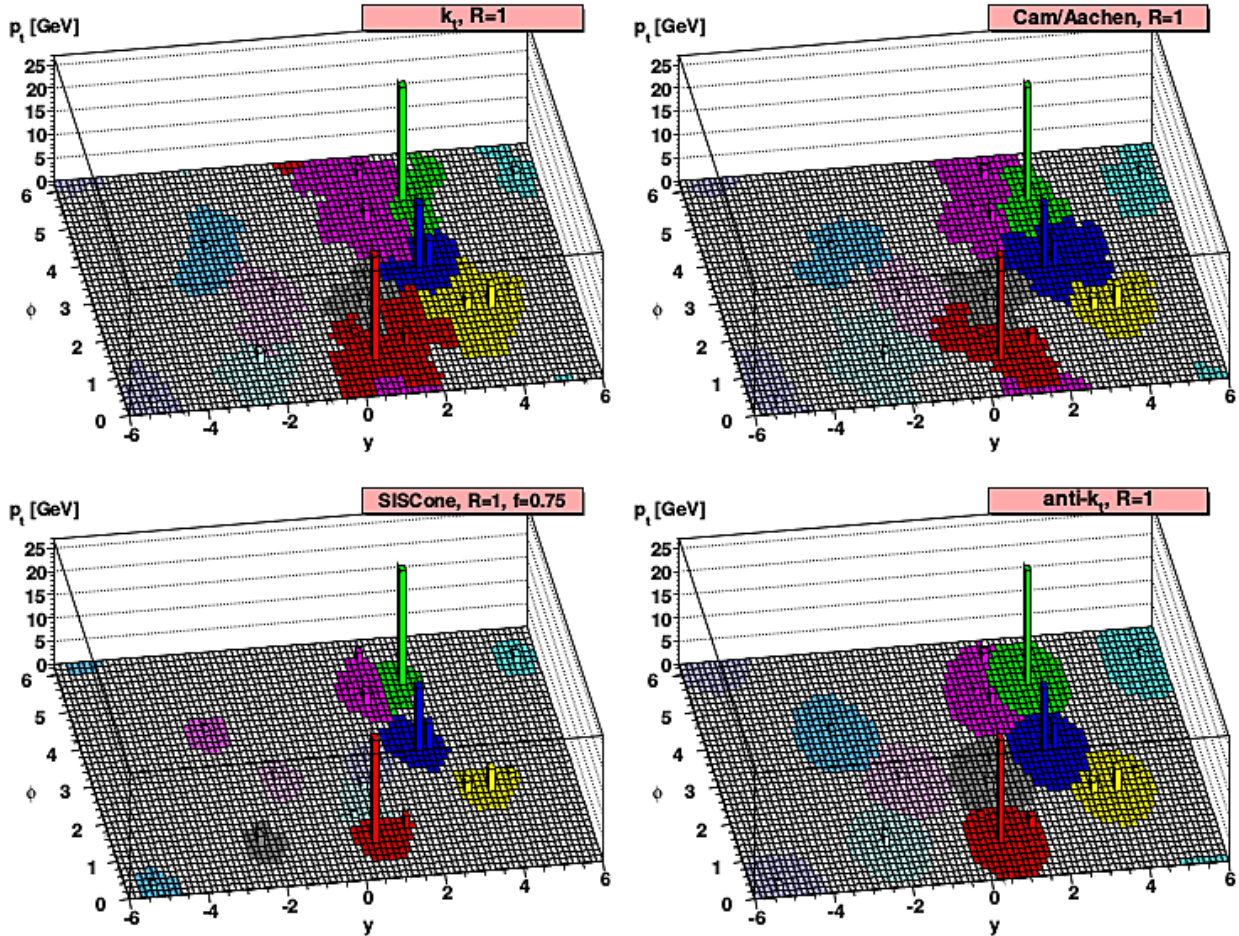


Figure 2.10: The clustering of particles, in y - ϕ space at the parton level, into jets clustered with the k_t (top left), Cambridge/Aachen (top right), SIScone (bottom left) and $\text{anti-}k_t$ (bottom right) algorithms with $R = 1$. The towers represent the jet p_T . The $\text{anti-}k_t$ algorithm gives circular jets while the jets produced with other three algorithms have irregular shapes. Taken from [35].

Chapter 3

Experimental Setup

The hadron colliders aim at search for elementary particles and the interactions acting between them as predicted by the Standard Model or beyond the Standard Model theories. For the same beam energy, higher center-of-mass energy can be achieved in the hadron colliders as compared to the fixed target experiments. Due to the availability of very high center-of-mass energy of the colliding hadrons, it becomes possible for the researchers to understand the fundamental structure of the universe deeply and to look back in its history. The masses of the Z and W bosons, discovered by the UA1 and UA2 experiments, were measured precisely at the Large Electron-Positron (LEP) collider. The proton-antiproton collider Tevatron at FNAL discovered the top quark and also measured its mass. The search for the long awaited Higgs boson was carried out by the currently running most powerful accelerator, the Large Hadron Collider (LHC). Still many questions related to the the nature of dark matter, the existence of super-symmetry (SUSY) or the extra dimensions, are yet to be answered.

The European Organization for Nuclear Research (CERN) is a world-class fundamental physics research organization founded in 1954. In the beginning, it concentrated on pure physics research to understand the inside of the atom, justifying the word “nuclear” in name. At present, the main area of research at CERN

is particle physics which studies the fundamental constituents of matter and their forces of interactions. To accomplish this task, several particle accelerators have been built by CERN which probe the physics at the TeV energy scale.

3.1 The Large Hadron Collider

The Large Hadron Collider (LHC) [45] is the world's biggest and the most powerful particle accelerator and collider built by CERN. It occupies the circular tunnel between the border of France and Switzerland which was previously used by LEP collider [46]. The circumference of the tunnel is 27 km circumference and it lies underground at a depth ranging from 50 to 175 metres (164 to 574 ft). Two beams of particles of the same kind, either protons or lead or xenon ions, are accelerated in directions opposite to each other. There are 1,232 dipole magnets to maintain the beams in their circular path. The additional 392 quadrupole magnets are present to keep the beams focused to increase the probabilities of interaction between the particles. Since this thesis presents the study done using proton-proton (pp) collisions data, we will discuss the acceleration of protons only.

The protons pass through a series of accelerators which increase their energy successively before their injection into the main ring of LHC. An overview of the various accelerators and detectors comprising the complex structure of the LHC is shown in Fig. 3.1. A bottle of hydrogen gas is the source of protons. The stripping of electrons from hydrogen gas atoms using an electric field yields protons. These protons are accelerated up to 100 keV through a radiofrequency quadrupole which provides the first focusing and a further acceleration to 750 keV energy. The linear particle accelerator (LINAC2) increases the energy of protons to 50 MeV. Then these protons are injected into the Proton Synchrotron Booster (PSB) in the form of bunches where they get accelerated to 1.4 GeV energy. The Proton Synchrotron (PS) further enhances the energy of protons to 25 GeV which is then increased to

450 GeV by the Super Proton Synchrotron (SPS). Finally the protons are injected into two beam pipelines of the main LHC ring where their energy increases to the beam energy. The total center-of-mass energy in head-on collisions between beams of same mass particles is twice the energy of the beams.

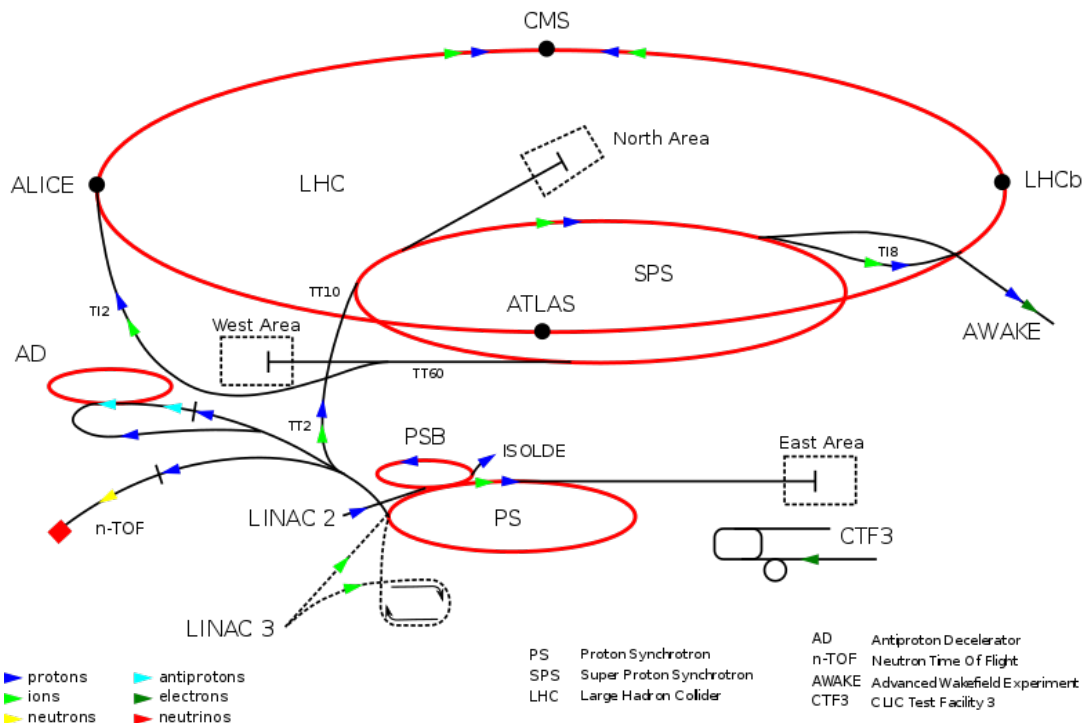


Figure 3.1: An overview of the different experiments of the Large Hadron Collider (LHC), a complex particle accelerator and collider located at CERN⁸.

The accelerated beams collide at four interaction points around which six detectors are located : ALICE (A Large Ion Collider Experiment) [47], ATLAS (A Toroidal LHC Apparatus) [48], CMS (Compact Muon Solenoid) [49–51], LHCb (Large Hadron Collider for Beauty) [52], LHCf (Large Hadron Collider forward) [53] and TOTEM (Total, elastic and diffractive cross-section measurement) [54]. The CMS and ATLAS are two general purpose detectors dedicated to the validation of the Standard Model theory predictions, existence of super-symmetry (SUSY) and

⁸Source : https://en.wikipedia.org/wiki/Large_Hadron_Collider

also looking for extra dimensions. The ALICE is a heavy-ion detector which collides lead ions to study quark-gluon plasma, a state of matter believed to be present just after the Big Bang. The LHCb experiment will explore the differences between matter and antimatter and new physics through b-quark (beauty) studies. TOTEM experiment is dedicated to cross-section measurements whereas LHCf focuses on forward physics.

The LHC successfully injected the first protons on September 10, 2008 but after few days there was magnetic quench in bending magnets which leaded to a loss of ~ 6 tonnes of liquid helium. After recovery from this incident, at first the low-energy beams circulated in the tunnel on November 20, 2009 and after three days the first collisions took place in all four detectors at $\sqrt{s} = 450$ GeV. The LHC achieved 1.18 TeV energy per beam on November 30, 2009. This made LHC the world's highest energy particle accelerator and left behind the Tevatron having record of 0.98 TeV per beam for eight years. The LHC recorded pp collisions at $\sqrt{s} = 2.36$ TeV around December 15, 2009. After this the beam energy was ramped up to 3.5 TeV on March 19, 2010 which resulted in the first pp collisions at $\sqrt{s} = 7$ TeV on March 30, 2010. The beam energy was kept at 3.5 TeV throughout 2011, and increased to 4 TeV in 2012. After a long shutdown for two years, the LHC restarted in 2015 and collided the proton beams at a much higher center-of-mass energy of 13 TeV and is running successfully till now. In the coming years, protons will be made to collide at a designed $\sqrt{s} = 14$ TeV with luminosity up to $10^{34} \text{ cm}^{-2}\text{s}^{-1}$. In this thesis, work has been carried out using the pp collisions data collected by the CMS detector at $\sqrt{s} = 8$ TeV in the year of 2012.

3.1.1 Luminosity Measurement

Luminosity (\mathcal{L}) is one of the most important parameters of an accelerator which characterizes its performance. It defines the rate at which collisions occur and is

given by the number of collisions produced in a detector per cm^2 and per second. Cross-section (σ) is a measure of the probability that an event can take place. \mathcal{L} is related to total number of events N of a process over a time period T and σ as :

$$N = \int_0^T \mathcal{L} \sigma dt = \mathcal{L}_{int} \sigma \quad (3.1)$$

where $\int_0^T \mathcal{L} dt = \mathcal{L}_{int}$ gives the total integrated luminosity. \mathcal{L}_{int} is expressed in the units of area, usually in barn^{-1} and gives a direct indication of number of events produced in a process. For example, an integrated luminosity of 10 fb^{-1} means that 10 events are produced in a process having cross-section equal to 1 fb .

The luminosity depends on the particle beam parameters as :

$$\mathcal{L} = \frac{N_b N_p^2 f_{rev} \gamma F}{4\pi \epsilon_n \beta^*} \quad (3.2)$$

where N_b is the number of bunches per beam, N_p is the number of particles in each bunch, f_{rev} is the revolution frequency of the beam, γ is the relativistic gamma factor and F is the geometric luminosity reduction factor. The effective collision area of the two beams is related to the normalized transverse beam emittance ϵ_n and the value of the betatron function β^* at the interaction point.

The CMS experiment constantly monitors the instantaneous luminosity delivered by LHC which is shown versus time in Fig. 3.2 for proton-proton collisions at nominal center-of-mass energy for the years 2010-2017. The relative instantaneous luminosity is calculated by using two methods [55] : Hadron Forward (HF) method by measuring the particle flux in the hadron forward calorimeter and Counting method where the number of reconstructed vertices in the pixel tracker are counted. The measurement of the absolute luminosity is performed using van-der-Meer scans done in special runs of the LHC [56]. The uncertainty on the measured luminosity

for 2012 data set is 2.5% (syst.) and 0.5% (stat.).

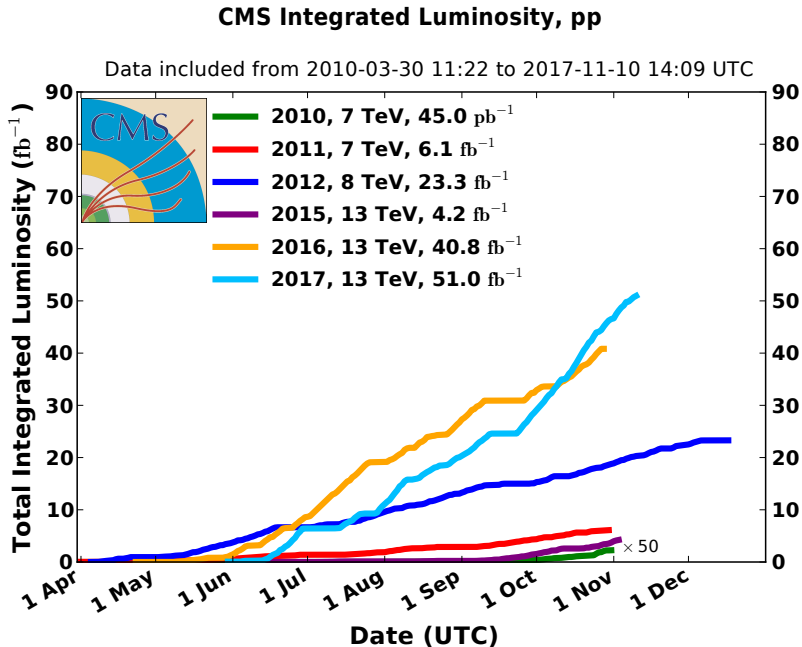


Figure 3.2: The integrated luminosity delivered by stable beams to CMS during proton-proton collisions taking place at nominal center-of-mass energy, is shown versus time for data-taking in 2010 (green), 2011 (red), 2012 (blue), 2015 (purple), 2016 (orange) and 2017 (light blue) run periods of the LHC⁹.

3.1.2 Pileup Interactions

To observe the extremely rare events, the event rate in a collider should be very high. This demands delivered luminosity to be high which is achieved by increasing the number of bunches or increasing the number of protons per bunch. However, this comes at the cost of multiple proton-proton interactions coming from independent hadron-hadron collisions occurring in the same bunch crossing, called pileup (PU) interactions. The hard interaction in every event is accompanied by a large amount of PU interactions which give rise to low p_T jets. The vertex of pileup interaction is reconstructed from tracks pointing to it as shown in Fig. 3.3. The pileup due to the

⁹Source : <https://twiki.cern.ch/twiki/bin/view/CMSPublic/LumiPublicResults>

additional collisions within a single bunch crossing is called in-time pileup whereas pileup coming from collisions other than hard scattering in other bunch crossings is known as out-of-time pileup. The pileup itself cannot be directly measured, it can be correlated to various other directly measurable quantities. The number of primary vertices (N_{PV}) is directly related to the amount of pileup as the pileup comes from the additional proton-proton interactions. The greater the N_{PV} , the more pileup energy is added to the jets which needs to be subtracted.

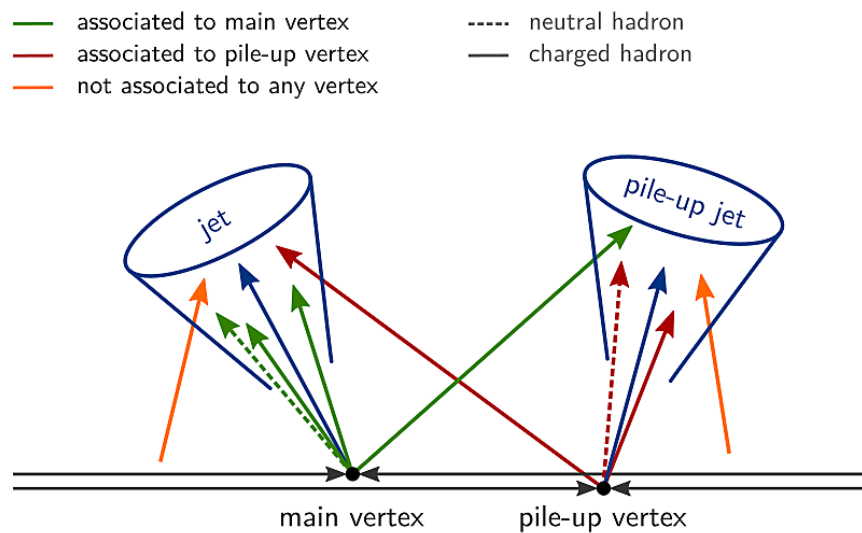


Figure 3.3: In a proton-proton collision, the particles produced from the hard interaction are clustered into a jet. The hard interaction corresponds to the main vertex. The particles produced in the interactions other than the hard one, form a pileup jet¹⁰.

3.2 The Compact Muon Solenoid

The Compact Muon Solenoid (CMS) detector is a general purpose detector located at the interaction point 5 (P5) of the main LHC ring, near the village of Cessy in France. The name of CMS comes from its compact size with main emphasis

¹⁰Source : <http://cds.cern.ch/record/1747055>

on the detection of muons and enclosed within high solenoidal magnetic field. The CMS detector aims at identifying the different types of particles produced in proton-proton and heavy ion collisions and measuring their energies and momenta. This is achieved by concentric layers of different sub-detectors arranged in a cylindrical complex structure with 21.6 m length and 15 m diameter. The silicon-based tracker surrounds the the interaction point and forms the innermost layer. After the tracker, there are layers of a scintillating crystal electromagnetic calorimeter (ECAL) and a sampling hadron calorimeter (HCAL). The calorimeters are enclosed inside the superconducting solenoid. Outside the magnet lies the large muon detectors embedded inside an iron yoke. The three dimensional view of the CMS detector

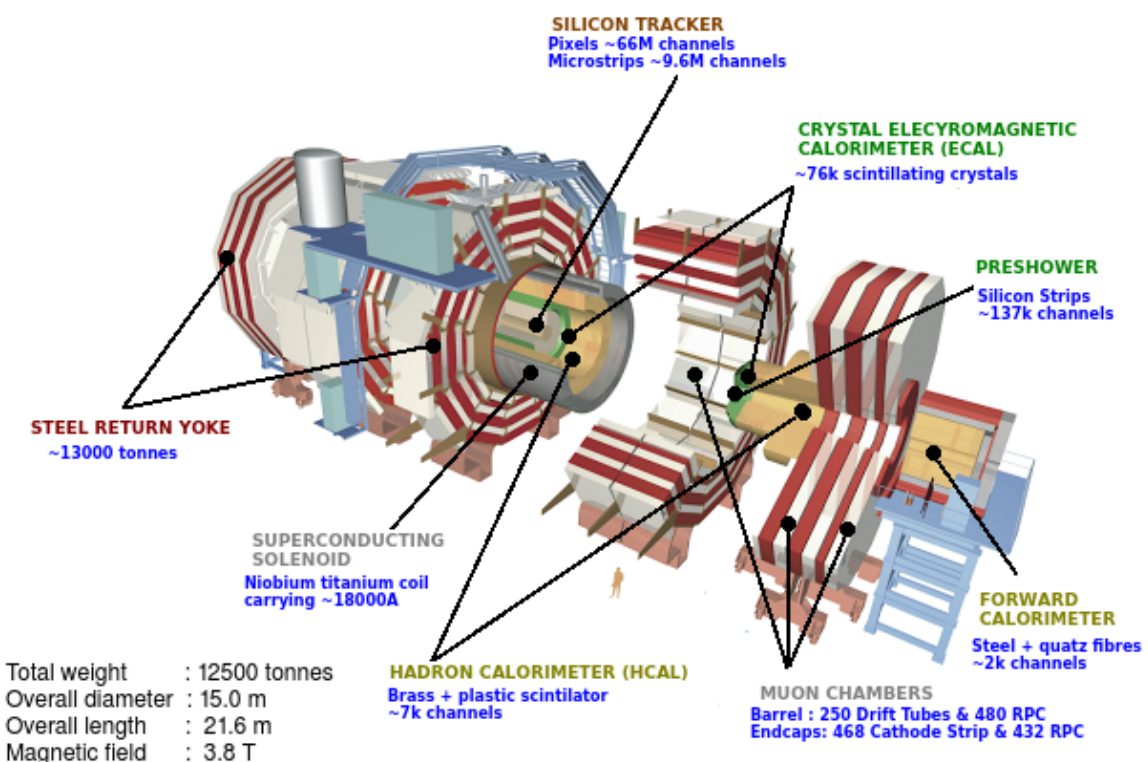


Figure 3.4: The three dimensional view of the CMS detector along with its sub-detector components¹¹.

¹¹Source : <https://orbiterchspacenews.blogspot.in/2013/04/cern-cms-prepares-for-future.html>

along with its components is presented in Fig. 3.4. The CMS was constructed in parts at ground and assembled later on in the cavern. The components are easily accessible for upgrades or repairs as the detector can be opened up into movable slices. Figure 3.5 shows the front view of the CMS detector differentiating individual components which contribute to event reconstruction. The dashed and solid lines represent the invisible and visible tracks, respectively, of the reconstructed particles. The different particles are : photons (γ), muons (μ^\pm), electrons (e^-), neutrons (n) and charged hadrons (π^\pm).

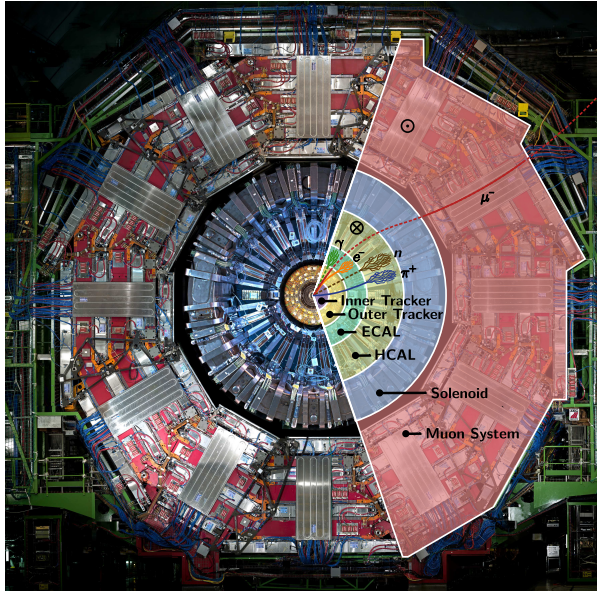


Figure 3.5: Front view of the CMS detector along with its components : inner tracker, outer tracker, electromagnetic calorimeter, hadronic calorimeter, solenoid and muon system. The path of different particles detected by dedicated sub-detectors are shown by dashed (invisible track) and solid (visible track) lines. \otimes and \odot gives the direction of magnetic field inside the solenoid and in the return yoke, respectively. Taken from [51].

A brief overview of the CMS detector has been presented and the details of the its design as well as physics performance are available in Ref. [50, 51]. Before going into the details of each sub-detector, first the CMS coordinate system is described in the next section.

3.2.1 Coordinate System

A right-handed coordinate system, illustrated in Fig. 3.6, is used by the CMS detector. The origin of the co-ordinate system lies at the nominal interaction point (IP) of the collisions. The x -axis points horizontally from the IP and towards the center of the LHC ring. The y -axis points vertically upwards and the z -axis along the beam direction towards the Jura mountains. Following customary polar coor-

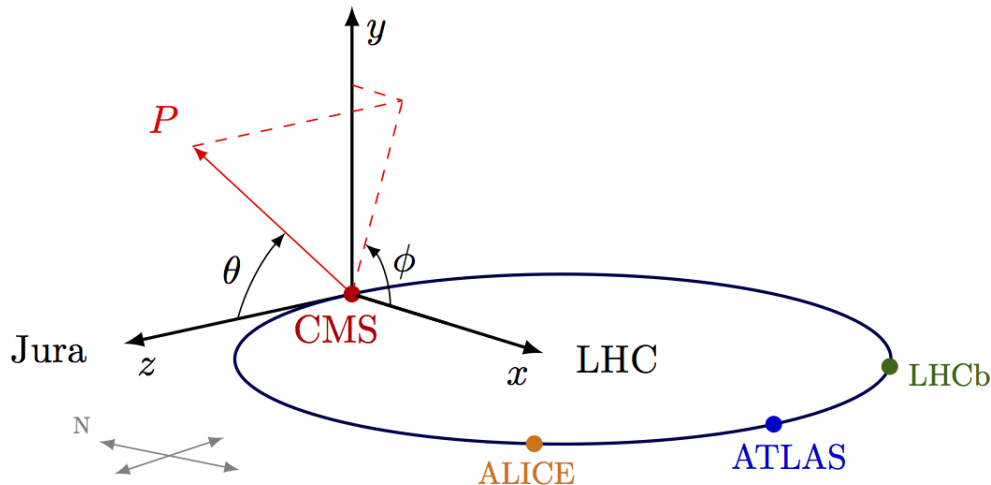


Figure 3.6: The CMS detector uses the right-handed coordinate system¹² having origin at the interaction point (IP). The x -axis points horizontally from the IP towards the center of the LHC ring, the y -axis points vertically upwards whereas the z -axis along the beam direction towards the Jura mountains. The azimuthal angle ϕ is measured from the x -axis in the x - y plane and the polar angle θ is calculated from the z -axis in the z - y plane.

dinate conventions : the azimuthal angle ϕ is measured from the x -axis in the x - y plane as $\phi = \tan^{-1}(\frac{y}{x})$ where $\phi = 0$ points to the $+x$ axis and $\phi = \pi/2$ points to the $+y$ axis. The polar angle θ , is calculated from the z -axis in the z - y plane as $\theta = \tan^{-1}(\frac{x^2 + y^2}{2})$ with $\theta = 0$ corresponding to the $+z$ direction and $\theta = \pi$ to the $-z$ direction. The quantities pseudorapidity η and the rapidity y are preferred over the angles θ and ϕ . The pseudorapidity and rapidity are given by Eq. 3.3. Both the

¹²Source : https://wiki.physik.uzh.ch/cms/latex:example_spherical_coordinates

quantities are equal for massless particles.

$$\begin{aligned}\eta &= -\ln\left(\tan\left(\frac{\theta}{2}\right)\right) \\ y &= \frac{1}{2} \ln\left(\frac{E + p_z}{E - p_z}\right)\end{aligned}\tag{3.3}$$

The difference between rapidities Δy is invariant under longitudinal Lorentz boost whereas it does not hold for η . Hence y is considered in this thesis. The angular distance between the two particles is defined by $\Delta R = \sqrt{(\Delta\eta)^2 + (\Delta\phi)^2}$. The momentum component transverse to the direction of beam p_T , is computed from the x - and y -components as $p_T = \sqrt{p_x^2 + p_y^2}$ and the transverse energy is given by $E_T = E \sin\theta$. After introducing the CMS coordinate system, further the detector subsystems are described briefly in the following sections. In Fig. 3.7, a longitudinal section of the CMS detector shows the location of different sub-systems along with the superconducting solenoid, in the y - z plane.

3.2.2 Inner Tracker System

The charged particles produced from the LHC collisions leave their trajectories as they move outward from the interaction point. The particle flux within the detector decreases as $1/r^2$. So the tracks of the particles need to be measured as close to the collision point as possible and in a precise manner. The innermost tracking system of the CMS consists of silicon detectors and measures the hits produced by the charged particles. It surrounds the interaction point and has a cylindrical volume of length of 5.8 m and a diameter of 2.5 m and covers a pseudorapidity range up to $|\eta| < 2.5$. The passage of the charged particles through the silicon detector material produces small ionization currents which get detected as hits. Such multiple hits when combined, reconstruct the track which gives the information about the direc-

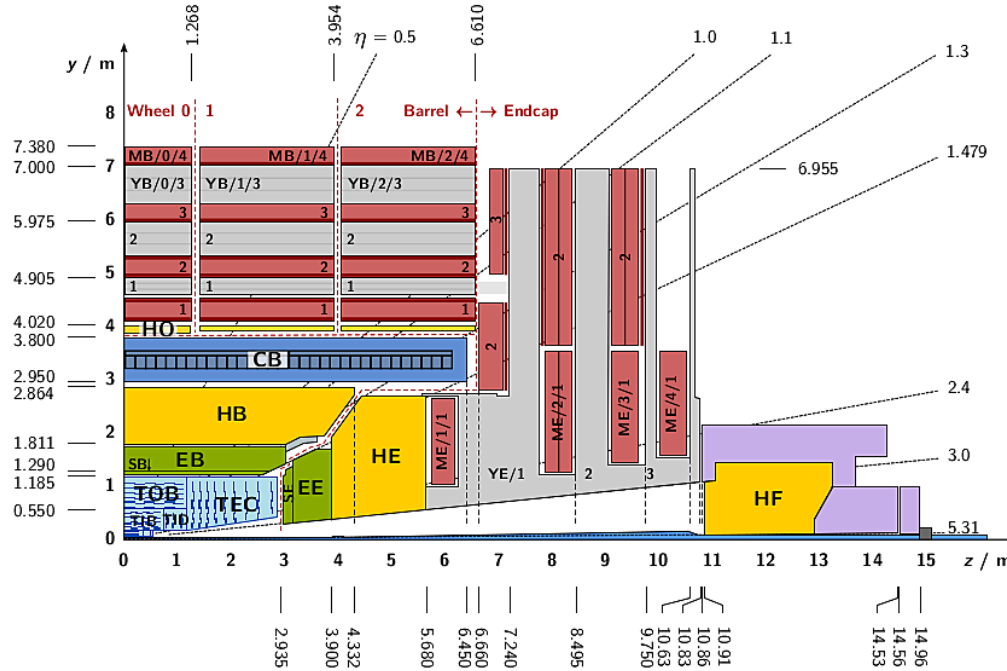


Figure 3.7: A longitudinal view of the CMS detector is shown in the y - z plane¹³. It shows the tracking detector (TIB, TID, TOB, TEC) close to the nominal interaction point at $(0,0)$, the electromagnetic (EB, EE) and hadronic (HB, HE, HO, HF) calorimeters. The coil of the solenoid magnet (CB) surrounds the inner barrel region. The iron return yoke (YB, YE) is interleaved with the muon chambers (MB, ME).

tion and transverse momentum p_T of the charged particle. Silicon detectors have a much higher resolution in tracking charged particles as compared to the older ones such as cloud chambers or wire chambers. CMS inner tracking system shown in Fig. 3.8 consists of two sub-systems :

Pixel Detector - A pixel detector is located close to the beam pipe. It has three co-centric barrel layers lying at radii of 4.4, 7.3 and 10.2 cm from the beam pipe. It has two disks of pixel modules on each side of barrel. Taking the design luminosity of LHC i.e. $10^{34} \text{ cm}^{-2}\text{s}^{-1}$, about 1000 particles are produced from more than 20 overlapping proton-proton collisions. These particles traverse through the tracker

¹³Source : <http://cds.cern.ch/record/1747055>

for each bunch crossing, i.e. every 25 ns. The size of each pixel is $100 \mu\text{m} \times 150 \mu\text{m}$ which gives an average occupancy of 10^{-4} per bunch crossing. Due to the large Lorentz effect, the pixel tracker has a resolution of $10 \mu\text{m} \times 20 \mu\text{m}$ which is beneficial for a precise determination of the primary and secondary vertices and good momentum resolution.

Strip Detector - After coming out of the pixel detector the charged particles traverse through ten layers of silicon strip detectors, reaching out to a radius of 130 cm. The silicon strip detector has four layers of inner barrel (TIB) assembled in shells with two inner endcaps (TID), each having three small discs. There is an outer barrel tracker (TOB) consisting of six concentric layers. Finally two endcaps (TEC) are placed at the end of tracker. Each part of the tracker has silicon modules which are designed with dedicated functions. The strip detector performs the measurement of the particle tracks with a reduced resolution of $23 \mu\text{m}$ which hints the smaller particle flux at larger distances from the collision point. The active silicon

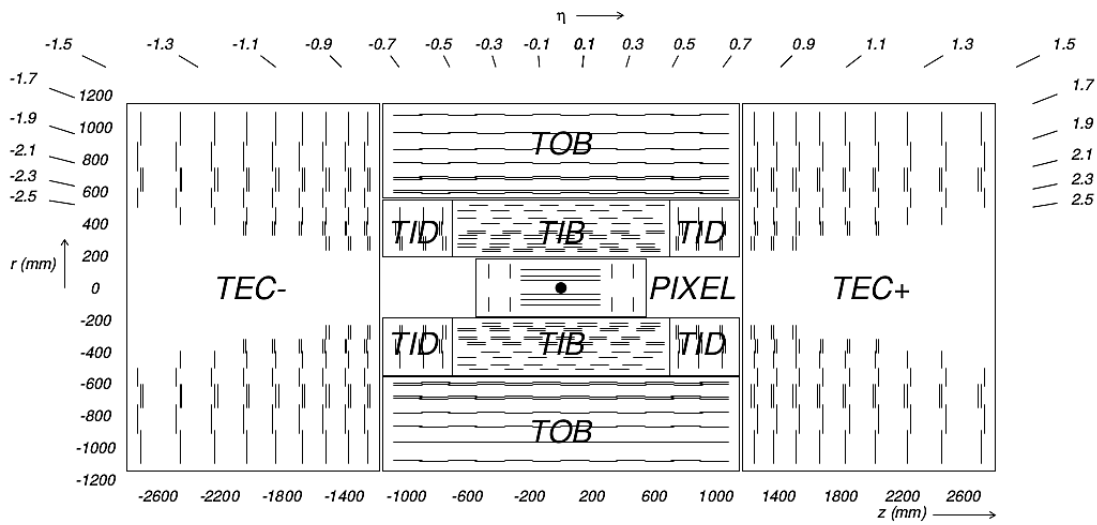


Figure 3.8: A longitudinal view of the inner tracking system is shown in r - z plane. The CMS tracking system is made up of the silicon pixel detector and the silicon strip detector. The silicon strip detector has four components : The Tracker Inner Barrel (TIB) complemented by the Tracker Inner Disks (TID) which are further surrounded by the Tracker Outer Barrel (TOB) in barrel region. Tracker End Cap (TEC) covers high η ranges up to $\eta = 2.5$. Taken from [49].

area of CMS tracker is about 200m^2 which makes it the largest silicon tracker. Along with the measurement of tracks, the energy also needs to be measured for which the calorimeters are present outside the tracker. The tracker should interfere with the particles to a minimum extent so that their momentum can be measured precisely but to measure their energy, they are required to interact with the calorimeters fully.

3.2.3 Electromagnetic Calorimeter

The electromagnetic calorimeter (ECAL) is a homogeneous and hermetic calorimeter used to slow down the produced photons and electrons/positrons and measure their energy by absorbing them into the detector material. The barrel part of the ECAL is made up of 61200 lead tungstate (PbWO_4) crystals and each of the two end caps has 7324 crystals. PbWO_4 is a very dense material having a short radiation length of $X_0 = 0.89 \text{ cm}$ and covers the pseudorapidity up to $|\eta| < 3.0$. The particles interact with matter and produce electromagnetic shower through the subsequent processes of bremsstrahlung and electron-positron pair production. The energy of the particles deposited by the photoelectric effect and the Compton scattering causes excitation of the material atomic state and the emission of photons. These emitted photons are detected by silicon avalanche photo diodes (APDs) in the barrel region and vacuum phototriodes (VPT) in the end-cap region. The number of created photons gives the direct measure of energy of the incident particles. The incorporation of oxygen makes it highly transparent and enables to emit scintillation light. The small Molière radius of 2.19 cm gives a fine granularity. These properties leads to compact size of ECAL so that it can be easily placed within the solenoid magnet.

Figure 3.9 presents a geometric view of ECAL in the y - z plane showing the arrangement of different parts of ECAL : the ECAL barrel (EB) extending up to $|\eta| < 1.479$ using more than 60000 crystals and ECAL endcaps (EE) covering the region $1.479 < |\eta| < 3.0$ with an additional 15000 crystals. The preshower detectors (ES) made of lead absorbers and silicon detectors are put in front of the endcaps to

distinguish high energetic single photons from low energetic photon pairs originating from neutral pions decays.

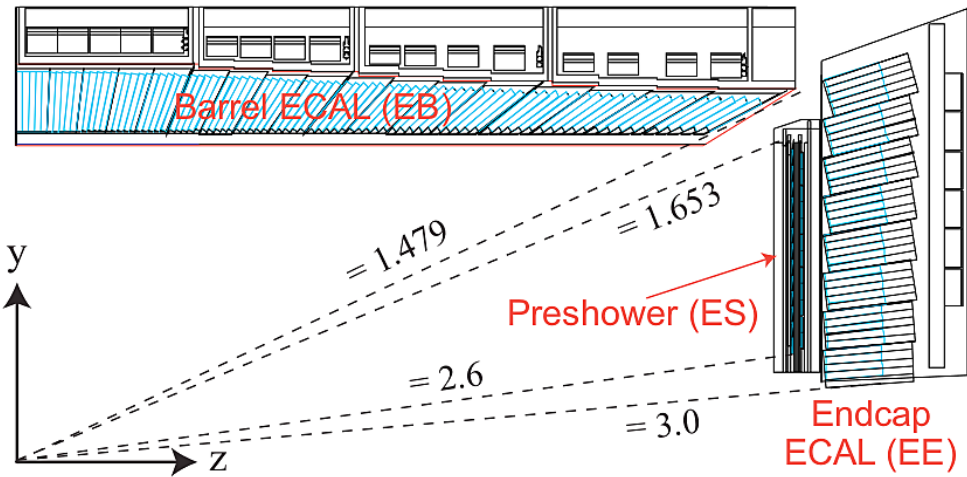


Figure 3.9: A geometric view of one quarter of the electromagnetic calorimeter (ECAL) in y - z plane showing the arrangement of sub-modules covering the barrel region (EB) and the endcaps (EE). ECAL is complemented with preshower detector (ES) mounted in front of the endcaps. Taken from [50].

The relative energy resolution of the ECAL has been measured to be [57] :

$$\left(\frac{\sigma(E)}{E}\right)^2 = \left(\frac{2.8\%}{\sqrt{E}}\right)^2 + \left(\frac{12\%}{E}\right)^2 + \left(0.30\%\right)^2 \quad (3.4)$$

where E is the energy in GeV. The first term is the stochastic component caused by fluctuations in the energy deposited in the preshower absorber and lateral shower containment. The second term is the contribution by noise and the last is the constant term which comes from leakage of energy from the back of the crystal, inter-calibration errors and non-uniformity of the longitudinal light collection.

3.2.4 Hadronic Calorimeter

At CMS, the major fraction of the particles produced in proton-proton collisions is hadrons. The combined CMS calorimeter system measures the energies and di-

rections of particle jets which indirectly give the energies and directions of quarks, gluons and neutrinos. The neutral hadrons do not leave track and hence their energy is measured by taking into account the missing transverse energy (E_T^{miss}). The determination of E_T^{miss} is a crucial tool in searching the new particles and phenomena. The hadron calorimeter (HCAL) mainly focuses on the identification of hadron jets, neutrinos as well as electrons, photons and muons in conjunction with the ECAL and the muon system. Hence HCAL is an essential sub-system of the CMS detector and contributes to most of CMS's physics studies.

HCAL is a sampling calorimeter installed inside the solenoid coil. It consists of non-magnetic brass absorber with a short interaction length of $\lambda_I = 16$ cm and is interleaved with plastic scintillators having wavelength-shifting (WLS) fibres as readout. The highly energetic hadrons further produces a large number of pions and nucleons by inelastic interactions. The hadronic shower spreads more than the electromagnetic showers because of large transverse momentum of the secondary particles. As the energy of the particles is lower than a certain threshold, the ionization and low-energy hadronic processes come into play. The active scintillation material excites and blue-violet light is emitted. The wavelength shifters connects all scintillators to photodiodes and read out the signals and further pass them to the data acquisition system. The longitudinal view of one quarter of the HCAL presented in Fig. 3.10 shows the different parts :

Hadron Barrel - The hadron barrel (HB) is divided into two identical half barrel sections on either side of the interaction point. Each half barrel is made of 18 azimuthal wedges which are further divided into four azimuthal sectors each giving a granularity of $\Delta\phi = 0.087$. In z direction, the plastic scintillators are divided into 16 intervals of granularity $\Delta\eta = 0.087$. HB covers the region up to $|\eta| < 1.305$ and overlaps with endcaps for $1.305 \leq |\eta| \leq 1.392$. Since HB has the highest resolution ($\Delta\eta \times \Delta\phi = 0.087 \times 0.087$), it is the optimal for calibration of the jet energy scale. The thickness of the HCAL amounts to 7-11 interaction lengths which are

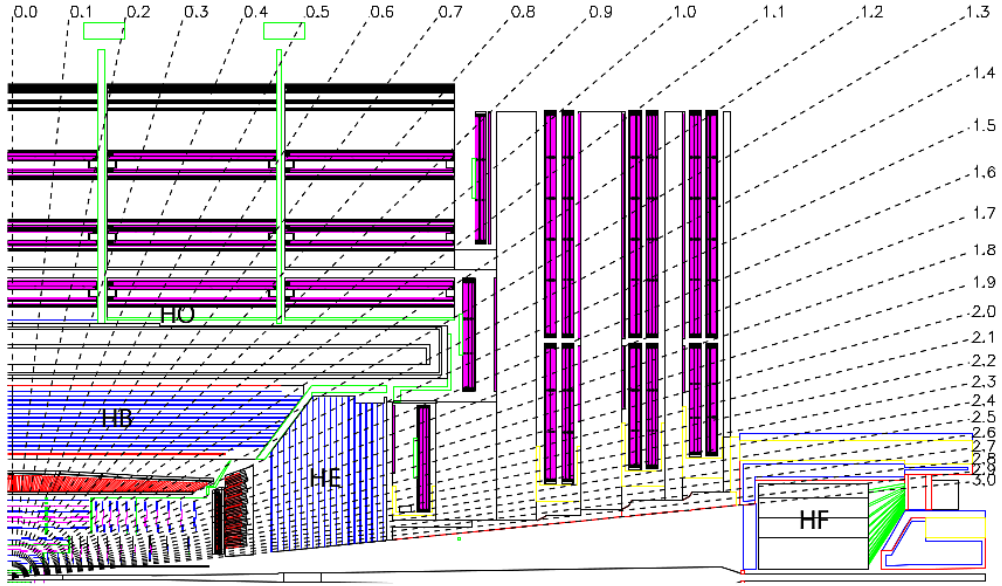


Figure 3.10: Longitudinal section of one quarter of the hadronic calorimeter (HCAL) in r - η plane. It consists of different parts : hadron barrel (HB), hadron outer (HO), hadron endcap (HE) and hadron forward (HF). Taken from [49].

sufficient enough to absorb most of the hadrons.

Hadron Outer - The total amount of material in barrel region to absorb the hadronic shower is not sufficient. This requirement is fulfilled by placing an outer hadron (HO) calorimeter as a tail catcher on top of the coil of the magnet. The HO uses the solenoid coil as an additional absorber having interaction lengths of $1.4/\sin\theta$ and measures the tails of hadron showers penetrating the HB and the coil. Since the HO is physically located inside the muon system, it is strongly constrained by its geometry. The muon system is subdivided into 5 rings along the z -axis. Each of these rings is 2.536 m wide in z -direction and the HO is placed as first sensitive layer in these rings, with a scintillator thickness of 10 mm. The central ring ($\eta = 0$) has two scintillator layers placed on each side of 19.5 cm thick iron layer.

Hadron Endcap - The hadron endcaps (HE) extend the pseudorapidity range up to $|\eta| < 3.0$. About 34% of the particles produced in the final state reach this

region. The granularity in $\Delta\eta \times \Delta\phi$ is 0.087×0.087 up to $|\eta| < 1.6$ and 0.17×0.17 for $|\eta| > 1.6$. The main challenges faced in the construction of the HE were the use of non-magnetic material in order to not disturb the magnetic field and the close distance to the beam line. The continuous damages caused by radiations decrease the detector response which should be monitored at regular intervals.

Hadron Forward - The hadron forward (HF) calorimeter lies at a distance of $z = \pm 11.2$ m from the interaction point, covering the $2.8 < |\eta| < 5.2$ region. The HF has a cylindrical structure with an outer radius of 130.0 cm. It is azimuthally subdivided into 36 20° modular wedges. The HF is made up of 5 mm thick grooved steel plates which have quartz fibers inserted into the grooves. The fibres running parallel to the beam line are bundled to form 0.175×0.175 ($\Delta\eta \times \Delta\phi$) towers. The HF detects the jets having very high η and also the hadronization products of the beam remnants. The iron absorbers and quartz fibers act as active material to measure the emitted Cerenkov light and to produce the signal in the photomultipliers (PMT).

The relative hadronic energy resolution of the barrel HCAL and ECAL combination can be parametrized as :

$$\left(\frac{\sigma(E)}{E}\right)^2 = \left(\frac{a}{\sqrt{E}}\right)^2 + b^2 \quad (3.5)$$

where a is a stochastic term and b is a constant term. These values have been measured [58] as $a = (0.847 \pm 0.016) \sqrt{\text{GeV}}$ and $b = 0.074 \pm 0.008$ whereas for HF the measured values are $a = 1.98 \sqrt{\text{GeV}}$ and $b = 0.09$.

3.2.5 Superconducting Magnet

The superconducting magnet is an essential feature of the CMS detector which is 13m long and 6m in diameter. Its refrigerated superconducting high-purity

aluminium-stabilized niobium-titanium coils cooled at 4 Kelvin produces a magnetic field of 4 Teslas (T). The magnet will run at 3.8 T in order to maximize its lifetime. This intense solenoidal field makes the compactness and cylindrical symmetry of the detector possible. The magnet is placed between the calorimeters and the muon system. The solenoidal magnetic field parallel to the beam bends the tracks of the high momentum charged particles in the transverse plane. The curvature of the trajectory increases with the strength of the magnetic field which make possible to determine the transverse momentum more precisely. The magnet is complemented by an iron yoke (~ 10000 tonnes) which returns the magnetic field at 2 T.

3.2.6 Muon System

As the name of CMS suggests, the detection of muons is of central importance in the CMS detector. Out of all the known stable particles, only the muons and neutrinos pass through the calorimeter without depositing their energies. They interact very little with matter and can travel long distances through the dense matter. The charged muons can be detected by having an additional tracking system outside the calorimeters whereas the neutrinos are practically undetectable as they escape completely without being tracked in any of the layers of the calorimeters. Their presence can be detected from the missing energy carried by them. The CMS muon system is installed outside the calorimeters in the iron return yoke of the magnet which act as a hadron absorber for the identification of the muons. Along with the muon identification, the muon system also measures their momenta and is also used for the triggering purposes. Good muon momentum resolution and trigger capability are enabled by the high-field solenoidal magnet and its flux-return yoke. The CMS muon system measures the momenta and charge of muons over the entire kinematic range of the LHC. The muon system shown in Fig. 3.11 consists of three types of gaseous particle detectors :

Drift Tube - The muon barrel (MB) detector has four concentric layers of drift

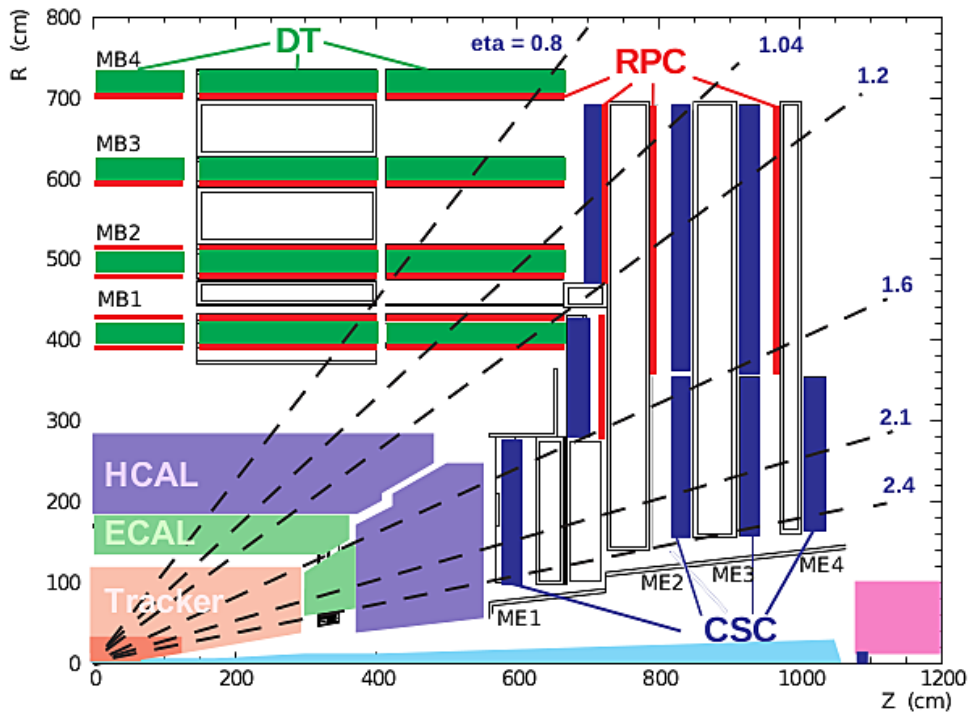


Figure 3.11: A longitudinal view of the CMS muon system showing the location of the three gaseous particle detectors : four Drift Tube (DT) stations in the barrel (MB1-MB4, green), four stations of Cathode Strip Chambers (CSC) in the endcap (ME1-ME4, blue), and the Resistive Plate Chambers (RPC) stations (red)¹⁴.

tube (DT) chambers inside the iron yoke which covers the region up to $|\eta| < 1.2$. DT stations are distributed into 5 wheels along the z direction. Each wheel is divided into 12 sectors, each covering a 30° azimuthal angle. The DT is an aluminium tube having length of 2.5 m and area of $4.2 \times 1.3 \text{ cm}^2$. It is filled with a gas mixture consisting of 58% Ar + 15 % CO₂.

Cathode Strip Chambers - In the forward region, the muon and background flux is higher. In this region, cathode strip chambers (CSC) are preferred because of their fast response time, high radiation tolerance and fine segmentation. In each end cap, four stations of CSCs are installed which cover the region of $0.9 < |\eta| < 2.4$.

¹⁴Source : <https://arxiv.org/abs/1209.2646>

Each CSC is trapezoidal in shape and consists of 6 gas gaps. Each gap has a plane of radial cathode strips and a plane of anode wires lying in perpendicular direction to the strips.

Resistive Plate Chambers - Both DT and CSC are accompanied by resistive plate chambers (RPC) which are double-gap chambers. RPCs operate in avalanche mode to ensure good performance at high rates. They help to resolve ambiguities in attempting to make tracks from multiple hits in a chamber. They also provide additional points for determination of a muon trajectory and give fast response to the trigger system which is described in the following section.

3.2.7 Trigger and Data Acquisition System

At the LHC, the interaction rates in proton-proton collisions are very high. In the 2012 run period, the beam crossing frequency was 25 ns. At this frequency, around 40 million bunch crossings occur per second with an average of around 20 collisions per bunch crossing. But the rate at which the information can be stored is much lower than collision rates. Hence, either the storage rate should be increased or event rates should be decreased. This is achieved by using an efficient trigger system which retains the interesting signal events and rejects the background events. An event should be accepted or rejected very quickly, based on signals of certain physics. CMS has a two-level complex trigger system :

Level-1 Trigger - The Level-1 (L1) trigger system is based on custom electronics which stores the events at maximum rate of 100 kHz and then forward them to the next level triggers. The L1 system uses only coarsely segmented data from calorimeter and muon detectors and holds all the high-resolution data in pipeline memories in the front-end electronics. The work flow of the L1 trigger system, consisting of local, regional and global components, is shown in Fig. 3.12. The local triggers known as Trigger Primitive Generators are based on energy deposits in calorimeter trigger

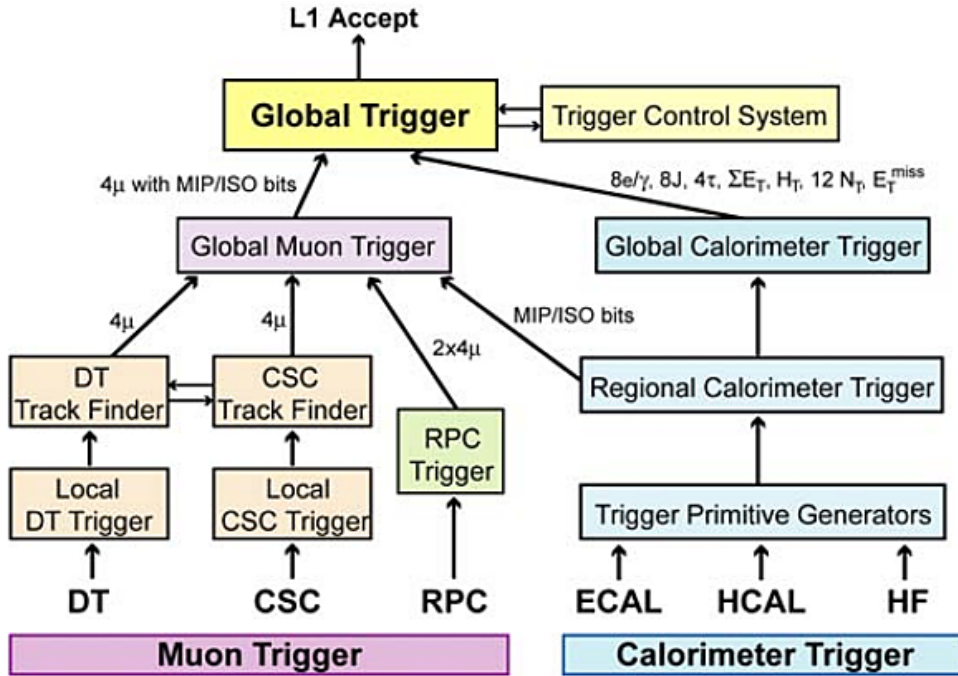


Figure 3.12: Work flow of the L1 trigger system consisting of local, regional and global components. Taken from [49].

towers and tracks in muon chambers. The Regional Triggers combine their information and use pattern logic to determine ranked and sorted trigger objects such as electron or muon candidates in limited spatial regions. The rank is determined as a function of energy or momentum and quality, which reflects the level of confidence attributed to the L1 parameter measurements, based on detailed knowledge of the detectors and trigger electronics and on the amount of information available. The Global Calorimeter and Global Muon Triggers determine the highest-rank calorimeter and muon objects and transfer them to the Global Trigger (GT), the top entity of the Level-1 hierarchy. The events accepted by the GT are further evaluated by the HLT.

High Level Trigger - At the second step, a software-based High-Level Trigger (HLT) reduces the maximum L1 accepted rate of 100 kHz to a final output rate of 100 Hz. The HLT system filter events by performing physics selections based on the

offline reconstruction software. The on-line processor farm provides the HLT and a fraction of the accepted events are passed to the Data Acquisition (DAQ) system for further processing.

3.2.7.1 Jet Triggers

At CMS, there are various types of triggers depending on the analysis to be performed. The triggers based on jet properties and missing transverse energy (E_T^{miss}) are important for search for new physics whereas the single-jet triggers are mainly designed to study quantum chromodynamics (QCD). This thesis uses the single-jet triggers to select the events for analysis. At L1, the single-jet triggers use information mainly from the calorimeters by looking for the highest energy deposit. The sums of transverse energy from ECAL and HCAL are computed in 4×4 trigger towers, except in the HF region where this quantity is measured in the whole trigger tower itself. If the calculated sum is greater than a certain threshold, the event is selected at L1 and it is passed to the HLT. At HLT level, the jets are reconstructed using the anti- k_t jet clustering algorithm. The inputs to the jet algorithm are either calorimeter towers giving “CaloJet” objects, or the reconstructed particle flow objects giving “PFJet” objects. The processing of reconstruction algorithm takes a long time and hence the jet trigger paths are divided into multiple selection steps. At first, the jets are reconstructed from calorimeter towers. The PF algorithm is run only for events in which at least one calorimeter jet passes a certain p_T threshold. The jets are then again clustered again from the PF candidates. In 2012, most of the jet trigger paths take PFJets as their inputs. The rate of jet events is quite high, so PFJet trigger paths have a pre-selection based on CaloJets. The matching between CaloJets and PFJets is required in single PFJet paths. Due to the flexibility of the HLT, it is possible to apply the jet energy corrections during the HLT selection.

3.2.7.2 Data Acquisition System

As the L1 trigger accepts events at a rate of 100 kHz, the Data Acquisition (DAQ) system has to process the events at the same speed. It reads out the data of all detector sub-components and assembles the complete events, see Fig. 3.13. The data is subsequently passed to the HLT which further reduces the rates to a few hundred events per second. Finally, the events are merged and saved to a local storage system, from which they are continuously transferred to the Tier-0 computing center at CERN.

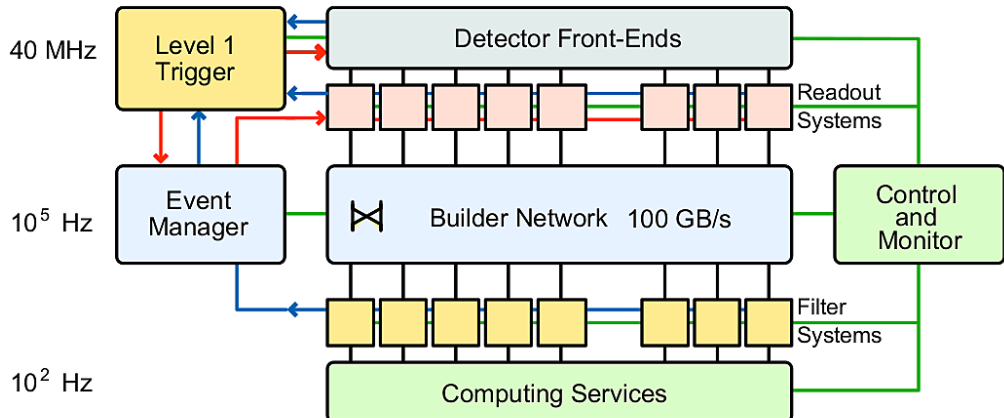


Figure 3.13: Architecture of the CMS Data Acquisition (DAQ) system. Taken from [49].

3.2.8 Data Management

Although the trigger system reduces the collision rate enough to be stored in tape, still there is a huge amount of data need to be analyzed. An efficient computing infrastructure and the software is required for storing and distributing the data. To meet this need, the LHC has a data storage infrastructure called the Worldwide LHC Computing Grid (WLCG) [59]. WLCG provides a hierarchical structure, as shown in Fig. 3.14, in a series of four levels or Tiers. Each Tier is made up of several computer centres. All the raw collision data collected by CMS is converted

into a format suitable for offline analysis and sorted in the form of data sets at the Tier-0 site at CERN. This processed data is then transferred to Tier-1 centers all over the world where reconstruction algorithms are run. Further reconstructed and simulated data is distributed to Tier-2 sites, where it is available for physics analysis mainly performed on Tier-3 sites.

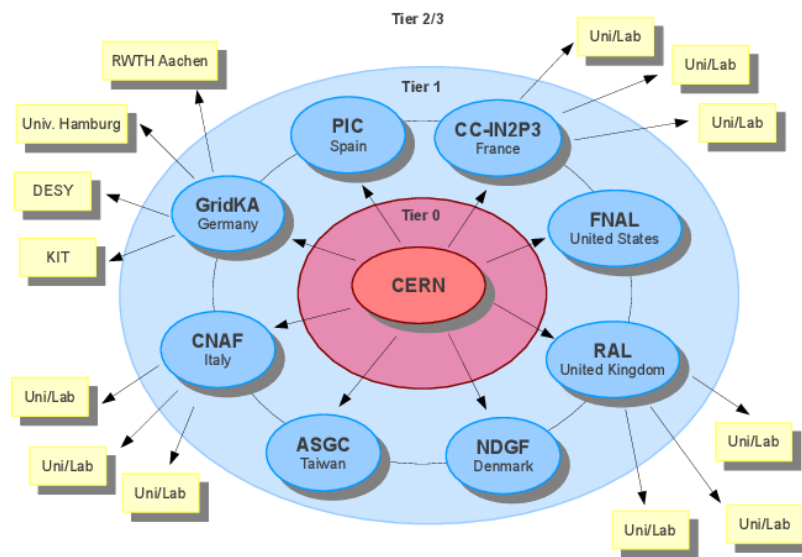


Figure 3.14: The schematic overview of the CMS computing grid. All data collected by CMS is stored at the Tier-0 site at CERN which is then transferred to Tier-1 centers all over the world. Further reconstructed and simulated data is distributed to Tier-2 sites, where it is available for physics analysis mainly performed on Tier-3 sites. Taken from [59].

3.3 Software Tools

Every year, the CMS is recording a huge amount of collision and simulation data. This data is analyzed iteratively to improve the understanding of the detector and the measured physics. So a dedicated data structure and software tools are required for data analysis. These are included in the software framework referred to as CMSSW framework.

3.3.1 CMSSW Framework

The CMS software framework (CMSSW) [60] provides all necessary tools required to perform a physics analysis. It is built on top of an event data model (EDM). It is a container for arbitrary C++ objects, e.g. recorded raw data and reconstructed physical objects or derived physical quantities of an event. The reconstruction algorithms in the CMSSW framework are divided into modules, which can be dynamically loaded and run. The event processing model in CMSSW is run by one executable, called cmsRun. SCRAM (Source Configuration, Release, And Management) is a configuration and management tool in the framework. It builds a runtime environment and make available all the necessary shared libraries. The shared libraries reduces memory consumption by loading only required modules during runtime. The CMSSW framework performs calibration, event generation, detector simulation, event reconstruction as well as data analysis by implementing the codes either in C++ or Python languages. To reduce the event content, a process called skimming is performed where only necessary data is preserved.

3.3.2 ROOT

ROOT [61] is an open source object-oriented data analysis framework, developed by CERN. It consists of a huge C++ library provided with all the functionalities to store and analyze large amounts of data. It provides histogramming methods in 1, 2 and 3 dimensions, curve fitting functions, minimization procedures, graphics and visualization classes. The command language of ROOT is command line interpreter (CINT), with several extensions to C++ which makes ROOT a versatile package. ROOT can be extended dynamically by linking external libraries. The events generated or analyzed in CMSSW framework are stored in a tree structure in files using ROOT libraries. In this thesis, ROOT has been used extensively for storing information of events or objects, for analyzing the events, for fitting as well as plotting purposes.

3.3.3 NLOJET++ and FASTNLO

The cross-sections for jet production at leading order (LO) and next-to-leading order (NLO) are evaluated using a C++ program called NLOJET++ [62, 63]. It uses the dipole subtraction method for the separation of the divergences and can calculate up to three-jet observables at NLO precision. The perturbative QCD cross-sections are calculated using Monte Carlo integration methods which are very time consuming. It makes PDF fits or estimations of uncertainties difficult where the calculations of the cross-sections are need to be repeated. So the NLOJET++ is interfaced to the FASTNLO project [64, 65] which performs fast re-evaluations of cross-sections. It stores the perturbative coefficients obtained with NLOJET++ in a way that the strong coupling constant and the PDFs can be changed afterwards without a recalculation of the perturbative coefficients.

All the event generators and cross-section calculation tools takes the PDFs as an input. They are either hard coded in the generators or accessed via a standardized interface with the LHAPDF library [66, 67]. LHAPDF provides a unified and easy way to use the PDF sets by storing them in data files. It provides interpolation routines to read the PDFs and interpolate the PDFs at all scales. It also allows access to single PDF members without needing to load whole sets. LHAPDF is supported by many MC event generators and other physics programs.

Chapter 4

Event Generation, Simulation and Reconstruction

Event simulation plays a significant role in the operation of any experiment. Before the real data taking, the reconstruction algorithms, efficiency of trigger paths, analysis strategies and other operational details of the experiment need to be studied and optimized well. This is achieved by simulation of the apparatus and the expected processes using the Monte Carlo (MC) method [68]. In high energy physics, the simulation of experimental data is done in two steps : event generation and detector simulation. Event generators simulate a collision starting from the proton-proton interaction up to the production of the final decay products, to be observed with the detector. The output of an event generator is taken as input in a detector simulation program which models the interactions between the generated final-state particles and the detector. This requires a sophisticated and complex simulation of the detector material and the behaviour of the interacting particles.

4.1 Event Generation and Simulation Software

In real world, the machine or collider produces interactions which are observed by detectors. The interesting events are stored and reconstructed afterwards for a

physics analysis. In the MC world, the role of machines is played by the event generators. The event generators generate simulated events as detailed as observed by a detector. The output produced of an event generator is in the form of “events” with the same behaviour and fluctuations as the real data. The detector simulation takes the output of the generator as an input and allows a precise prediction and verification of the entire experimental setup. The comparison of real and Monte Carlo world is presented in Fig. 4.1.

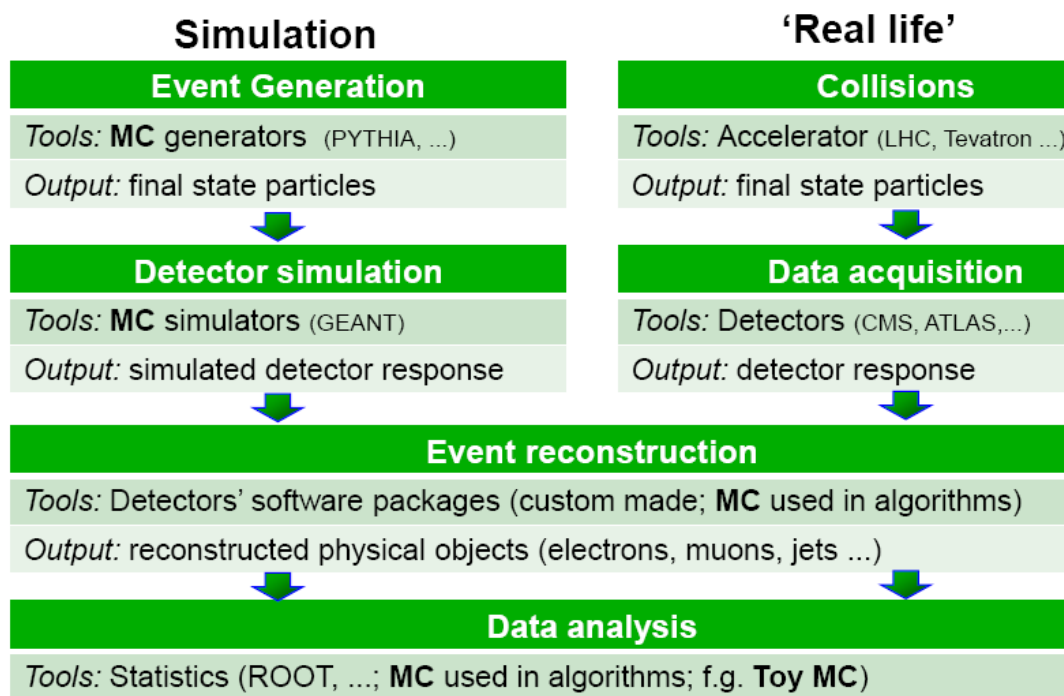


Figure 4.1: The comparison between Monte Carlo (MC) simulations generated by event generators and the real data produced by the collisions of observed in the detectors.

There are a variety of MC event generators which are commonly used in high energy physics. In this thesis, the three leading order (LO) generators : PYTHIA, MADGRAPH5 and HERWIG as well as the next-to-leading order (NLO) generator POWHEG are used. These generators are described one by one in the following sections.

4.1.1 PYTHIA

PYTHIA is the most widely used program to generate the collisions at high energies for p-p, e-e and e-p colliders. It contains theoretical models for a number of physics aspects which includes hard and soft processes, parton distribution functions, initial-state and final-state parton showers, multi-parton interactions, fragmentation and decay. It has a feature to interface with the external programs. It uses the Lund string hadronization model [69] to describe the hadronization process. PYTHIA was originally coded in FORTRAN language under the version 6 i.e. PYTHIA6 [70]. In 2004, it was rewritten in C++ and was released as PYTHIA8 [71] in 2007. The two versions differ in the description of multi-parton interactions. Both the versions use LO calculations to derive the colored partons from the hard interaction which hadronize into colorless objects like hadrons. For the studies in this thesis, PYTHIA6 with tune Z2* [72] and PYTHIA8 with tunes CUETS1 and CUETM1 [73] have been used.

4.1.2 MADGRAPH5

MADGRAPH5 [74] generates matrix elements for high energy physics processes, such as decays and $2 \rightarrow n$ scattering processes. The event information of the particles involved in the hard process such as particle ID, momenta, spin etc. is stored in the Les Houches format [75] which can be interfaced to other generators. In the current study, MADGRAPH5 has been interfaced to PYTHIA6 with tune Z2* to handle the rest of the generation steps which involves parton showering and hadronization. Matching algorithms make sure that no double-counting occurs between the tree-level and the parton-shower-model-generated partons. MADGRAPH5+PYTHIA6 (MG5+P6) samples are used mainly for general comparisons to data and calculating the detector resolution.

4.1.3 HERWIG

HERWIG (Hadron Emission Reactions With Interfering Gluons) [76] is a multi-purpose event generator which performs the LO calculations. It uses angular ordering for parton showers and cluster model for hadronization. The hard lepton-lepton, lepton-hadron and hadron-hadron scattering as well as soft hadron-hadron processes can be simulated using HERWIG generator. This generator can be interfaced to external matrix element generators. HERWIG was written in FORTRAN language and a version in C++ is also available as HERWIG++ [77]. We have used the HERWIG++ generator with the default tune of version 2.3 [78] to generate the samples which have been used to study the non-perturbative effects.

4.1.4 POWHEG

POWHEG (Positive Weight Hardest Emission Generator) generator performs the fixed NLO calculations merged with parton showers [79–81]. This generator used a computer framework known as POWHEG BOX [82] to implement NLO calculations in shower MC programs. It can be interfaced with all modern shower MC programs that support the Les Houches Interface format. It contains the hard matrix elements for NLO dijet production. POWHEG has been interfaced to PYTHIA8 with tunes CUETS1 and CUETM1 to include the parton shower and hadronization,

4.2 Detector Simulation

The particles generated by Monte Carlo event generators are passed through a computer program known as the detector simulation. It defines the detector system including its geometry, material and electronics properties. The detector simulation describes the nature of the interactions of the particles with the material of the detector. While propagating through the detector material, these particles are allowed to decay according to their known branching fractions and decay kinematics. The

particles can interact with the detector material through several physical processes, including electron bremsstrahlung, energy loss by ionization, multiple scattering, hadron showering etc., which are simulated or parametrized in the corresponding parts of the detector.

In CMS, the detector response is simulated by two approaches [50] : Full Simulation and Fast Simulation. Full Simulation is based on a C++ simulation toolkit GEANT4 (GEometry ANd Tracking) [83]. It is a successor of a FORTRAN based GEANT3 and handles the interactions of particles with matter over a wide range of energy. In GEANT4, the uniform and non-uniform electromagnetic, magnetic and electric fields can be specified. The equation of motion of the particle in the field gives the track of the particle. A physical interaction of a track in the sensitive region of a detector is called a hit. The secondary particles produced are stored in a stack with the information of their kinematic properties as well as the vertex position where the interaction has occurred. A large number of Monte Carlo events may have to be produced for a feasible physics analysis. The complete detector simulation of CMS using GEANT4 is rather time consuming. So a Fast Simulation framework [84] has been developed in the general software framework of the CMS for the fast simulation of the detector response. In Fast Simulation, detector effects are parametrized instead of simulating these from first principles as done in Full Simulation. In Fast Simulation package, the events are produced at much faster rates as compared to the Full Simulation package, while maintaining almost the same level of accuracy for physics studies. The format of the Fast Simulation data output is fully compatible with the standard Full Simulation one.

After simulating the detector response, it is then transformed into a digital signal with the help of electronics and this step is called digitization. The simulated output of the detector response needs to be as close as possible to the real data coming from the CMS detector. After this, the event reconstruction algorithms are applied to both simulated and real events.

4.3 Event Reconstruction

The aim of the event reconstruction is to identify the particles passing through the detector by interpreting the electrical signals produced in digitization. These particles are produced either directly from the interaction point of pp collisions or from the hadronization process. In event reconstruction, analysis-level objects are created by combining recorded signals from the tracker, calorimeters and muon detectors. Initially the reconstructed hits are collected which are combined to form tracks and calorimetric towers. Then higher level objects such as electrons, muons, photons and jets are reconstructed by combining the tracks and energy deposits. This thesis presents the study of jets which are collimated sprays of hadrons and other particles produced by the hadronization of a quark or gluon. The detailed description of jets is given in Sec. 2.4. The jet algorithms, discussed in Sec. 2.4.1, are used for clustering of stable partons, particles or reconstructed particles. The jets are formed at different levels : parton level, particle level and detector or reconstructed level, as illustrated in Fig. 4.2. In the CMS detector, jets are the localized deposits of energy in the calorimeter cells along with the large number of tracks in the direction of the deposited energy. Depending on the type of input to the jet algorithm, jets can be categorized into different types :

Generator Jets - The stable particles generated by the Monte Carlo event generators are clustered into generator jets (GenJets). At this particle level, the passage through the detector simulation has not been carried out. The objects at this level are photons, charged and neutral hadrons. Since the energy of GenJets is independent of the detector response, these are considered as reference objects for estimating the jet energy corrections, discussed in Sec. 4.3.2.

Calorimetric Jets - The Calometric jets (CaloJets) are reconstructed by taking the energy clusters deposited in the ECAL and HCAL calorimeter towers as inputs. One calorimetric tower consists of one HCAL cell surrounded by an array of

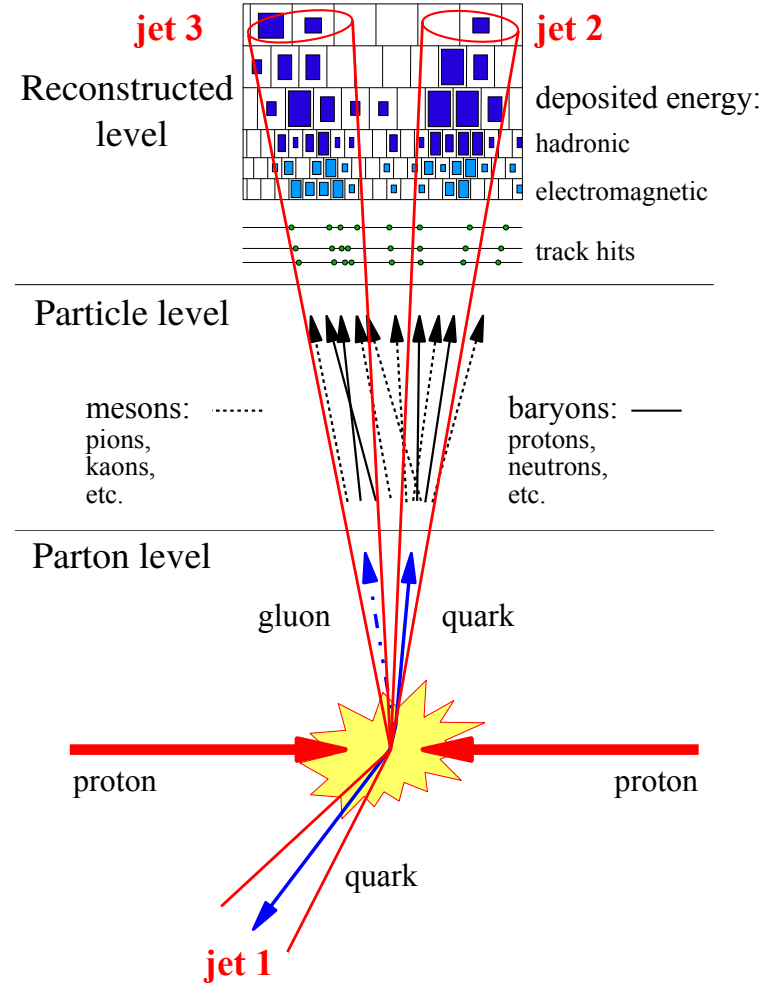


Figure 4.2: In a proton-proton collision, the hard scattered quarks and gluons fragment and hadronize to produce the showers of partons, hadrons and detector measurements which are clustered into parton jets, particle jets and reconstructed jets, respectively. Taken from [85].

5×5 ECAL cells. The tower's four-momenta are computed by taking the direction from the interaction point to the tower center. All towers with a transverse energy measurement above 300 MeV are considered in the clustering process. CaloJets are relatively simple objects because only calorimeter information is deployed, but they are strongly affected by the non-linearity of the calorimeter response. Since the readout of calorimeter measurements is fast, CaloJets are commonly used by the trigger system.

Particle Flow Jets - The clustering of particle flow candidates give detector level jets called Particle Flow jets (PFJets). The four-momenta of the particles is taken as the input. The use of the tracker system and high granularity of the ECAL gives better energy resolution calculated using the independent measurements of charged hadrons and photons clustered to form a jet. Hence PFJets perform better than CaloJets and are the standard jets used at CMS.

This thesis presents the study of the jets formed by clustering particle flow candidates using the anti- k_t algorithm with a jet size parameter of $R = 0.7$ and particle flow candidates. In CMS, all the particles are identified and reconstructed with a Particle Flow (PF) algorithm, discussed in details in next section.

4.3.1 Particle Flow Algorithm

In the CMS, the identification and reconstruction of the particles is performed using the event reconstruction technique called Particle Flow (PF) algorithm [86,87]. The PF event reconstruction algorithm basically converts the detector signals back to physical objects by using PF event reconstruction algorithm which is illustrated in Fig. 4.3. The PF algorithm combines the information from the individual sub-detectors. The additional identification of the tracks, using the Combinatorial Track Finder (CTF) algorithm [88], enhances the reconstruction performance. These tracks are used to identify the primary vertices in an event. The transverse momenta of the final state stable particles or energies of the calorimeter towers are taken as the inputs to the PF algorithm. The PF algorithm first collects the reconstructed hits in each sub-detector independently and creates a list of reconstructed elements (referred as blocks) which consists of charged tracks in tracker, energy clusters in calorimeters and muon tracks in muon system. Then a link algorithm connects topologically compatible blocks producing PF objects. The PF objects consists of all stable particles : electrons, muons, photons, charged and neutral hadrons. The

energy of the the electrons is determined from the track momentum at the main interaction vertex along with the corresponding ECAL energy deposits and the energy sum of all bremsstrahlung photons associated with the tracks. The curvature of the

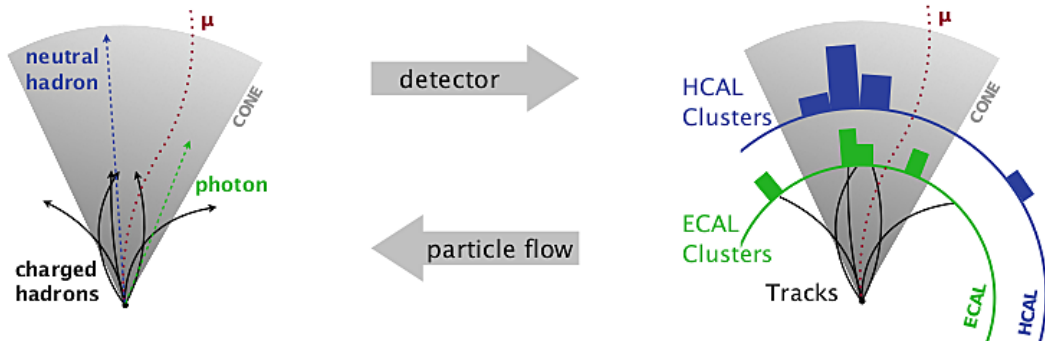


Figure 4.3: The Particle Flow (PF) algorithm is used by the CMS to identify and reconstruct the particles. The PF converts the sub-detector measurements back to physical particle objects. Taken from [15].

tracks in tracker and muon chamber is used to estimate the energy of muons. The energy of photons is obtained directly from the ECAL measurement, corrected for zero-suppression effects¹⁵. The energy of charged hadrons is calculated by combining the track momentum and corresponding energy clusters in ECAL and HCAL, corrected for zero-suppression effects as well as calibrated for the nonlinear response of the calorimeters. The energy of neutral hadrons is obtained from the corresponding calibrated ECAL and HCAL energies only. Along with the reconstruction of the PF objects, missing transverse energy (E_T^{miss}) is also determined using PF algorithm. E_T^{miss} is defined as the negative vector sum of transverse momenta (p_T) of all the isolated stable particles reconstructed in an event i.e. $E_T^{\text{miss}} = -\sum_i \vec{p}_{T,i}$. To avoid any kind of double-counting of energy, blocks of all PF reconstructed particle objects are removed and the energy of the calorimeter clusters is recalculated. Finally,

¹⁵To suppress noise in the calorimeters, only cells with energies above a given threshold are considered and this procedure is known as zero-suppression.

the collection of PF objects is used to reconstruct the jets by using jet clustering algorithms.

4.3.2 Jet Energy Corrections

The measured energy of jets cannot be directly translated to the energy at true particle or parton level. This is because of the nonlinear and nonuniform response of the calorimeters, effects of pileup and small residual effects in the data remaining after the corrections based on Monte Carlo simulations. Hence the jet energy corrections (JEC) [89, 90] are used to correct the measured jet energy and relate it to the corresponding true particle jet energy. To correct the energy of jets, the CMS follows a factorized approach, as presented in Fig. 4.4, where JEC are applied in a sequential manner with fixed order, i.e. the output of one step serves as the input for the next one. Each level of correction takes care of a different effect and is independent of each other. At each step, the jet four-momenta is scaled with a correction factor which depends on jet p_T , η , flavor etc.

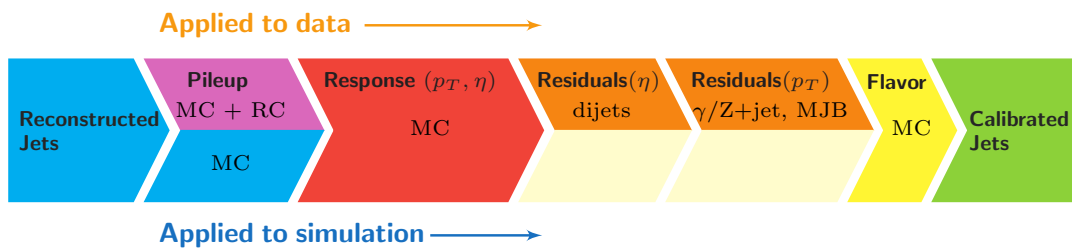


Figure 4.4: A schematic diagram of the factorized jet energy corrections (JEC) applied to data (upper half) and simulation (lower half). The reconstructed jets are corrected for pileup effects, non-uniform p_T and η response and residual differences between data and Monte Carlo simulations along with optional flavor corrections. All corrections marked with MC are derived from simulation studies, RC stands for random cone, and MJB refers to the analysis of multijet events. Taken from [90].

The corrected jet transverse momentum p_T^{corr} is obtained by applying all correction factors subsequently on raw or uncorrected jet transverse momentum p_T^{raw}

as below :

$$p_T^{\text{corr}} = c_{\text{res}}(\eta, p_T'') \cdot c_{\text{mc}}(\eta, p_T') \cdot c_{\text{pileup}}(\eta, \rho, A_j, p_T^{\text{raw}}) \cdot p_T^{\text{raw}} \quad (4.1)$$

where p_T' is the transverse momentum obtained after applying the pileup correction factor c_{pileup} on p_T^{raw} , p_T'' is the transverse momentum got after applying the additional correction factor c_{mc} because of relative and absolute effects derived from MC. Finally, a correction factor c_{res} is applied for residual effects derived from data. The corrections applied at each step are discussed below :

Pileup Corrections - The additional proton-proton collisions occur within the same bunch-crossing along with the main hard interaction and give rise to pileup events. The particles produced from the pileup events got clustered into the jets coming from the hard interaction and increase the jet energy. This extra energy needs to be subtracted from the reconstructed jet energy. This is done by applying the pileup corrections to raw jet p_T^{raw} . The pileup corrections are determined by simulating a sample of QCD dijet events with and without pileup effects. The pileup correction factor, c_{pileup} is calculated from jet area method using the pileup density ρ in the event and the jet area A_j . c_{pileup} is parametrized as a function of ρ , A_j , jet p_T and η . There are corrections for residual differences between data and detector simulation which are determined using the random cone (RC) method in zero-bias events. Hence the different pileup corrections are applied to data and MC simulations.

MC Corrections - The next correction applied to the pileup corrected jets is based on MC simulated QCD events. Due to the inefficiencies introduced by the detector simulation, the reconstructed jet p_T is not the same as that of the generated one. This difference is corrected with the factor, c_{mc} which is derived by comparing the measured jet p_T to the particle level jet p_T . The corrections are determined as a function of jet p_T and η which make the detector response uniform over these two

variables.

Residual Data Corrections - The jets corrected with above mentioned corrections are further corrected for remaining small differences between data and M simulations. This correction is only applied to data. The correction factor c_{res} is derived using data-driven methods. The relative residual corrections are evaluated using dijet events in which a probe jet is calibrated using a tag jet. The last correction applied is the absolute residual correction in which the precisely reconstructed Z bosons balanced to a jet are used to calibrate the jet energy.

Flavor Corrections - These corrections correct the jets for flavor dependence (b , τ etc.) and are optional. These are extracted using $Z+\text{jet}$ and photon+jets simulated events. The flavor corrections have not been applied for 8 TeV CMS data.

The process of correction of jets by using JEC introduces uncertainties in the final corrected jet energy which are discussed in Sec. 5.6.2. After correcting the jets, the multijet event cross-sections are measured which are discussed in the following chapter.

Chapter 5

Measurement of the Differential Inclusive Multijet Cross-sections and their Ratio

In a proton-proton collision, the inclusive jet cross-section studied as a function of jet properties, provides essential information about the parton distribution functions of proton and the strong coupling constant. This chapter describes the measurement of inclusive differential jet event cross-sections and the cross-section ratio in details which includes event and jet selections, trigger studies, spectrum construction, corrections applied and calculation of experimental uncertainties.

The inclusive differential jet event cross-sections are studied as a function of the average transverse momentum, $H_{\text{T},2}/2 = \frac{1}{2}(p_{\text{T},1} + p_{\text{T},2})$, where $p_{\text{T},1}$ and $p_{\text{T},2}$ denote the transverse momenta of the two leading jets, and are defined by :

$$\frac{d\sigma}{d(H_{\text{T},2}/2)} = \frac{1}{\epsilon \mathcal{L}_{\text{int,eff}}} \frac{N_{\text{event}}}{\Delta(H_{\text{T},2}/2)} \quad (5.1)$$

where N_{event} is the number of inclusive n-jet events counted in an $H_{\text{T},2}/2$ bin, ϵ is the product of the trigger and jet selection efficiencies, which are greater than 99%,

$\mathcal{L}_{\text{int,eff}}$ is the effective integrated luminosity, and $\Delta(H_{\text{T},2}/2)$ are the bin widths. The measurements are reported in units of (pb/GeV). The inclusive n-jet event samples include the events with number of jets $\geq n$, where $n = 2$ and 3 in the current study.

The cross-section ratio R_{32} , defined in Eq. 5.2 is obtained by dividing the differential cross-sections of inclusive 3-jet events to that of inclusive 2-jet one, for each bin in $H_{\text{T},2}/2$.

$$R_{32} = \frac{\frac{d\sigma_{3\text{-jet}}}{d(H_{\text{T},2}/2)}}{\frac{d\sigma_{2\text{-jet}}}{d(H_{\text{T},2}/2)}} \quad (5.2)$$

For inclusive 2-jet events ($n_j \geq 2$) sufficient data are available up to $H_{\text{T},2}/2 = 2000$ GeV, while for inclusive 3-jet events ($n_j \geq 3$) and the ratio R_{32} , the accessible range in $H_{\text{T},2}/2$ is limited to $H_{\text{T},2}/2 = 1680$ GeV.

5.1 Data Samples

This measurement uses the data which was collected at the center-of-mass energy of 8 TeV by CMS experiment in the 2012 run period of the LHC. The 2012 data is taken in four periods A, B, C, D and the data sets are divided into samples according to the run period. Further each sample is grouped into subsets based on the trigger decision. For run B-D, the `JetMon` stream data sets contain prescaled low trigger threshold paths (HLTPFJet40, 80, 140, 200 and 260) while the `JetHT` stream data sets contain unprescaled high threshold trigger paths (HLT PFJet320 and 400). For run A, the `Jet` stream contains all the above mentioned trigger paths. The data to be used in physics analysis must satisfy a certain criteria according to which it should fulfill the validation requirements of data quality monitoring procedure. CMS uses JSON (Java Script Object Notation) format files to store the range of good lumi

sections within a run. In the current analysis, the applied certification file¹⁶ is based on the final event reconstruction of the 2012 CMS data sets. The data sets used in the current study are mentioned in the Table 5.1 along with the luminosity of each data set which increases with period. Full 2012 data sample corresponds to an integrated luminosity of 19.71 fb^{-1} .

Table 5.1: Run range and luminosity of the proton-proton collisions data collected at the center-of-mass energy of 8 TeV by CMS experiment in the year of 2012 in four different run periods A, B, C and D.

Run	Run range	Data set	Luminosity fb^{-1}
A	190456-193621	/Jet/Run2012A-22Jan2013-v1/AOD	0.88
B	193834-196531	/Jet[Mon,HT]/Run2012B-22Jan2013-v1/AOD	4.41
C	198022-203742	/Jet[Mon,HT]/Run2012C-22Jan2013-v1/AOD	7.06
D	203777-208686	/Jet[Mon,HT]/Run2012D-22Jan2013-v1/AOD	7.37

5.1.1 Monte Carlo Samples

To have a comparison of data results with the simulated events, the MADGRAPH5 Monte-Carlo (MC) event generator has been used. It has been interfaced to PYTHIA6 by the LHE event record, to generate the rest of the higher-order effects using the Parton Showering (PS) model, with tune Z2* to model the underlying event. The MC samples are processed through the complete CMS detector simulation to allow studies of the detector response and compare to measured data on detector level.

The cross-section measured as a function of the transverse momentum p_T or the scalar sum of the transverse momentum of all jets H_T falls steeply with the increasing p_T . So in the reasonable time, it is not possible to generate a large number of high p_T events. Hence, the events are generated in the different phase-space region binned in H_T or the leading jet p_T . Later on, the different phase-space regions are added together in the data analyses by taking into account the cross-section of the

¹⁶Cert_190456-208686_8TeV_22Jan2013ReReco_Collisions12_JSON

different phase-space regions. The official CMS MADGRAPH5+PYTHIA6 (MG5+P6) MC samples used in this analysis are generated as slices in the H_T phase-space are tabulated in Table 5.2 along with their cross-sections and number of events generated.

Table 5.2: The official Monte Carlo samples are produced in phase space slices in H_T with the generator MADGRAPH5 and interfaced to PYTHIA6 for the parton shower and motorization of the events. The cross-section and number of events generated are mentioned for each sample.

Generator	Sample	Events	Cross-section pb
MADGRAPH5 + PYTHIA6	/QCD_HT-100To250_TuneZ2star_8TeV-madgraph-pythia6/ Summer12_DR53X-PU_S10_START53_V7A-v1/AODSIM	50129518	1.036×10^7
	/QCD_HT-250To500_TuneZ2star_8TeV-madgraph-pythia6/ Summer12_DR53X-PU_S10_START53_V7A-v1/AODSIM	27062078	2.760×10^5
	/QCD_HT-500To1000_TuneZ2star_8TeV-madgraph-pythia6/ Summer12_DR53X-PU_S10_START53_V7A-v1/AODSIM	30599292	8.426×10^3
	/QCD_HT-1000ToInf_TuneZ2star_8TeV-madgraph-pythia6/ Summer12_DR53X-PU_S10_START53_V7A-v1/AODSIM	13843863	2.040×10^2

5.2 Event Selection

The events are selected according to several quality criteria which ensures the high purity and high selection efficiency of the sample to be studied. This event selection also reduces beam induced background, detector-level noise and jets arising from fake calorimeter energy deposits.

5.2.1 Trigger Selection

CMS implements a two-level trigger system to reduce the amount of recorded events to a sustainable rate. In this analysis the jets are the final objects to study. So single jet trigger paths with varying thresholds are used to select events in data. It consists of one L1 trigger seed and multiple HLT filters. The L1 jet trigger uses transverse energy sums computed using both HCAL and ECAL in the central region ($|\eta| < 3.0$) or HF in the forward region ($|\eta| > 3.0$). The single jet triggers (HLT_PFJetX), same

as the ones used for other CMS 8 TeV measurements [23, 91], are used in the current study and are tabulated in Table 5.3. A single jet trigger selects an event in which at least one jet has the transverse momentum above the threshold. HLT_PFJetX implies that there is at-least one jet in the event, whose $p_T > X$ (GeV). The L1 trigger has a lower threshold to ensure full efficiency versus p_T of the HLT trigger. The p_T spectrum is steeply falling and hence the rates for low- p_T jets are very high. So it is not feasible to use a single unprescaled trigger for the selection of all required events. To collect sufficient data in the lower part of the p_T spectrum, different five prescaled low- p_T trigger paths, each with different prescale value, are used. Also, one unprescaled trigger i.e. HLT_Jet320 is used in the high p_T region, in which the rate is sufficiently small to collect and store all events. During the reconstruction of the spectrum, the prescales have been taken into the account.

Table 5.3: The single jet HLT trigger paths used in the analysis are listed here. The column $H_{T,2}/2, 99\%$ indicates the value of $H_{T,2}/2$ at which each trigger exhibits an efficiency larger than 99%. The last column gives the effective luminosity seen by each trigger which divided by the total integrated luminosity of 19.71 fb^{-1} , gives the effective prescale applied on a trigger over the whole run period.

Trigger Path	L1 threshold GeV	HLT threshold GeV	$H_{T,2}/2, 99\%$ GeV	Eff. Lumi fb^{-1}
HLT_PFJet80	36	80	120.0	0.0021
HLT_PFJet140	68	140	187.5	0.056
HLT_PFJet200	92	200	262.5	0.26
HLT_PFJet260	128	260	345.0	1.06
HLT_PFJet320	128	320	405.0	19.71

The efficiency of each trigger path as a function of $H_{T,2}/2$ is described by the turn-on curves with a rising part where the trigger is partly inefficient, until a plateau region where the trigger is fully efficient. Hence it is important to determine the threshold above which a trigger becomes fully efficient. The threshold is the value at which the trigger efficiency exceeds 99%. The trigger efficiency for HLT_PFJetY is given by Eq. 5.3 where HLT_PFJetX is the reference trigger and is assumed to be fully efficient in the considered phase space region. The value of X is chosen

previous to that of Y in p_T ordering from the trigger list so that the higher trigger condition can be emulated from the lower trigger path.

$$\epsilon_{\text{HLT_PFJetY}} = \frac{H_{T,2}/2 \left(\text{HLT_PFJetX} + (\text{L1Object}_p > Z) + (\text{HLTOBJECT}_p > Y) \right)}{H_{T,2}/2(\text{HLT_PFJetX})} \quad (5.3)$$

where Y is the p_T threshold of HLT_PFJetY and Z is the L1 seed value corresponding to the trigger path HLT_PFJetY. The denominator represents the number of events for which the reference trigger path HLT_PFJetX has been fired. The numerator is the number of events for which HLT_PFJetX has been fired along the p_T of L1Object \geq Z and the p_T of HLTOBJECT \geq Y. For example, to obtain turn-on curve for HLT_PFJet260, HLT_PFJet200 is the reference HLT path. The p_T cut on L1Object is 128 GeV and p_T cut on HLTOBJECT is 260 GeV. The threshold point at which the trigger efficiency is larger than 99% is determined by fitting the turn-on distribution with a sigmoid function described in Eq. 5.4. The trigger turn-on curves as a function of $H_{T,2}/2$ can be seen in Fig. 5.1 which are described by a sigmoid function (blue line). The error bars give the uncertainty on the efficiency which is calculated using Clopper-Pearson confidence intervals [92].

$$f_{fit}(x) = \frac{1}{2} \left(1 + \text{erf} \left(\frac{x - \mu}{\sqrt{2}\sigma} \right) \right) \quad (5.4)$$

5.2.2 Primary Vertex Selection

The reconstructed tracks, number of strip and pixel hits and the normalized track χ^2 , identify the primary vertex (PV). The tracks are clustered according to the z-coordinate of their point of closest approach to the beam axis. A selection criteria for primary vertex should be followed which helps to identify and reject the beam

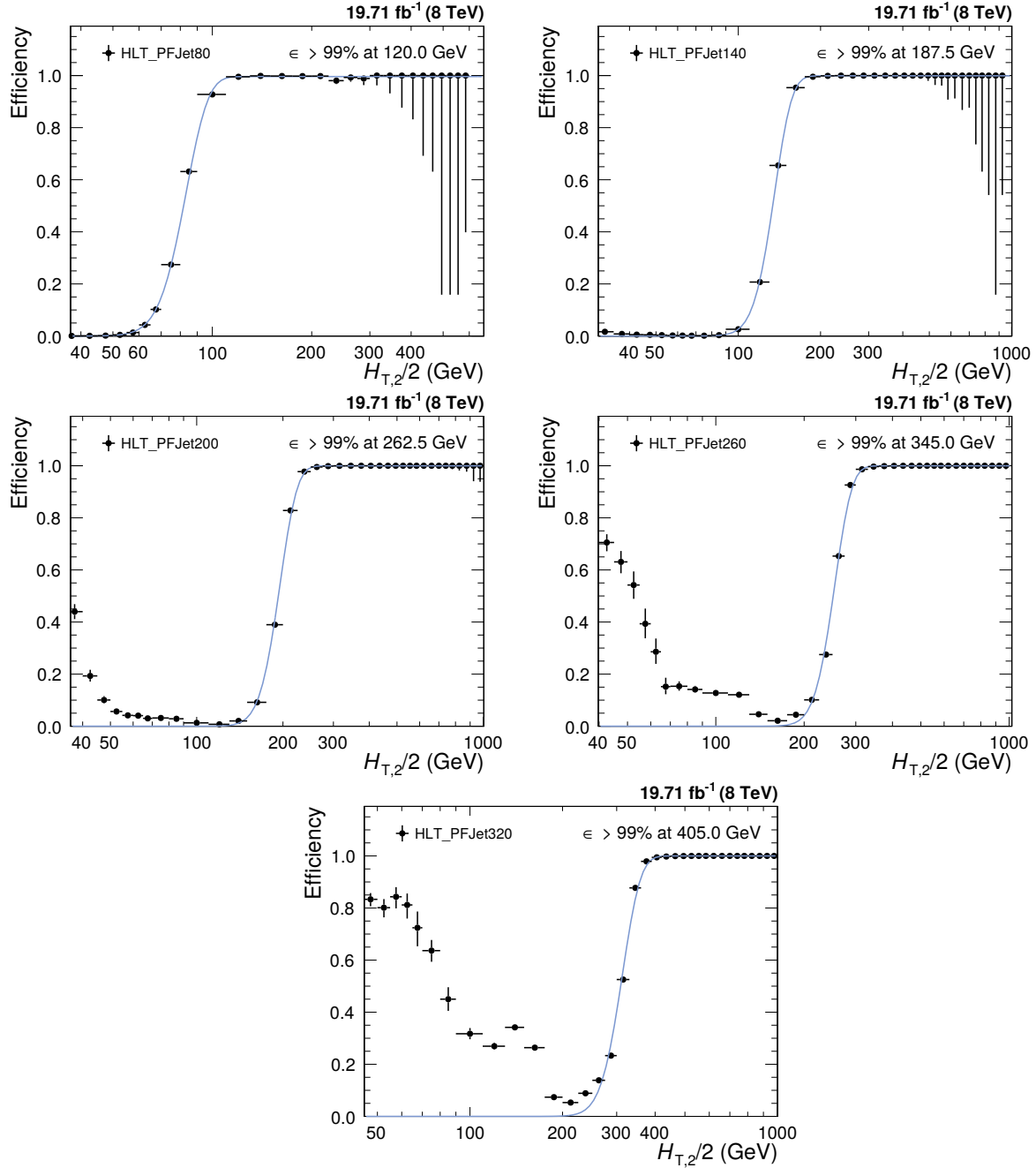


Figure 5.1: Trigger efficiencies turn-on curves for the single jet HLT trigger paths are fitted with a sigmoid function (blue line) to obtain the 99% efficiency threshold. The error bars give the uncertainty on the efficiency which is calculated using Clopper-Pearson confidence intervals [92].

background events. At-least one good primary vertex reconstructed from at least four tracks within a distance of $|z(PV)| < 24$ cm to the nominal interaction point in a collision, is required in each event. The radial distance in x-y plane, $\rho(PV)$ should be not be greater than 2 cm. The number of degrees of freedom in fitting for the position of each vertex using its associated tracks should be at-least four in number.

5.2.3 Missing Transverse Energy

In an ideal detector where all particles could be identified and perfectly measured, the transverse momentum of all particles would sum up to zero. But the neutral weakly interacting particles, such as neutrinos, escape from typical collider detectors and do not produce any direct response in the detector elements. The imbalance of total momentum of all visible particles can give the hints of the presence of such particles. The vector momentum imbalance in the plane perpendicular to the beam direction is known as missing transverse momentum or energy (E_T^{miss}). It is one of the most important observables for discriminating leptonic decays of W bosons and top quarks from background events which do not contain neutrinos, such as multijet and Drell–Yan events or searches for physics beyond the Standard Model.

The ratio of missing transverse energy to the total transverse energy $E_T^{\text{miss}}/\sum E_T$, shown in Fig. 5.2 for $n_j \geq 2$ (left) and $n_j \geq 3$ events (right), shows a discrepancy between data (black solid circles) and simulated MC (blue histogram), at the tail part of the distribution. This is because of a finite contribution from $Z(\rightarrow \nu\bar{\nu}) + \text{jet}$ events which gives rise to non-zero E_T in the events in data. Such events are absent in QCD simulated events in MC. Hence $E_T^{\text{miss}}/\sum E_T$ is required to be less than 0.3 to reject events with high E_T^{miss} .

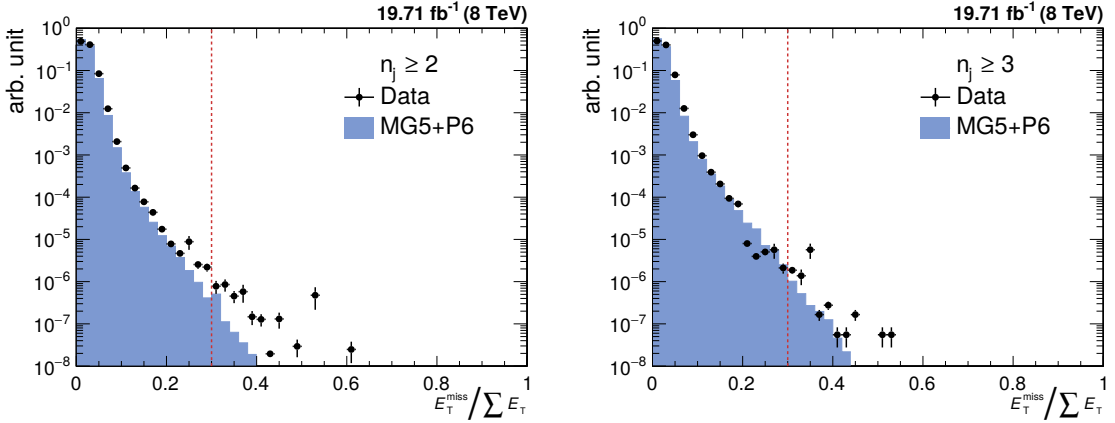


Figure 5.2: Missing transverse energy fraction of the total transverse energy per event in data (black solid circles) and simulated Monte Carlo events (blue histogram) in inclusive 2-jet (left) and 3-jet events (right). To remove background and noise, events with a fraction exceeding a certain threshold, here indicated with the red dashed line, are rejected.

5.2.4 Jet Identification

In order to suppress fake jets, arising from detector noise or misreconstructed particles, jet identification criteria (ID) has been applied. Instead of applying it event-wise, it is applied it on each jet. The algorithm works on reconstructed jets using information of the clustered particle candidates. The official tight jet ID [93], recommended by JETMET group [94] is used. Due to pileup and electronic noise the jet constituent fractions may vary from event to event. In order to reject the noisy jets, some jet selection criteria are optimized to select only good quality jets. The selection criteria are implemented as selection cut on jet fractions. Table 5.4 summarizes the properties of the reconstructed jets and their respective cuts. Each jet should contain at least two particles, one of which should be a charged hadron. The cut on the fraction of neutral hadrons and photons removes HCAL noise and ECAL noise, respectively. Muons that are falsely identified and clustered as jets are removed by the muon fraction criterion. Based on information of the tracker, additional selection cuts are enforced in the region $|\eta| < 2.4$. The charged electromagnetic fraction cut removes the jets clustered from misidentified electrons. Furthermore, the fraction of charged hadrons in the jet must be larger than zero and jets without any charged

hadrons are very likely to be pileup jets. The Figs. 5.3 and 5.4 show the distributions of the jet constituents observed in data (black solid circles) and simulated MC events (blue histogram) for $n_j \geq 2$ and $n_j \geq 3$, respectively.

Table 5.4: The jet ID removes noise and fake jets based on the properties of the reconstructed jets and the clustered particle candidates. All the selection cuts which are recommended by the JETMET group are applied [94].

	Property	Loose ID	Tight ID
Whole η region	neutral hadron fraction	< 0.99	< 0.90
	neutral EM fraction	< 0.99	< 0.90
	number of constituents	> 1	> 1
	muon fraction	< 0.80	< 0.80
only $ \eta < 2.4$	charged hadron fraction	> 0	> 0
	charged multiplicity	> 0	> 0
	charged EM fraction	< 0.99	< 0.90

5.2.4.1 Jet ID Efficiency

The efficiency of the jet ID as a function of $H_{T,2}/2$ is studied using a tag-and-probe technique with dijet events. The two leading jets are required to be back-to-back in the azimuthal plane such that $|\Delta\phi - \pi| < 0.3$. One of the dijets is selected randomly as a “tag” jet which is required to fulfill the tight jet ID criteria. The other jet is called “probe” jet for which it is examined, whether it also passes the tight jet ID. The ID efficiency is defined as the ratio of events where the probe jet passes the ID requirements, over the total number of dijet events. It is shown as function of $H_{T,2}/2$ in Fig. 5.5 and as expected, it is always greater than 99%. The QCD cross-section decreases as a function of $H_{T,2}/2$ and hence the number of events decrease on moving to higher $H_{T,2}/2$. Consequently the statistical fluctuations for ID efficiency are larger at higher $H_{T,2}/2$.

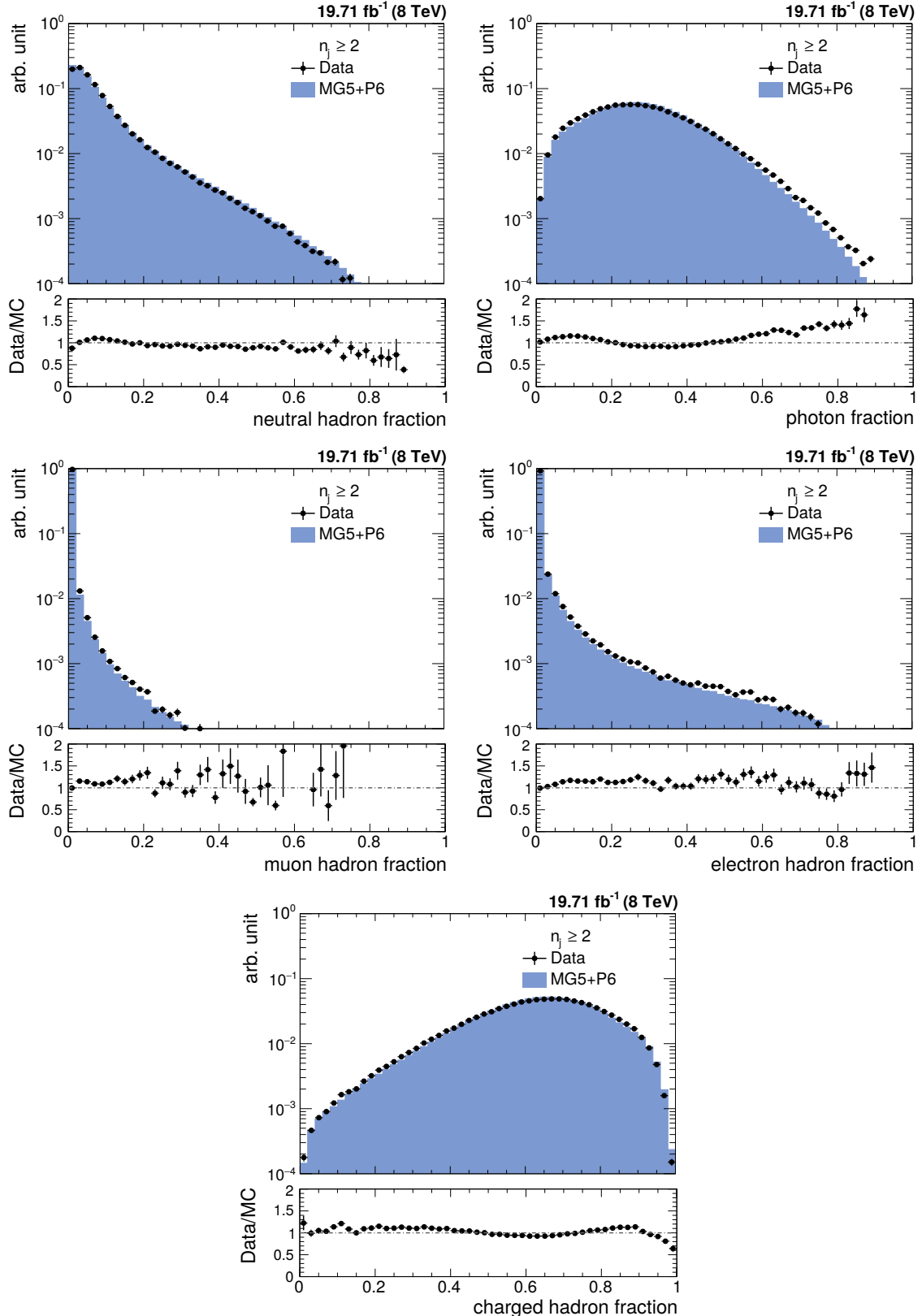


Figure 5.3: The fractions of jet constituents as observed in data (black solid circles) and simulated Monte Carlo events (blue histogram) for different types of PF candidates for inclusive 2-jet events. Data and simulations are normalized to the same number of events. The distributions are shown after the application of the jet ID.

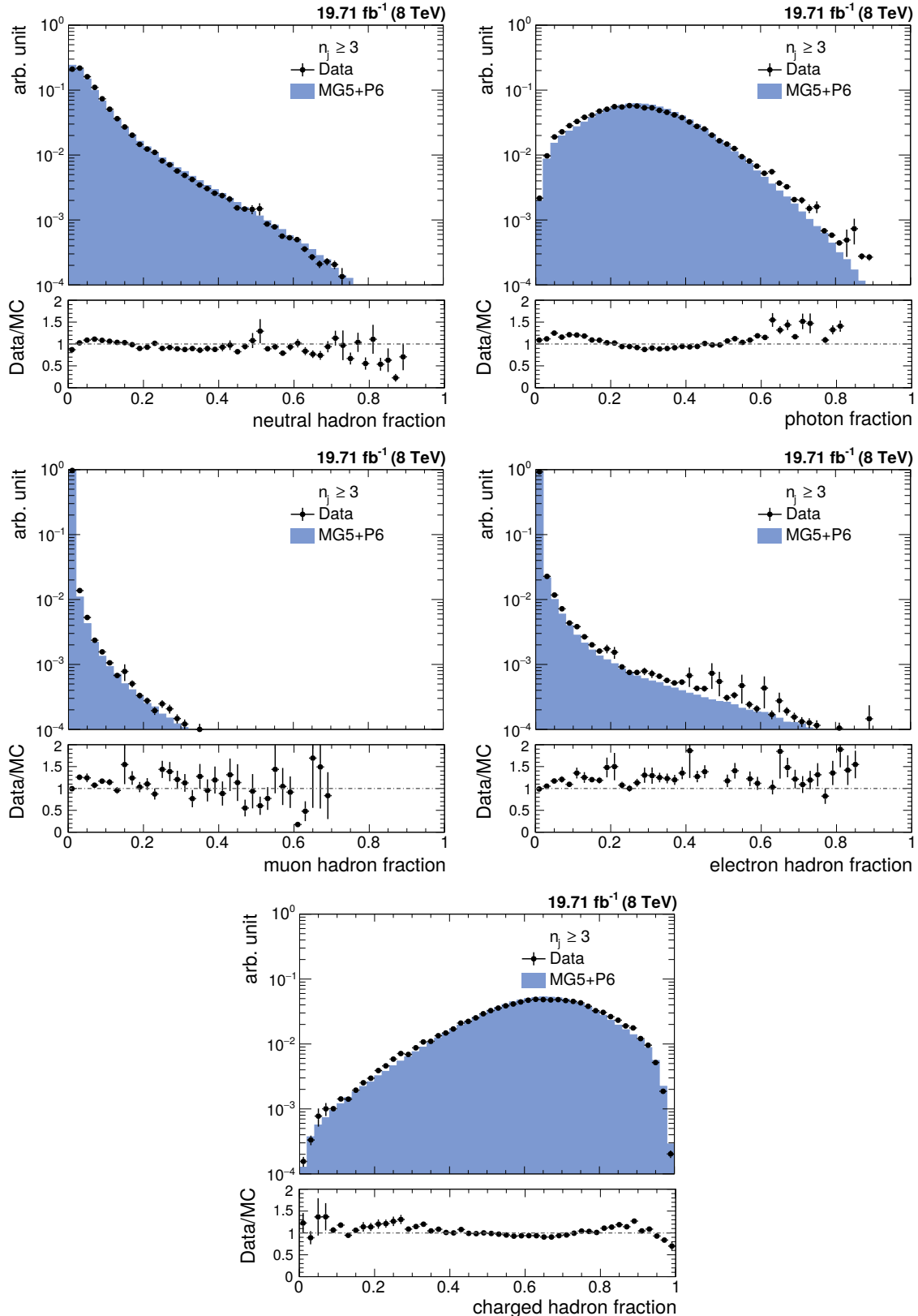


Figure 5.4: The fractions of jet constituents as observed in data (black solid circles) and simulated Monte Carlo events (blue histogram) for different types of PF candidates for inclusive 3-jet events. Data and simulations are normalized to the same number of events. The distributions are shown after the application of the jet ID.

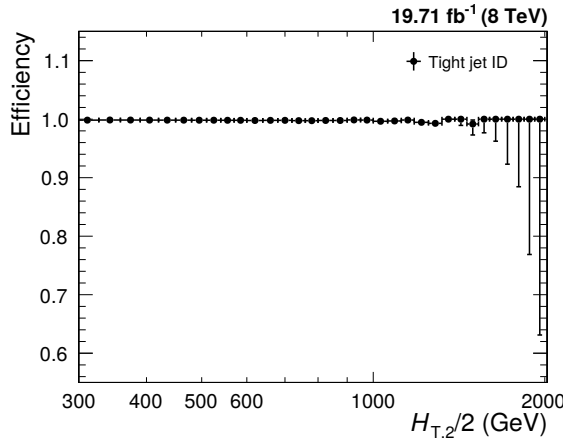


Figure 5.5: The jet ID efficiency is studied as a function of $H_{T,2}/2$ with tag-and-probe technique using dijet event topologies and it always exceeds 99%.

5.2.5 Jet Selection

The measurement of differential cross-sections and their ratio uses jets clustered from particle flow candidates using the anti- k_t jet algorithm with a size parameter, $R = 0.7$. The energy scale of the jets is corrected with the CMS recommended jet energy corrections, described in Sec. 4.3.2. These corrections are applied to jets in both data¹⁷ as well those in simulated events¹⁸. As a convention, the jets in one event are in decreasing order of p_T , with the first (leading) jet being the jet with highest p_T . The jet selection, based on phase space cuts on transverse momentum and rapidity of jets in an event, is as follows :

- All jets having $p_T > 150$ GeV and $|y| < 5.0$ are selected.
- Events with at least two jets are selected.
- The two leading jets should have $|y| < 2.5$ and further jets are counted only, if they lie within the same central rapidity range of $|y| < 2.5$.

These cuts assure high detector acceptance and exactly same selection is ap-

¹⁷Winter14_V8 jet energy corrections

¹⁸START53_V27 jet energy corrections

plied in the measurement, simulated events as well in theoretical calculations for a consistent comparison.

5.3 Comparison with Simulation

5.3.1 Pileup Reweighting

While generating the official Monte-Carlo samples, the number of pileup interactions describing the conditions expected for each data-taking period are taken care of. But the number of pileup events implemented in the simulation $N_{\text{MC}}(N_{\text{PU,truth}})$, does not match exactly with the one measured actually in data $N_{\text{data}}(N_{\text{PU,est.}})$. To match the pileup distributions in data, a reweighting factor w_{PU} , as given by Eq. 5.5 is applied to the simulated events. In Fig. 5.6 the number of reconstructed vertices are shown before (left) and after pileup reweighting (right). It is observed that before pileup reweighting there was a significant mismatch of the pileup distributions in data (black solid circles) and simulated MC events (blue histogram), which completely vanishes after reweighting.

$$w_{\text{PU}} = \frac{N_{\text{data}}(N_{\text{PU,est.}}) / \sum N_{\text{data}}}{N_{\text{MC}}(N_{\text{PU,truth}}) / \sum N_{\text{MC}}} \quad (5.5)$$

5.3.2 Comparison of Cross-sections and their Ratio

The measured data distribution of differential cross-section at detector level is compared to the predictions of Monte Carlo simulation using MADGRAPH5 generator interfaced with PYTHIA6 (MG5+P6) including the detector simulation as well as to a fixed-order theory prediction obtained using CT10-NLO PDF set. Figure 5.7 shows the comparison of differential cross-section as a function of $H_{T,2}/2$ for $n_j \geq 2$ (left) and $n_j \geq 3$ events (right), for data (black solid circles), MG5+P6 MC (red empty

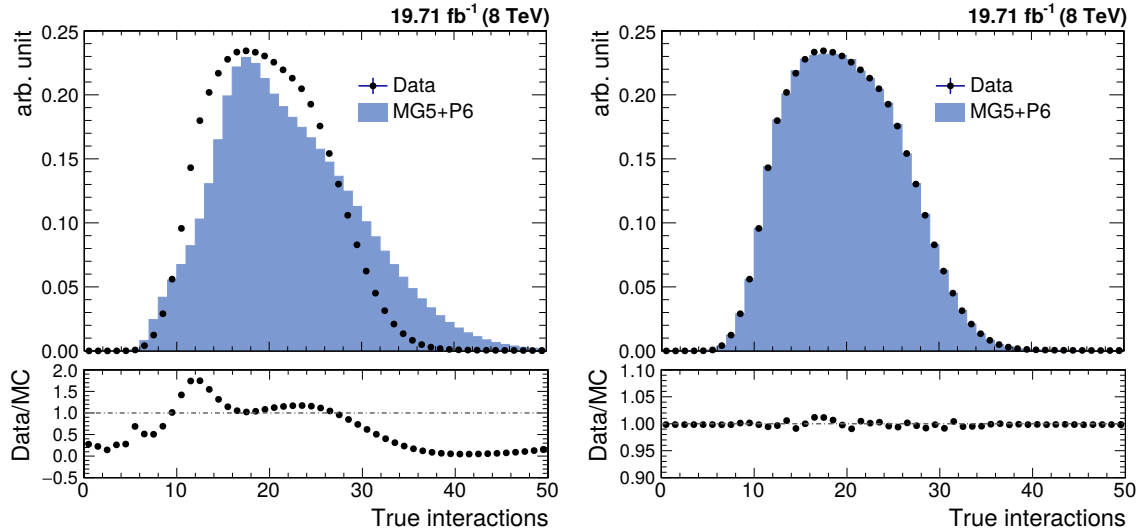


Figure 5.6: Number of reconstructed vertices in data (black solid circles) and simulated Monte Carlo events (blue histogram) before (left) and after (right) the pileup reweighting.

circles) and CT10-NLO (blue histogram). The bottom panel in each plot shows the ratio of data to the MC predictions (red line) as well as to the CT10-NLO theory predictions (blue line). The NLO predictions on parton level are not corrected for non-perturbative effects. Still the NLO predictions describe the data better as compared to the LO MC simulations which roughly describes the spectrum on detector level. The sufficient data for $n_j \geq 2$ and $n_j \geq 3$ events are available up to $H_{T,2}/2 = 2000$ GeV and 1680 GeV, respectively. Due to some kinematical constraints, the minimum cut on $H_{T,2}/2$ is 300 GeV (explained in Sec. 6.1.1). Hence the differential cross-sections are studied in the range $300 \text{ GeV} \leq H_{T,2}/2 < 2000 \text{ GeV}$ for $n_j \geq 2$ and $300 \text{ GeV} \leq H_{T,2}/2 < 1680 \text{ GeV}$ for $n_j \geq 3$ events.

The ratio of differential cross-sections, R_{32} as a function of $H_{T,2}/2$, is extracted by dividing the cross-section of selected inclusive 3-jet events to that of inclusive 2-jet events at any given bin size of $H_{T,2}/2$. In the cross-section ratios, the numerator and denominator are not independent samples. So to calculate the statistical uncertainty for the cross-section ratios at reconstructed level, the Wilson score interval method is used which takes into account the correlation between the

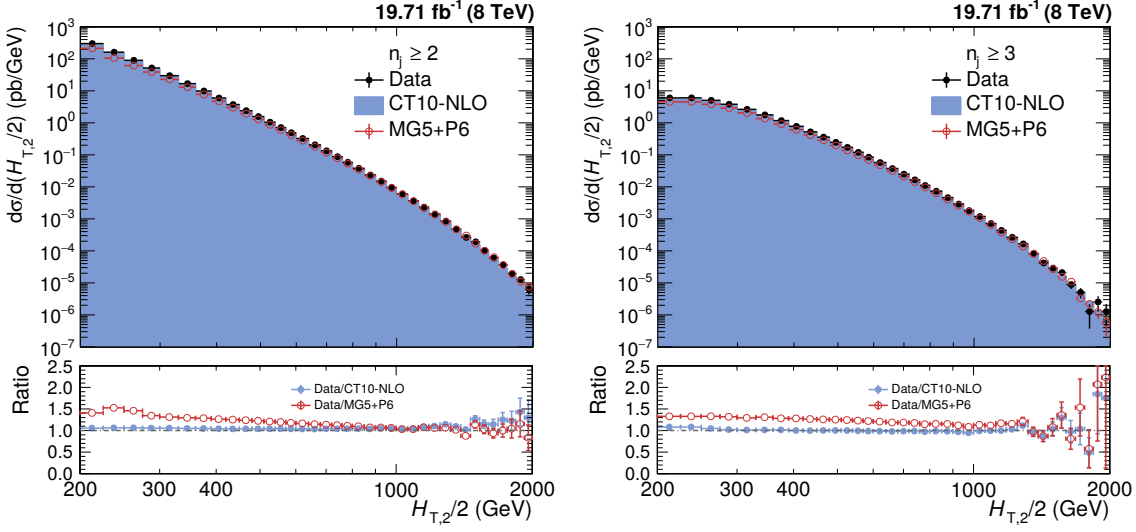


Figure 5.7: The reconstructed level differential cross-sections are compared for data (black solid circles) and LO MADGRAPH5+PYTHIA6 (MG5+P6) Monte Carlo (red empty circles) simulations with CT10-NLO theory predictions (blue histogram), as a function of $H_{T,2}/2$ for inclusive 2-jet (left) and 3-jet events (right). Ratios of data to the Monte Carlo predictions (red line) as well as to the CT10-NLO predictions (blue line) are shown in bottom panel of each plot.

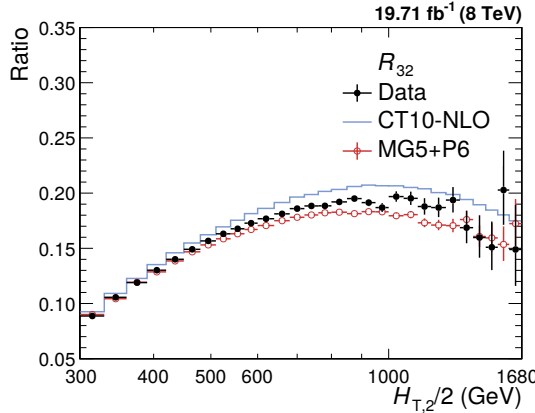


Figure 5.8: Comparison of the reconstructed level cross-section ratio R_{32} as a function of $H_{T,2}/2$, for data (black solid circles) and LO MADGRAPH5+PYTHIA6 (MG5+P6) Monte Carlo (red empty circles) with CT10-NLO theory predictions (blue line). The error bars give the asymmetrical statistical uncertainty, calculated by the Wilson score interval method which takes into the account the correlation between the numerator and denominator.

numerator and the denominator and give asymmetric errors. Figure 5.8 shows the comparison of the cross-section ratio R_{32} as a function of $H_{T,2}/2$, for data (black solid circles) and LO MADGRAPH5+PYTHIA6 (MG5+P6) Monte Carlo (red empty

circles), at reconstructed level with CT10-NLO theory predictions (blue line). Since in $n_j \geq 3$ events, the enough statistics for differential cross-section is available up to 1680 GeV of $H_{T,2}/2$ only, R_{32} is also studied in the range $300 \text{ GeV} \leq H_{T,2}/2 < 1680 \text{ GeV}$. The bin-wise inclusive 2-jet and 3-jet events differential cross-sections as well as their ratio R_{32} , calculated at detector level, along with statistical uncertainty (in %) are tabulated in Table A.1.

5.4 Jet Energy Resolution (JER)

In an ideal experiment, the value of a physical quantity would be determined exactly with an infinite precision. For e.g. whenever a particle with energy E passes an ideal calorimeter having infinite resolution, the measured energy should always be equal to E . But in real world, the measured energy of the above mentioned particle might differ from the value E . This difference of the measured quantity from its true value may be due to detector noise, uncertainties in the calibration, non-linearity of the response etc. Hence this results in the finite value of the resolution of the detector known as jet energy resolution (JER). In such case, the measured values of energy of different particles, passing through the same detector with same energy E , will be different. Such measurements are described by a Gaussian distribution which is centered around the true value of the measured quantity and its width is generally interpreted as detector resolution. Hence the importance of the detector resolution lies in the fact that it indicates how much the measured value of the observable differs from the true one i.e. how precisely a physical observable can be measured. The narrower the distribution, the higher the resolution is and hence the more efficient is the detector.

Due to finite resolution of the CMS detector, the measured transverse momentum of jets gets smeared. Since the observable in this study i.e. $H_{T,2}/2$ is the average sum of transverse momentum of leading and sub-leading jets, the resolution

of the detector has to be studied in terms of the observable. CMS detector simulation based on MG5+P6 MC event generators is used to determine the resolution as both the particle and reconstructed level information is available. The jets clustered from stable generator particles called Gen jets as well as from particle flow candidates reconstructed from the simulated detector output called Reco jets, are used. The studies of the JETMET working group at CMS has shown that the jet energy resolution in data is actually worse than in simulation [95]. So the reconstructed jet transverse momentum needs to be smeared additionally to match the resolution in data. Table 5.5 shows the scaling factors (c) which need to be applied on the transverse momentum of simulated reconstructed jets. The scaling factors depend on the absolute η of the jet. The uncertainty on these measured scaling factors ($c_{central}$) needs to be taken into account in a physics analysis. This is done by smearing the reconstructed jets with two additional sets of scaling factors, c_{up} and c_{down} , that correspond to varying the factors up and down respectively, by one sigma and evaluating the impact of these new sets.

Table 5.5: JETMET working group at CMS has shown that the jet energy resolution in data is actually worse than in simulation [95]. To match the resolution in data, the reconstructed jet transverse momentum in simulated events need to be smeared by applying the scale factors. The uncertainty on the resolution is given by an upwards and downwards variation c_{up} and c_{down} of the measured scaling factor $c_{central}$.

η	0.0 - 0.5	0.5 - 1.1	1.1 - 1.7	1.7 - 2.3	2.3 - 2.8
$c_{central}$	1.079	1.099	1.121	1.208	1.254
c_{down}	1.053	1.071	1.092	1.162	1.192
c_{up}	1.105	1.127	1.150	1.254	1.316

The reconstructed jet p_T is smeared randomly using a Gaussian width widened by the scaling factor ($c_{central}$)

$$p_T \rightarrow \text{Gauss} \left(\mu = p_T, \sigma = \sqrt{c_{central}^2 - 1} \cdot \text{JER}(p_T) \right) \quad (5.6)$$

where $\text{JER}(p_T)$ is the resolution determined as a function of jet p_T using MG5+P6 MC simulated events. After smearing transverse momentum of each reco jet, $H_{T,2}/2$ is calculated from both generator particle jets (Gen $H_{T,2}/2$) as well as the particle flow or reconstructed jets (Reco $H_{T,2}/2$). Then the response is calculated as defined in the Eq. 5.7.

$$R = \frac{\text{Reco } H_{T,2}/2}{\text{Gen } H_{T,2}/2} \quad (5.7)$$

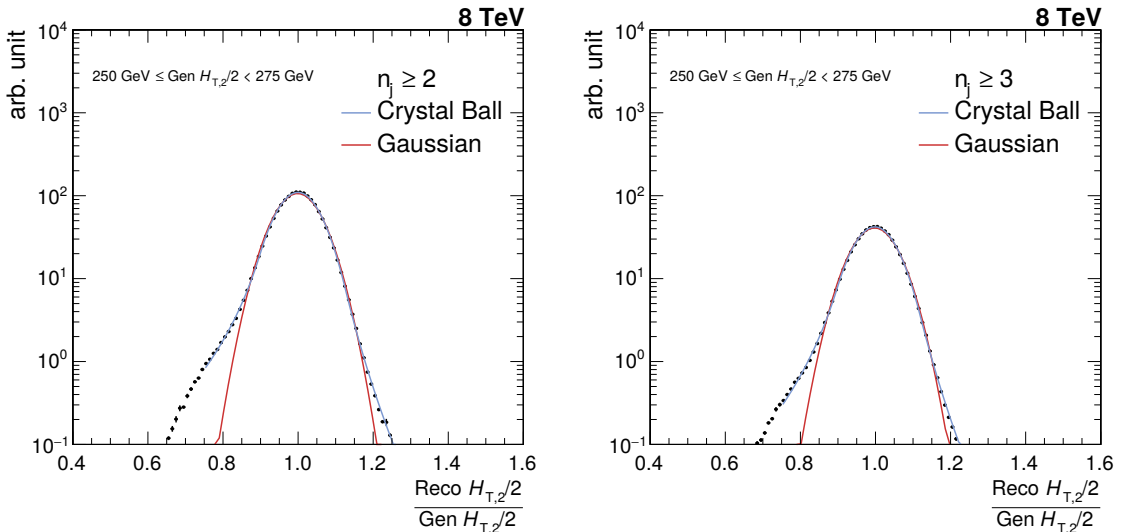


Figure 5.9: Fitting of the jet energy resolution distribution, obtained using LO MADGRAPH5+PYTHIA6 (MG5+P6) Monte Carlo simulated events, as a function of $H_{T,2}/2$ for inclusive 2-jet (left) and 3-jet events (right). The blue line shows the double-sided Crystal Ball function fit of $\frac{\text{Reco } H_{T,2}/2}{\text{Gen } H_{T,2}/2}$ in each Gen $H_{T,2}/2$ bin, overlayed by Gaussian fitting the core of the resolution (red line).

The width of the response distribution in a given Gen $H_{T,2}/2$ bin is interpreted as the resolution which in good approximation can be described by the σ of a Gaussian fit of the response distribution. A double-sided Crystal-Ball function takes into account the non-Gaussian tails of the jet response distribution. The resolution as a function of $H_{T,2}/2$ is calculated separately for both $n_j \geq 2$ and $n_j \geq 3$ events. A fit example for one Gen $H_{T,2}/2$ bin is shown in Fig. 5.9 for $n_j \geq 2$ (left) and 3-jet events (right). Here the black dots represent the jet response distribution and the

double-sided Crystal-Ball fit (blue line) is overlayed by the Gaussian fit (red line).

The resolution in each Gen $H_{T,2}/2$ bin is then plotted as a function of Gen $H_{T,2}/2$.

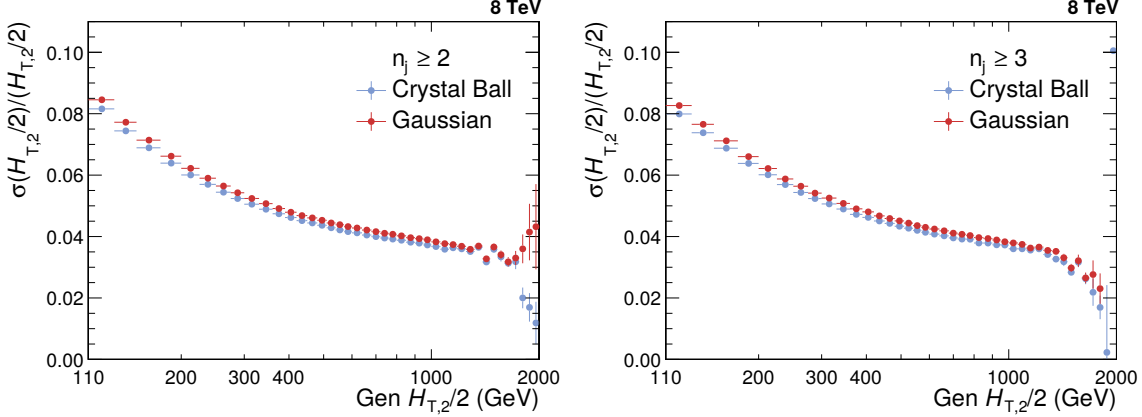


Figure 5.10: Comparison of jet energy resolution calculated using Crystal-Ball fit function (blue solid circles) and Gaussian fit function (red solid circles) for inclusive 2-jet (left) and 3-jet events (right).

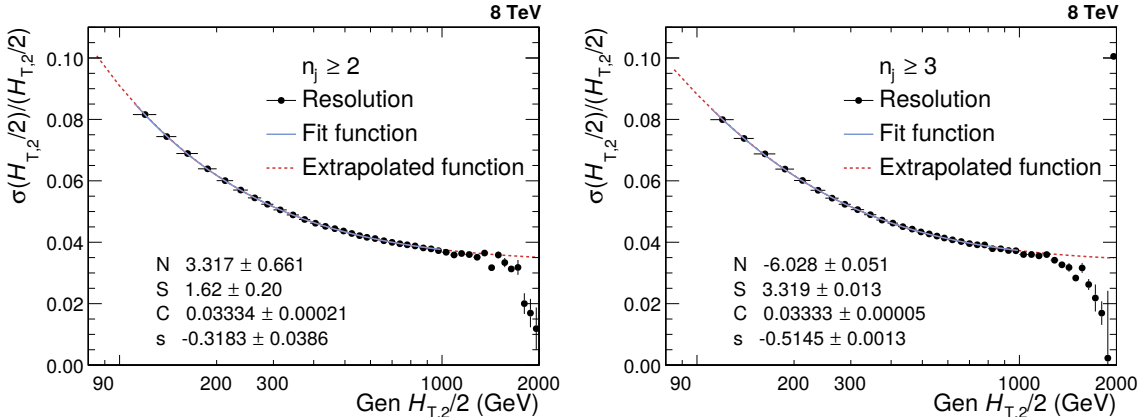


Figure 5.11: Jet energy resolution (JER) is shown as a function of Gen $H_{T,2}/2$ for inclusive 2-jet (left) and 3-jet events (right). JER (black solid circles) is fitted by using the modified NSC-formula (blue solid line) which is extrapolated to 80 GeV and up to 2000 GeV (red dashed line) to consider the migration into lower as well as higher bins.

As expected, it has been observed from Fig. 5.10 that the Crystal Ball function (blue solid circles) describes the measured distributions better as compared to Gaussian function fit (red solid circles), especially in the low- $H_{T,2}/2$ region where the non-Gaussian tails are more pronounced. Hence JER is determined using Crystal Ball function fit. Figure 5.11 shows the final relative jet energy resolution (JER)

which is described by a modified version of the NSC formula (blue solid line) [96], as mentioned in Equation 5.8. To consider the migration to lower as well higher bins and to obtain the resolution with reasonable statistics over the full range of Gen $H_{T,2}/2$, the fit function is extrapolated to 80 GeV and up to 2000 GeV which is shown by red dashed line. The fit formula used here is basically the usual NSC formula which describes the resolution in terms of noise N originating due to electronic and pileup noise and is independent of $H_{T,2}/2$; a stochastic component S due to sampling fluctuation and EM fraction fluctuation per hadrons; and a constant term C because of dead material, magnetic field and calorimeter cell to cell fluctuation. In the low $H_{T,2}/2$ region the tracking has a non-negligible influence on the resolution due to the particle flow algorithm, so the additional parameter s is introduced to obtain slightly better fits. The parameters obtained after fitting the relative resolution using the above mentioned NSC formula are tabulated in Table 5.6 for $n_j \geq 2$ and $n_j \geq 3$ events. This calculated JER is used in unfolding procedure to smear the generated truth spectrum which is used as input in getting the response matrices and is explained in details in Sec. 5.5.1. Since JER in $n_j \geq 2$ events is similar to that one in $n_j \geq 3$ events, so N , S and C fit parameters obtained for $n_j \geq 3$ events are used for unfolding R_{32} .

$$\frac{\sigma(x)}{x} = \sqrt{sgn(N) \cdot \frac{N^2}{x^2} + S^2 \cdot x^{s-1} + C^2} \quad (5.8)$$

Table 5.6: The parameters obtained by fitting the relative resolution as a function of $H_{T,2}/2$, using the modified NSC formula, for inclusive 2-jet and 3-jet events.

	N	S	C	s
Inclusive 2-jet	3.32	1.62	0.0333	-0.318
Inclusive 3-jet	-6.03	3.32	0.0333	-0.515

Since the JER is calculated using MG5+P6 Reco and Gen $H_{T,2}/2$ distributions, so it is expected that if Gen $H_{T,2}/2$ is smeared using this JER, it should match the

Reco $H_{T,2}/2$. But this extracted JER in one large rapidity bin, smears the Gen $H_{T,2}/2$ too much because Smeared Gen/Gen ratio (red line) shows a discrepancy from simulated Reco/Gen ratio (blue line), as observed in Fig. 5.12 for $n_j \geq 2$ (left) and $n_j \geq 3$ events (right). Some shortcomings in the detector simulation of the theory spectra leads to these small nonclosures. When the 30% reduced JER is used to smear Gen, then the ratio Smeared Gen/Gen (pink line) matches with simulated Reco/Gen ratio (blue line) within the statistical fluctuations. Hence an additional unfolding uncertainty is attributed by comparison to 30% reduced JER for both $n_j \geq 2$ and $n_j \geq 3$ events. Due to high statistical fluctuations at high $H_{T,2}/2$, range is presented up to 1680 GeV only.

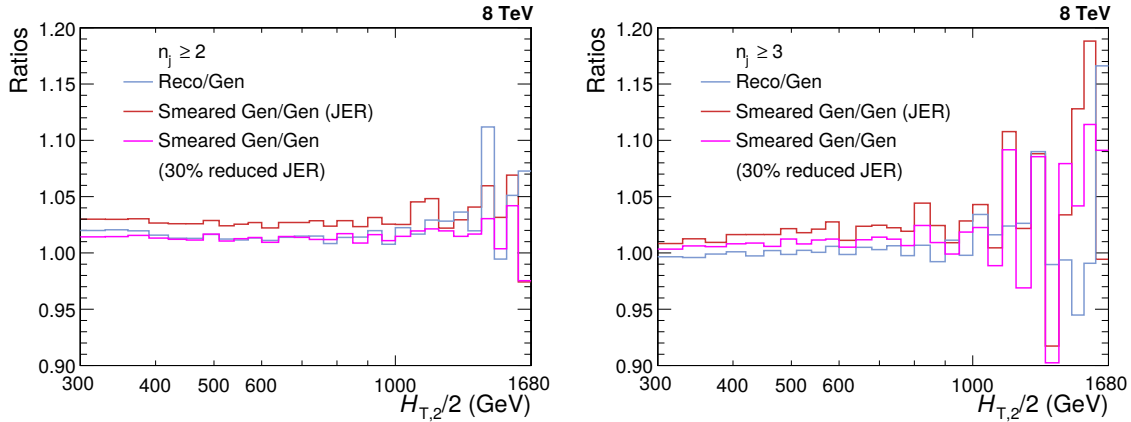


Figure 5.12: MADGRAPH5+PYTHIA6 (MG5+P6) Gen smeared using extracted jet energy resolution (JER) shows a discrepancy from simulated Reco as Smeared Gen/Gen ratio (red line) does not match with Reco/Gen ratio (blue line), for both inclusive 2-jet (left) and 3-jet events (right). Smeared Gen/Gen ratio (pink line) where Gen is smeared using 30% reduced JER matches with simulated Reco/Gen ratio (blue line) within the statistical fluctuations. Hence an additional unfolding uncertainty is attributed by comparison to 30% reduced JER.

5.5 Unfolding

One of the main goals in an experimental measurement is to do the comparison of data with theory predictions or with the results obtained from other experiments. But the finite resolution of a detector and the steeply falling jet p_T spectrum distorts

the physical quantities. As a result, the measured observables are different from their corresponding true values. Each p_T bin content contains the migrated events from neighbouring bins along with the original events. So an unfolding process of the data should be followed in order to remove detector effects. In this analysis, the measurements are corrected for detector smearing effects and unfolded to stable particle level by using the iterative D'Agostini Bayesian algorithm [97, 98] as implemented in RooUnfold software package [99]. In this algorithm, the number of iterations regularize the unfolding process. The obtained distribution in one iteration is taken as the input in the next one. χ^2 between two successive iterations is given by Eq. 5.9. The number of iterations stop when χ^2/N_{bins} is < 1 . A reduced χ^2 is obtained by a higher number of iterations but this will also increase the uncertainty and there are larger bin-by-bin fluctuations and correlations. So the optimization of number of iterations is very important. In the current analysis, unfolding done with “four” iterations gives the best results with low χ^2 and low bin-by-bin correlations.

$$\chi^2 = \sum_{i=1}^{N_{bins}} \left(\frac{n_i^{j+} - n_i^j}{\sqrt{n_i^j}} \right)^2 \quad (5.9)$$

where n_i^j number of events in i -th bin for j -th iteration.

The measured differential cross-sections as a function of $H_{T,2}/2$, are unfolded separately for $n_j \geq 2$ and $n_j \geq 3$ events. The measured cross-section ratio R_{32} is also corrected for detector smearing effects and unfolded to particle level. There can be two ways to obtain unfolded cross-section ratio :

- **Method I :** First unfold separately the inclusive 2-jet and 3-jet measured cross-sections and then construct the ratio R_{32}
- **Method II :** Unfold directly the cross-section ratio R_{32}

In further analysis, unfolded cross-section ratio R_{32} and its systematic uncer-

tainties are calculated using Method I, whereas Method II is used only to propagate the statistical uncertainties including bin-by-bin correlations and statistical correlations between the inclusive 3-jet and 2-jet events cross-sections. Unfolding takes the response matrix as an input which are explained in the next section.

5.5.1 Response Matrices

The response matrix is a two dimensional mapping between the true and measured distributions. It is usually derived from simulated Monte Carlo (MC) samples, which takes the true distribution from MC as an input and smears it by taking into account the detector resolution. Then this response matrix is used to unfold the measured data spectrum. But there are several drawbacks of constructing response matrix using this method. In some phase space regions, the shape of the distribution is not well described by the LO predictions. Also, the limited number of events in the MC samples at high transverse momenta introduces high statistical fluctuations in the response matrix.

However, there is an indirect way of constructing the response matrix which uses a custom Toy Monte Carlo method. In this method, the particle level or true $H_{T,2}/2$ spectrum is obtained by fitting the theoretically predicted NLO spectrum. Then this distribution is smeared with forward smearing technique, using the extracted jet energy resolution (JER) to obtain the reconstructed level or measured $H_{T,2}/2$ spectrum. After that, the response matrix is constructed from these two distributions is used for the unfolding procedure.

5.5.1.1 Inclusive Cross-sections

The NLO spectrum of the differential cross-sections for $n_j \geq 2$ and $n_j \geq 3$ events obtained using CT10-NLO PDF set are fitted with the following two different functions defined in Eq. 5.10 and 5.13. These functions describes the shape as well as

normalization of the distribution.

- **Function I :**

$$f(H_{T,2}/2) = N[x_T]^{-a}[1 - x_T]^b \times \exp[-c/x_T] \quad (5.10)$$

where N is normalization factor and a, b, c are fit parameters.

This function is derived from the below function [100] :

$$f(p_T; \alpha, \beta, \gamma) = N_0[p_T]^{-\alpha} \left[1 - \frac{2 p_T \cosh(y_{min})}{\sqrt{s}} \right]^{\beta} \times \exp[-\gamma/p_T] \quad (5.11)$$

using

$$\alpha = a, \quad \beta = b, \quad \gamma = c * \sqrt{s}/2, \quad x_T = \frac{2 * H_{T,2}/2 * \cosh(y_{min})}{\sqrt{s}} = \frac{2 * H_{T,2}/2}{\sqrt{s}} \quad (5.12)$$

where transverse scaling variable x_T corresponds to the proton fractional momentum x for dijets with rapidity $y = 0$, $\sqrt{s} = 8000$ GeV and y_{min} is low-edge of the rapidity bin y under consideration (here y_{min} is taken equal to 0)

- **Function II :**

$$f(H_{T,2}/2) = A_0 \left(1 - \frac{H_{T,2}/2}{A_6} \right)^{A_7} \times 10^{F(H_{T,2}/2)}, \text{ where } F(x) = \sum_{i=1}^5 A_i \left(\log \left(\frac{x}{A_6} \right) \right)^i \quad (5.13)$$

where the parameter A_6 is fixed to $\frac{\sqrt{s}}{2 \cosh(y_{min})}$, where $\sqrt{s} = 8000$ GeV and y_{min} is the minimum rapidity. The other parameters are derived from the fitting.

Figure 5.13 shows the fitted CT10-NLO spectrum of differential cross-section as a function of $H_{T,2}/2$ (green solid circles) using Function I (top) and using Function

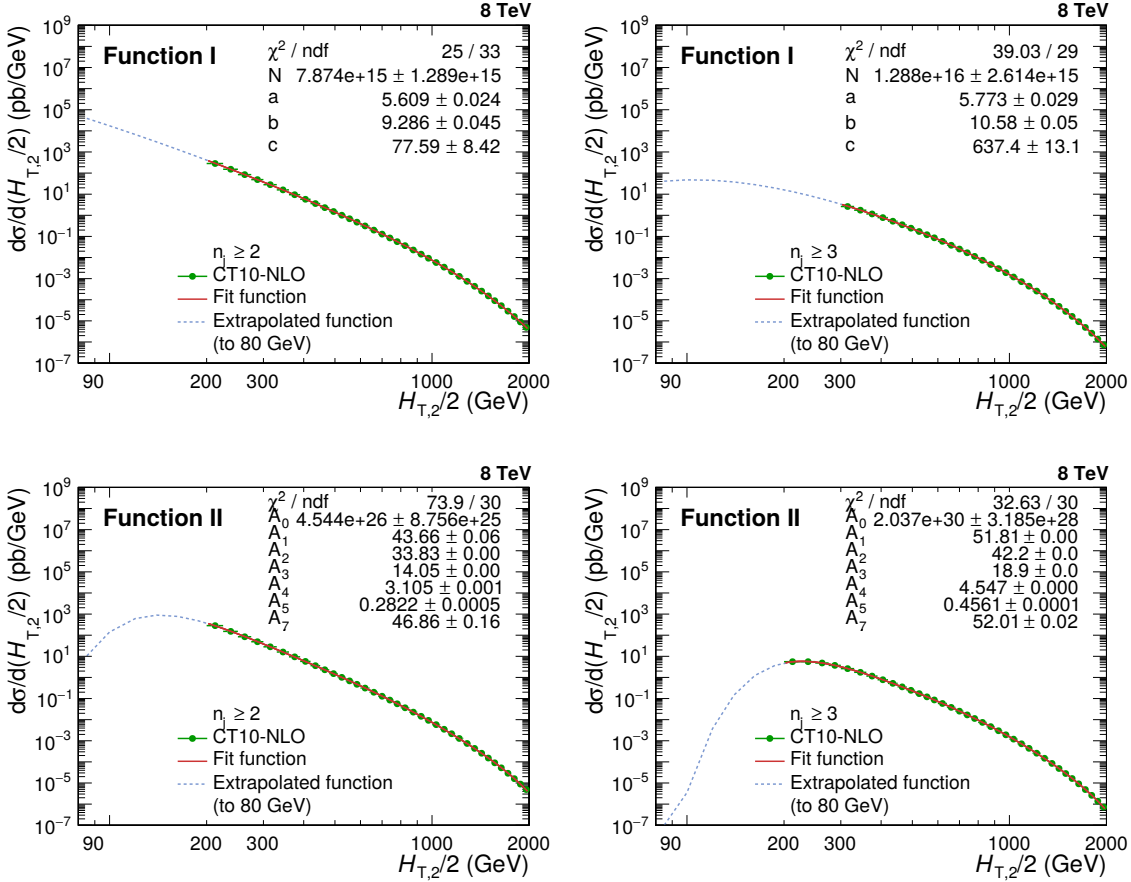


Figure 5.13: Fitted CT10-NLO spectrum of differential cross-section as a function of $H_{T,2}/2$ (green solid circles) using Function I (top) defined in Eq. 5.10 and using Function II (bottom) given by Eq. 5.13, for inclusive 2-jet (left) and 3-jet events (right). To consider the migration to lower $H_{T,2}/2$ bins, the fit functions described by red lines are extrapolated to 80 GeV (blue dashed lines).

II (bottom) : for inclusive 2-jet (left) and 3-jet events (right). Function I is used primarily to generate response matrices and perform the closure tests and Function II is used as an alternative function to calculate unfolding uncertainty, described in Sec. 5.6.3. To include the migration to lower bins, the fit functions described by red lines are extrapolated to 80 GeV (blue dashed lines).

A flat $H_{T,2}/2$ spectrum is generated by using toy Monte Carlo events and the fit parameters obtained from the NLO spectrum using function I (as shown in Fig. 5.13) provides weights to the flat spectrum. A total of ten million events are generated randomly (in $H_{T,2}/2$ range 80-2000). These generated values are then smeared with a

Gaussian function, where σ of the Gaussian is determined from the relative resolution parametrization as a function of $H_{T,2}/2$ calculated from NSC formula mentioned in equation 5.8. The parameters N, S, C used for smearing are taken from Table 5.6. These randomly generated (Gen_{Toy}) and smeared ($\text{Measured}_{\text{Toy}}$) values are used to fill the response matrices. Figure 5.14 shows the response matrices derived using the Toy MC for $n_j \geq 2$ (left) and $n_j \geq 3$ events (right). The matrices are normalized to the number of events in each column. The response matrices are diagonal as the migrations in off-diagonal bins are much smaller than the bins along the diagonal.

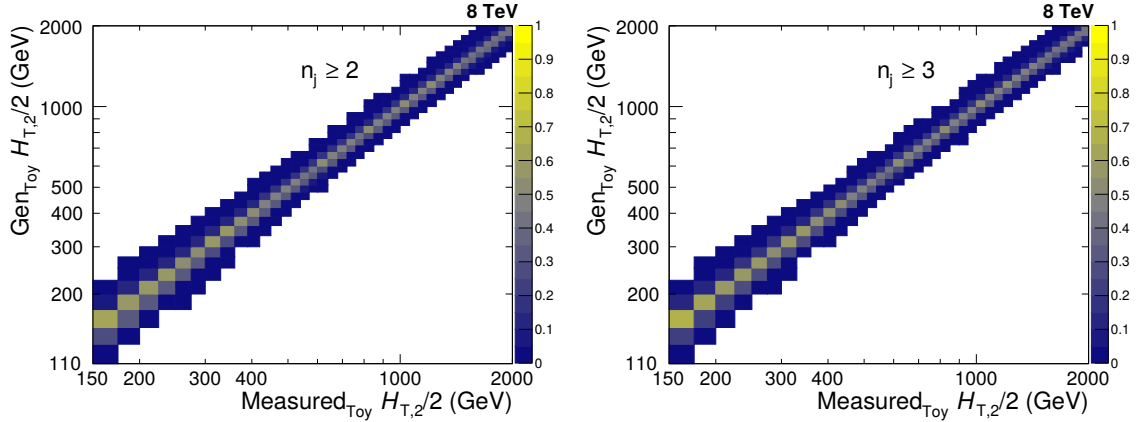


Figure 5.14: The response matrices are derived using the Toy Monte Carlo and forward smearing method, for inclusive 2-jet (left) and 3-jet events (right). The matrices are normalized to the number of events in each column and are diagonal with small off-diagonal migrations between close-by $H_{T,2}/2$ bins.

5.5.1.2 Cross-section Ratio, R_{32}

To obtain the statistical uncertainty on the unfolded cross-section ratio R_{32} , Method II is used. In this method, the response matrix is constructed using Toy MC method as done in Sec. 5.5.1.1 for differential cross-sections. To obtain the true spectrum for R_{32} , the ratio of cross-section spectrum described by Eq. 5.10 for inclusive 3-jet to that of 2-jet events is taken. This ratio is shown by green solid circles in Fig. 5.15 (left) which is fitted using a polynomial function of degree 8 (red line). Then as explained in above section, response matrix is derived for R_{32} using the Toy Monte

Carlo and forward smearing method which is shown in Fig. 5.15 (right). The matrix is normalized to the number of events in each column and is diagonal with small off-diagonal migrations between close-by $H_{T,2}/2$ bins.

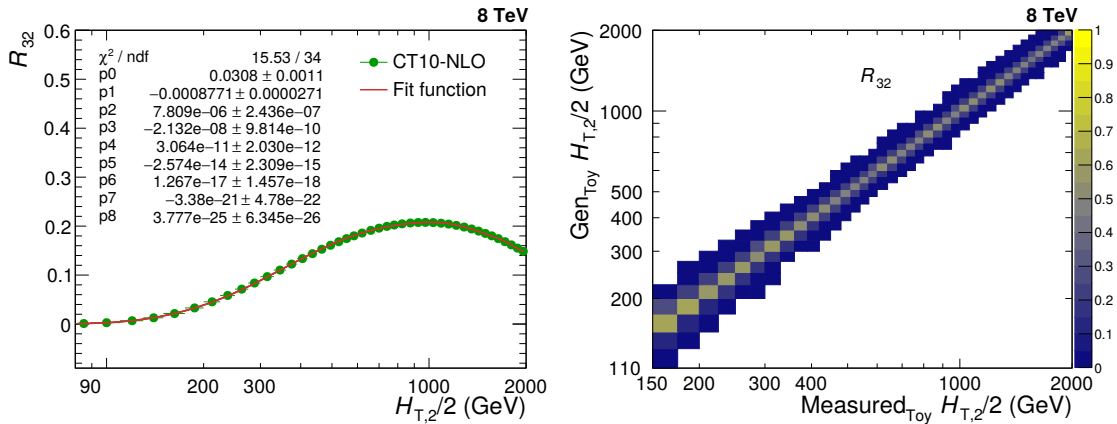


Figure 5.15: Left : The ratio of cross-sections described by Eq. 5.10 for inclusive 3-jet to that of 2-jet events is shown as a function of $H_{T,2}/2$ (green solid circles). It is fit using a polynomial function of degree 8 (red line). Right : The response matrix is derived using the Toy Monte Carlo and forward smearing method, for the cross-section ratio R_{32} . The matrix is normalized to the number of events in each column and is diagonal with small off-diagonal migrations between close-by $H_{T,2}/2$ bins.

5.5.2 Closure Test

A closure test has been performed to confirm the working of the unfolding procedure. In this test, $\text{Measured}_{\text{Toy}}$ spectrum is unfolded using the constructed response matrices shown in Figure 5.14. It is expected that the same Gen_{Toy} spectrum should be re-obtained after unfolding. Figure 5.16 confirms that the unfolded $\text{Measured}_{\text{Toy}}$ spectrum matches exactly with Gen_{Toy} spectrum as the ratio of these distributions is perfectly flat at one for both $n_j \geq 2$ (top left) and $n_j \geq 3$ events (top right) cross-sections as well as the cross-section ratio R_{32} (bottom).

For another closure test, Reco MG5+P6 MC differential cross-section distribution is unfolded using the above constructed response matrices using JER for forward smearing the randomly generated spectrum. While taking ratio of the un-

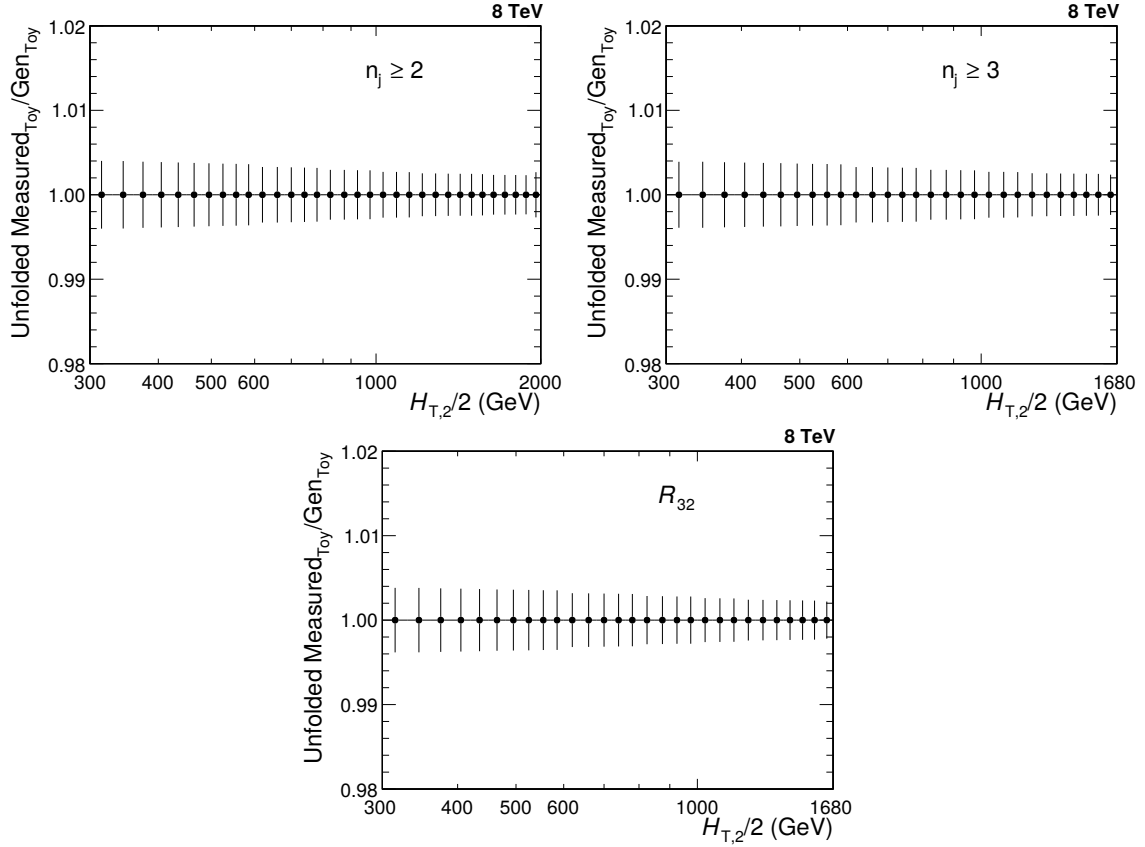


Figure 5.16: Closure test of the unfolding technique where the smeared spectrum obtained from Toy Monte Carlo method (Measured_{Toy}), is unfolded using the constructed response matrices (obtained by forward smearing the randomly generated spectrum (Gen_{Toy}) using extracted jet energy resolution (JER)). As expected, the unfolded measured_{Toy} spectrum matches exactly with Gen_{Toy} spectrum as the ratio of these distributions is perfectly flat at one for both inclusive 2-jet (top left) and 3-jet events (top right) cross-sections as well as the cross-section ratio R_{32} (bottom).

folded distribution to that of Gen MG5+P6 MC, it is observed that a well closure is not obtained. This is represented by blue line in Fig. 5.17 for $n_j \geq 2$ (top left) and $n_j \geq 3$ events (top right). As observed in Fig. 5.12 in Sec. 5.4, if Reco MG5+P6 MC is unfolded using the response matrices obtained using 30% reduced JER, then the good closure is obtained as shown by red line in Fig. 5.17. Since unfolded cross-section ratio R_{32} is the ratio of unfolded differential cross-sections (Method I), same behaviour is observed for R_{32} (bottom).

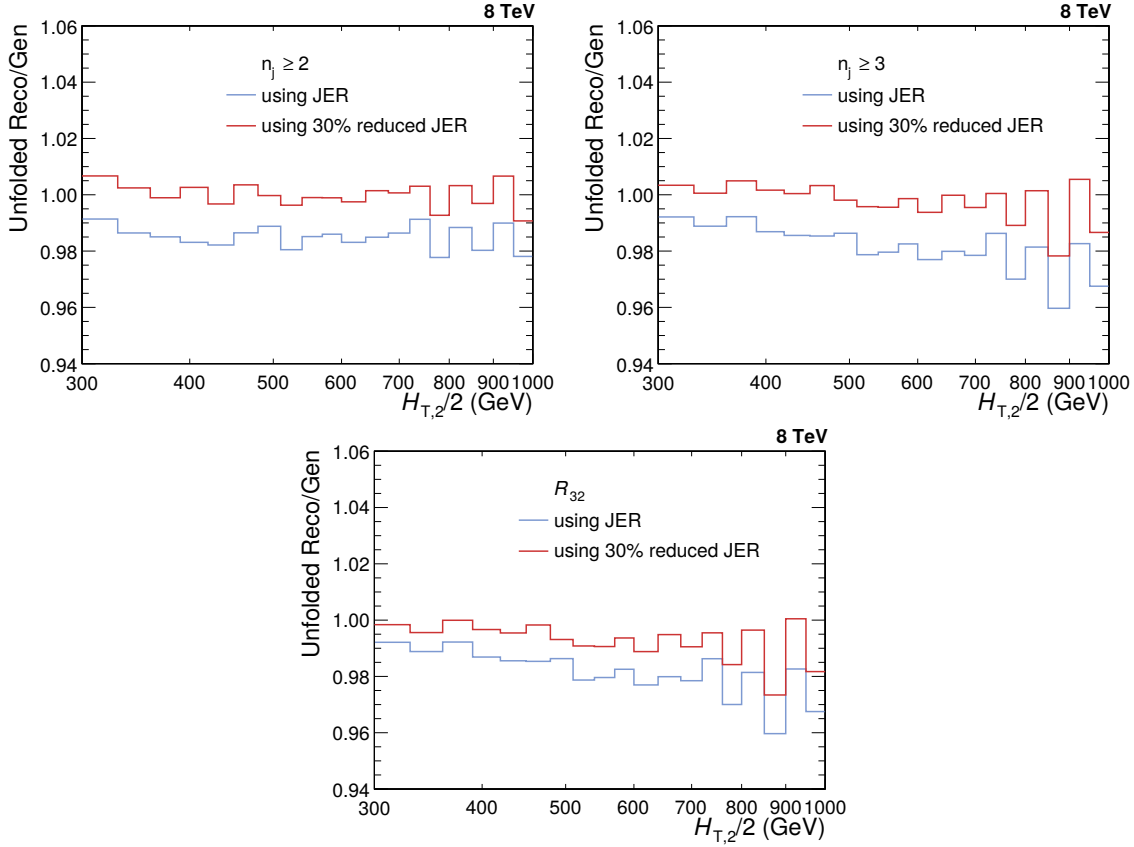


Figure 5.17: Reco MADGRAPH5+PYTHIA6 Monte Carlo (MG5+P6 MC) differential cross-section distributions unfolded with the response matrices (obtained by forward smearing the randomly generated spectrum (Gen) using extracted jet energy resolution (JER)), does not give a good closure with Gen MG5+P6 MC (blue line), for inclusive 2-jet (top left) and 3-jet events (top right). After performing the unfolding using 30% reduced JER, a good closure is obtained (red line). Since unfolded the cross-section ratio R_{32} is the ratio of unfolded differential cross-sections, same behaviour is observed for R_{32} (bottom).

5.5.3 Unfolding of the Measurement

After validity the unfolding method, the measured differential cross-sections as well as R_{32} are unfolded using the above reconstructed response matrices. The unfolded data spectrum is compared to that of measured one in Fig. 5.18 for $n_j \geq 2$ (top left) and $n_j \geq 3$ events (top right) cross-sections and for the cross-section ratio R_{32} (bottom). As already discussed that 30% reduced JER gives better closures than JER, so the unfolding of data is done with response matrices using JER (blue solid circles) as well as 30% reduced JER (red solid circles) for smearing. The difference

between both is taken as an additional uncertainty on the unfolded measurement.

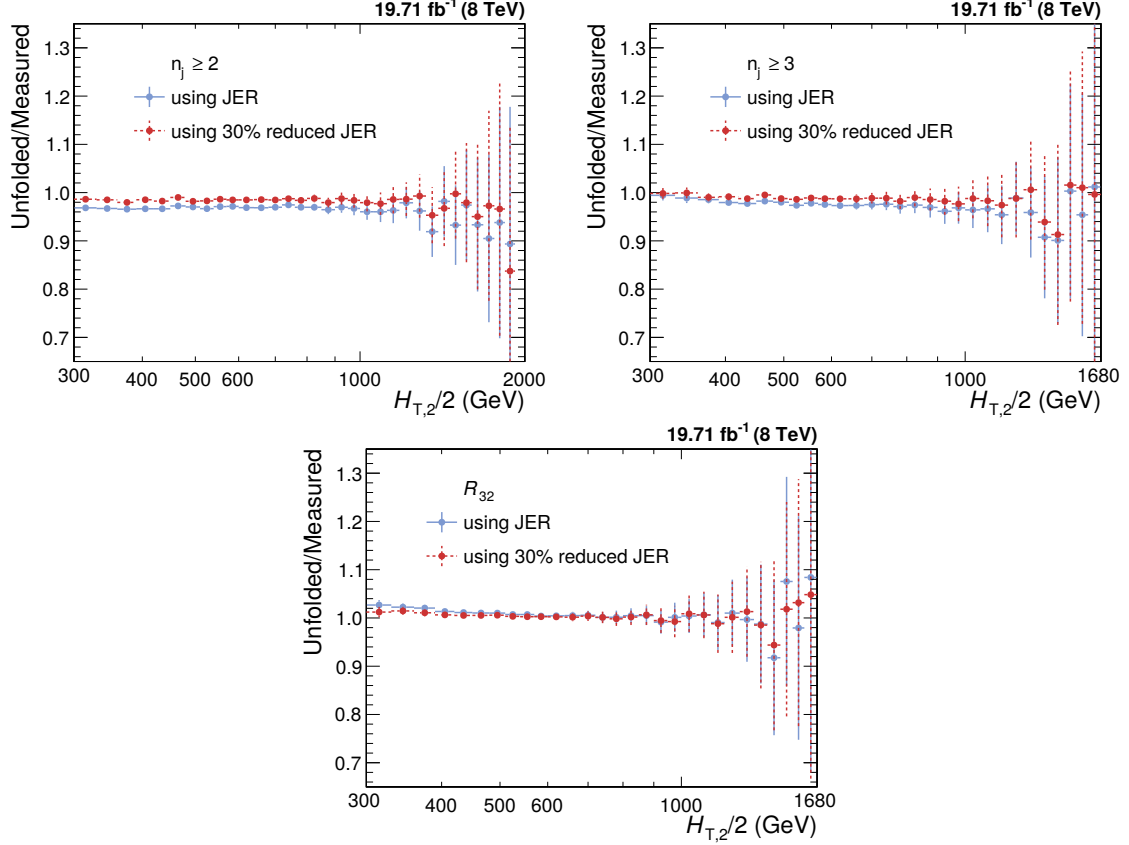


Figure 5.18: The measured differential cross-sections as well as the cross-section ratio R_{32} are unfolded as a function of $H_{T,2}/2$ using the response matrices derived using the Toy Monte Carlo and forward smearing method. The unfolded spectrum are compared with that of the measured one for inclusive 2-jet (top left) and 3-jet events cross-sections (right) as well as for R_{32} (bottom). The unfolding is done with response matrices using JER (blue solid circles) as well as 30% reduced JER (red solid circles) for smearing. The difference between both is taken as an additional uncertainty on the unfolded measurement.

5.6 Experimental Uncertainties

In an experimental measurement of any physical observable, the uncertainties play a key role and hence are important to study in a physics analysis. The uncertainties can be categorized into two types : statistical and systematic. The statistical uncertainties arise due to random fluctuations depending on the number of events. The more the number of events, less is the statistical uncertainty. The systematic

uncertainties may be due to known detector effects, model dependence, assumptions made or various corrections applied. In general, if the statistical and systematic uncertainties are uncorrelated, these can be added in quadrature to obtain the total uncertainty on the measurement. In this section, all the experimental uncertainties affecting the measurement of cross-sections and the cross-section ratio R_{32} are described. The systematic experimental uncertainties for R_{32} are propagated from the cross-sections to the ratio taking into account correlations. Due to this, the systematic uncertainties may cancel for R_{32} completely or partially as compared to those for the individual cross-sections.

5.6.1 Statistical Uncertainty

Statistical uncertainty on the measurement is obtained through the unfolding procedure using a toy MC method. The measured data points are smeared within their statistical uncertainties to get the smeared spectrum. Such smeared spectrums are produced million in number and the unfolding is performed multiple times for each smeared spectra. The differences between the unfolded spectrums and the measured one give the statistical uncertainty. The unfolding process introduces more statistical fluctuations which can be observed in Fig. 5.19. Here the fractional statistical uncertainties of the unfolded data (red line) are compared with those of the measured one (blue line) for $n_j \geq 2$ (top left) and $n_j \geq 3$ events cross-sections (top right) as well as for the cross-section ratio R_{32} (bottom).

After the unfolding, the final statistical uncertainties become correlated among the bins such that the size of these correlations varies between 10 and 20%. The correlation (anti-) is more significant for neighbouring bins in $H_{T,2}/2$ as compared to the far off ones. In Fig. 5.20, the correlations of the statistical uncertainty after the unfolding can be seen for $n_j \geq 2$ (top left) and $n_j \geq 3$ events cross-sections (top right) and for the cross-section ratio R_{32} (bottom). These correlations must be considered while performing the fits to extract the value of the strong coupling

constant, α_S .

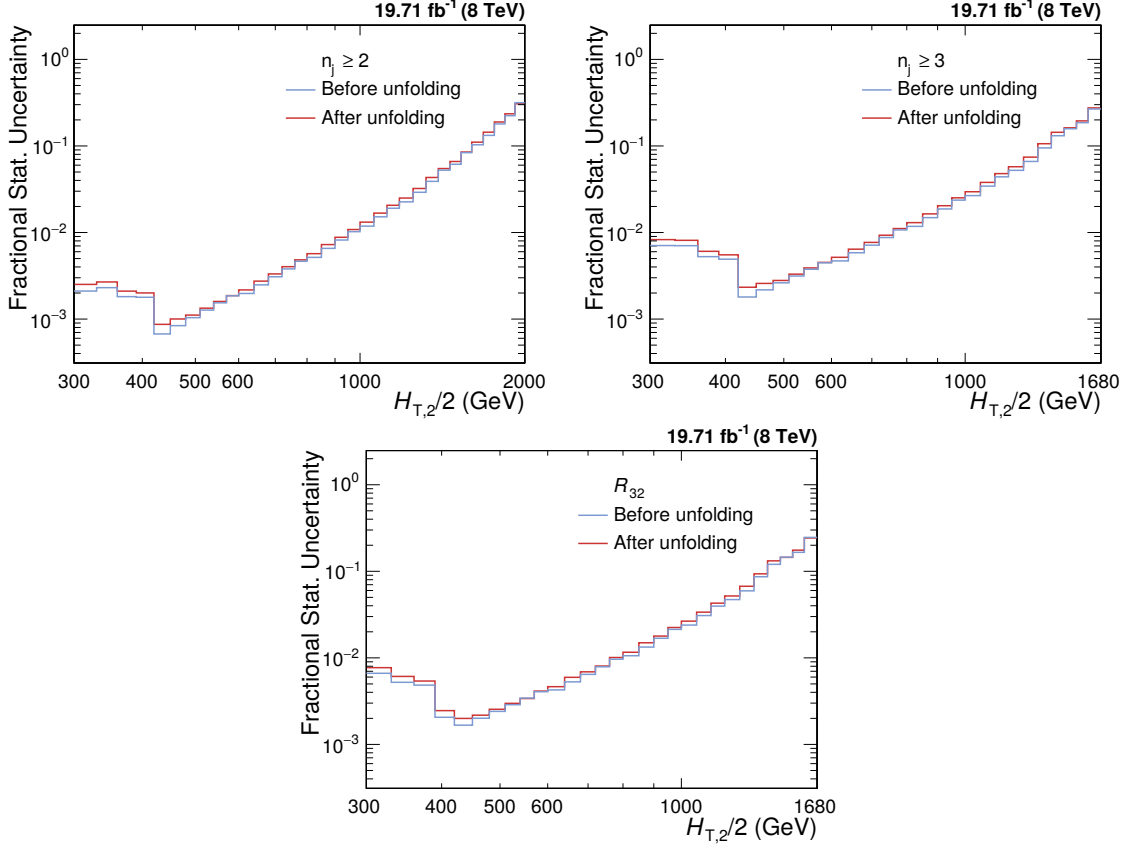


Figure 5.19: The fractional statistical uncertainties of the unfolded data (red line) are compared with those of the measured one (blue line) for inclusive 2-jet (top left) and 3-jet events cross-sections (top right) as well as for the cross-section ratio R_{32} (bottom). After unfolding, the statistical uncertainty increases slightly.

5.6.2 Jet Energy Corrections Uncertainty

As explained in Sec. 4.3.2, the measured jet energy is corrected for a variety of detector effects by using jet energy corrections (JEC). This process introduces uncertainties in the final corrected jet energy. There are 25 mutually independent sources which contribute to JEC. Each source presents a 1σ shift and is fully correlated in p_T and η but uncorrelated to all other sources. The observable is studied with the nominal values of the jet energy which gives nominal distributions as well as by varying up and down the energy of all jets by the uncertainty. The differences

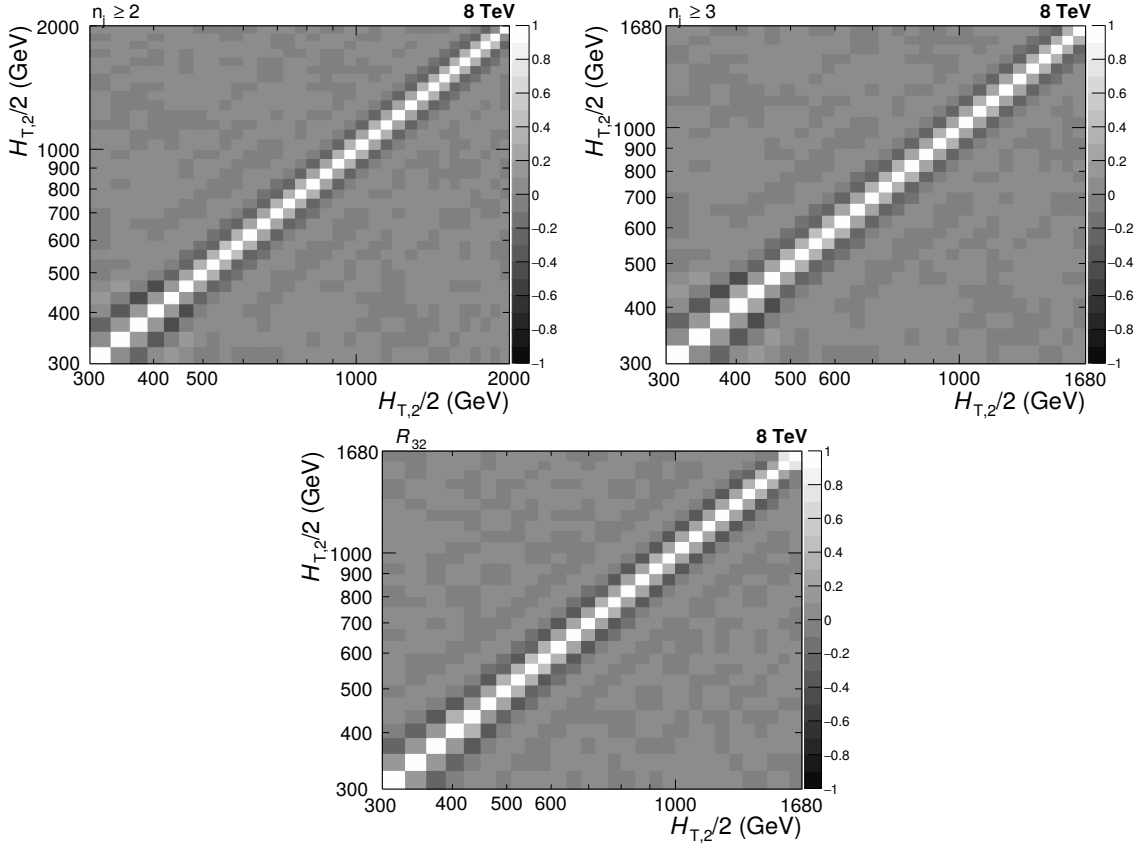


Figure 5.20: The unfolding procedure introduces the correlations of the statistical uncertainty through bin migrations which are shown here for inclusive 2-jet (top left) and and 3-jet events cross-sections (top right) as well as for the cross-section ratio R_{32} (bottom). The correlation (anti-) is more significant between neighbouring bins than far-ff ones.

between the nominal distributions and the ones obtained by varying the jet energy gives the uncertainties from each source. The JEC uncertainties can be asymmetric in nature which leads to separate treatment of upwards and downwards variation of each source. The sum in quadrature of uncertainties from all sources gives the total JEC uncertainty. In the current analysis, JEC uncertainties are a dominant source of experimental uncertainty at low $H_{T,2}/2$. The JEC uncertainty ranges from 3% to 10% for $n_j \geq 2$ and from 3% to 8% for $n_j \geq 3$ events cross-sections measurement. To calculate JEC uncertainty for ratio R_{32} , the inclusive 2-jet and 3-jet events cross-sections are measured as a function of $H_{T,2}/2$ by shifting the jet p_T according to the JEC uncertainty for each source of JEC separately. Then the ratio of these cross-

sections is taken and the difference of these from the central ratio R_{32} , gives the JEC uncertainty for R_{32} . As expected, JEC uncertainty for R_{32} is small as compared to that for individual cross-sections and is about 1 to 2% over all $H_{T,2}/2$ bins.

The sources of JEC considered in the current measurements are : AbsoluteStat, AbsoluteScale, AbsoluteFlavMap, AbsoluteMPFBias, Fragmentation, SinglePiononECAL, SinglePionHCAL, FlavorQCD, RelativeJEREC1, RelativeJEREC2, RelativeJERHF, RelativePtBB, RelativePtEC1, RelativePtEC2, RelativePtHF, RelativeFSR, RelativeStatFSR, RelativeStatEC2, RelativeStatHF, PileUpDataMC, PileUpPtRef, PileUpPtBB, PileUpPtEC1, PileUpPtEC2 and PileUpPtHF. The AbsoluteFlavMap uncertainty is exactly zero for the 8 TeV and can be ignored. For the four sources : RelativeJERHF, RelativePtHF, RelativeStatHF, PileUpPtHF, the JEC uncertainty is exactly zero because of $|y| < 2.5$ cut used in the analysis. So only 20 sources contribute to the total JEC uncertainty. The Figs. A.1-A.3 show the JEC uncertainty from each source separately for inclusive 2-jet (top) and 3-jet events cross-sections (middle) as for cross-section R_{32} (bottom). Depending on the origin of sources, they are categorized into four groups which are described below in brief :

1. **Pileup** - This uncertainty originates from the differences in the transverse momentum between the true offset and the Random Cone method (i.e. essentially difference of pileup inside and outside of jets), in simulated events. This uncertainty is derived from Z/γ +jet, dijet and multijet data using fit procedure to estimate the residual pileup uncertainty after the calibration.
2. **Relative** - The forward jets are calibrated by the relative η -dependent corrections using dijet events. The main contribution to the uncertainty comes from jet energy resolution (JER), derived by varying JER scale factors up and down by quoted uncertainties and the initial and final state radiation bias corrections.

3. **Absolute** - A global fit to Z/γ +jet and multijet events gives the absolute calibration of the jet energy scale. The uncertainties are related to the lepton momentum scale for muons in $Z (\rightarrow \mu\mu)$ +jet and the single pion response in the HCAL.
4. **Flavor** - Flavor response differences are studied from simulation by cross-checking the results with quark- and gluon-tagged γ +jet and Z +jet events. These uncertainties are based on PYTHIA6.4 and HERWIG++2.3 differences propagated through the data-based calibration method.

The details of the jet energy corrections and uncertainties can be found in [101].

5.6.3 Unfolding Uncertainty

The unfolding uncertainty is comprised of three uncertainties which are explained as follows :

1. **Jet Energy Resolution** - The calculation of the jet energy resolution (JER) using simulated MG5+P6 Monte Carlo events is already explained in Sec. 5.4. As mentioned before, the measured jet transverse momentum (p_T) in simulated MC events needs to be smeared additionally to match the resolution in data. This smearing is done by using measured scale factors ($c_{central}$) mentioned in Table 5.5. It is recommended by JETMET group that the uncertainty on these measured scaling factors must be taken into account in a physics analysis. Since JER is used in constructing the response matrix which is an input in unfolding procedure, so the uncertainty on scale factors accounts for the unfolding uncertainty. To calculate JER uncertainty, p_T is smeared with two additional sets of scale factors corresponding to varying the factors up and down by one sigma, and corresponding $H_{T,2}/2$ is calculated. Then again JER is calculated as a function of $H_{T,2}/2$ using these upwards (c_{up}) and downwards (c_{down}) variations of the scaling factors. Alternative response matrices are built

using the JER with above variations and the unfolding is performed again. The differences of the obtained unfolded spectrums to the nominal ones accounts for a systematic JER uncertainty.

2. **Model Dependence** - It is explained in Sec. 5.5.1 that to obtain the true $H_{T,2}/2$ spectrum to be used in constructing response matrix using Toy MC method, the fitting of the CT10-NLO predictions is performed with the Function I described in Eq. 5.10. Using the alternative function, Function II given by Eq. 5.13, for this fitting and then constructing different response matrix, gives the model dependence of the true $H_{T,2}/2$ spectrum. The differences in unfolded distributions using the above mentioned two different response matrices gives the model dependence uncertainty.
3. **Additional Uncertainty** - Small nonclosures observed in Fig. 5.12 introduces a supplementary uncertainty which is attributed by comparison of distributions unfolded using response matrices constructed using JER from simulation with that obtained with a 30% reduced JER.

All the three above mentioned uncertainties are added in quadrature to get the total unfolding uncertainty which increases from about 1% at low $H_{T,2}/2$ up to 2% at the high $H_{T,2}/2$ ends of the cross-sections for both $n_j \geq 2$ and $n_j \geq 3$ events. This uncertainty account for about less than 1% for R_{32} .

5.6.4 Luminosity Measurement Uncertainty

As discussed in Sec. 3.1.1, the luminosity delivered to CMS detector by LHC in the proton-proton collisions in the year of 2012 is measured by using the silicon pixel cluster counting method [55]. The uncertainty related to the integrated luminosity measurement is estimated to be 2.5% (syst.) and 0.5% (stat.). This uncertainty propagates directly to any absolute cross-section measurement. Hence, a total systematic uncertainty of 2.6% is considered across all the $H_{T,2}/2$ bins. At low $H_{T,2}/2$,

it is similar in size as the one from JEC. This uncertainty cancels completely for R_{32} .

5.6.5 Residual Uncertainty

The small trigger and jet identification inefficiencies account for smaller than 1% uncertainties on the cross-section measurements [91, 102]. Hence, an uncorrelated residual uncertainty of 1% is assumed across all $H_{T,2}/2$ bins for both $n_j \geq 2$ and $n_j \geq 3$ events cross-sections whereas for R_{32} , it gets cancel completely.

5.6.6 Total Experimental Uncertainty

After calculating the uncertainties from all the above mentioned sources, the total experimental uncertainty on measurement of cross-sections as well as cross-section ratio R_{32} , is obtained by adding in quadrature the uncertainties from individual sources. Figure 5.21 shows the experimental uncertainties, from different sources as well as the total uncertainty, affecting the measurement of $n_j \geq 2$ (top left) and $n_j \geq 3$ events cross-sections (top right) and cross-section ratio R_{32} (bottom). The error bars represent the statistical uncertainty obtained after unfolding. The systematic uncertainties due to jet energy corrections (JEC by blue line), luminosity (red dashed line), unfolding (green dashed line) and residual effects (light purple line) are also presented. The uncertainties due to luminosity and residual effects cancel completely in R_{32} . The total uncertainty (black dashed line) on the measurements is asymmetric in nature and dominated by the uncertainty due to the jet energy corrections (JEC) at lower $H_{T,2}/2$ values and by statistical uncertainty at higher $H_{T,2}/2$ values.

The experimental uncertainties from each source as well as total uncertainty are also quoted in Table 5.7. The values of uncertainties (in %) from each source as well as total uncertainty, for each $H_{T,2}/2$ bin, are tabulated in Tables A.2, A.3

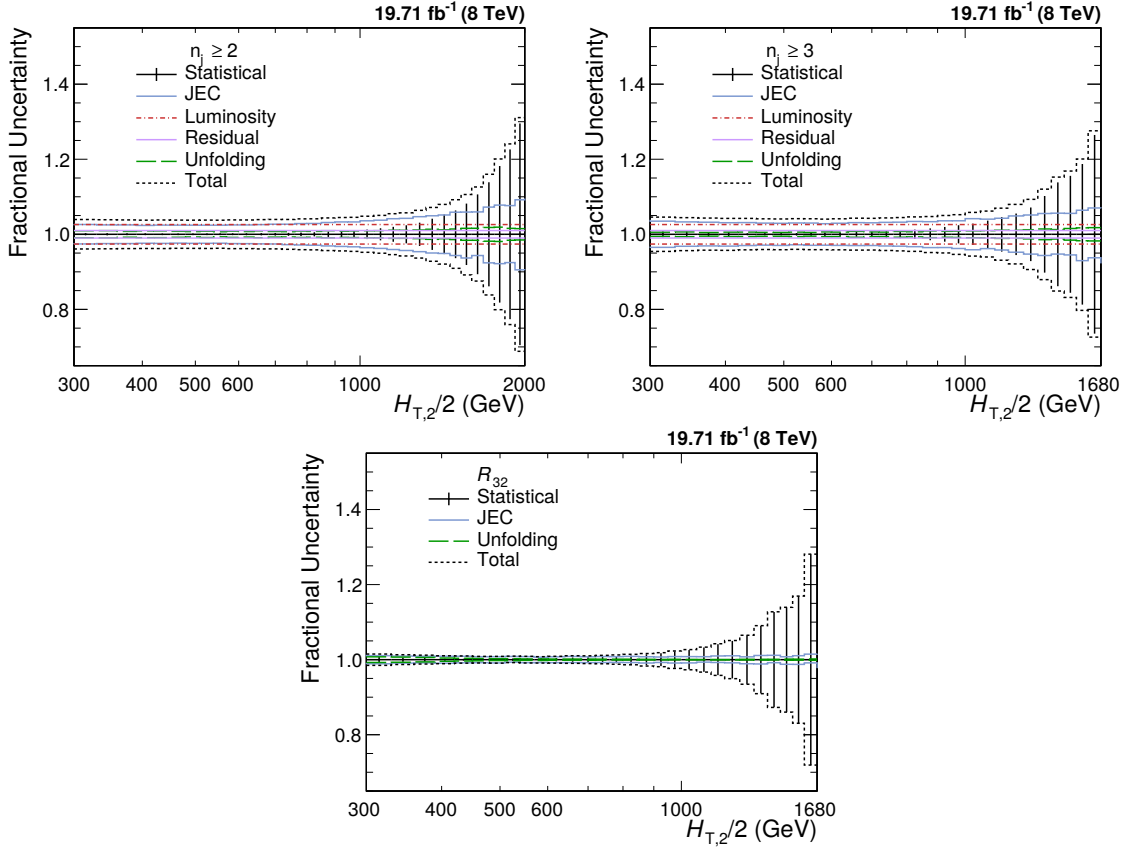


Figure 5.21: Experimental uncertainties from different sources affecting the measurement of cross-sections for inclusive 2-jet (top left) and 3-jet events (top right) and cross-section ratio R_{32} (bottom). The error bars represent the statistical uncertainty after unfolding. The systematic uncertainties due to jet energy corrections (JEC by blue line), luminosity (red dashed line), unfolding (green dashed line) and residual effects (light purple line) are also presented. The uncertainties due to luminosity and residual effects cancel completely in R_{32} . The total uncertainty (black dashed line) is the quadrature sum of the individual sources of uncertainty.

and A.4 for $n_j \geq 2$ and $n_j \geq 3$ events cross-sections and cross-section ratio R_{32} , respectively.

The complete data analysis of the differential inclusive 2-jet and 3-jet events cross-sections as well as their ratio R_{32} has been presented as a function of $H_{T,2}/2$. The measured spectrums after correcting for detector effects through the unfolding procedure, are compared with the next-to-leading order (NLO) pQCD calculations in the next chapter.

Table 5.7: An overview of all experimental uncertainties affecting the measurement of cross-sections for inclusive 2-jet (left) and 3-jet events (middle) and cross-section ratio R_{32} (right). The uncertainties due to luminosity and residual effects cancel completely in R_{32} . The total uncertainty is the quadrature sum of the individual sources of uncertainty.

Uncertainty Source	Inclusive 2-jet	Inclusive 3-jet	R_{32}
Statistical	< 1 to 30%	< 1 to 27%	< 1 to 28%
Jet energy corrections (JEC)	3 to 10%	3 to 8%	1 to 2%
Unfolding	1 to 2%	1 to 2%	< 1%
Luminosity	2.6%	2.6%	cancels
Residual	1%	1%	cancels
Total	4 to 32%	4 to 28%	1 to 28%

Chapter 6

Theoretical Calculations

In an experiment, the measurements are validated by doing the comparison with the perturbative QCD (pQCD) theoretical calculations. The lowest order (LO) calculations describe well the shapes of the measured distributions but not the normalization due to the dependence on the unphysical renormalization (μ_r) and factorization (μ_f) scales. The next-to-leading order calculations (NLO) improves the precision by reducing the dependence on μ_r and μ_f scales and become an essential feature in the determination of fundamental parameters such as α_S and the parton distribution functions (PDF). This chapter describes the next-to-leading order pQCD calculations used for comparison with the measurements. NLO pQCD calculations need to be corrected for the multi-parton interactions (MPI) and hadronization effects by applying non-perturbative (NP) corrections and also for the electroweak interactions (EW).

6.1 Fixed Order NLO Calculations

The predictions of the inclusive differential jet event cross-section at NLO accuracy in pQCD are computed with the NLOJET++ program version 4.1.3 [62, 63]. The results are provided within the framework of FASTNLO version 2.3 [64, 65]. The

PDFs are accessed through the LHAPDF6 library [66, 67]. The FASTNLO is preferred over the direct calculation with NLOJET++ because with FASTNLO the calculations of the cross-sections can be repeated several times with different PDFs and scale choices required for calculating the PDF and scale uncertainties. Here the factorization and renormalization scales are chosen equal to $H_{\mathrm{T},2}/2$, i.e. $\mu_f = \mu_r = H_{\mathrm{T},2}/2$.

In the current study, different PDF sets available for a series of different assumptions on the strong coupling constant at the scale of the Z boson mass $\alpha_s(M_Z)$ are used for NLO calculations. Table 6.1 summarizes the already existing PDF sets in LHC Run 1 (upper rows) and the newer PDF sets for Run 2 (lower rows). The different columns list the number of flavours N_f , the assumed masses M_t and M_Z of the top quark and the Z boson, respectively, the default values of $\alpha_s(M_Z)$, and the range in $\alpha_s(M_Z)$ variation available for fits for different PDF sets. All sets uses a variable-flavour number scheme with at most five or six flavours apart from the ABM11 PDFs, which employ a fixed-flavour number scheme with $N_F = 5$. Out of these eight PDF sets the following three are not considered further because of the below mentioned reasons :

- At NLO, predictions based on ABM11 do not describe LHC jet data at small jet rapidity [103–106].
- The HERAPDF2.0 set exclusively fits HERA DIS data with only weak constraints on the gluon PDF.
- The range in values available for $\alpha_s(M_Z)$ is too limited for the NNPDF3.0 set.

Mainly CT10 PDF set is considered for comparison between data and theory predictions as well as for calculating theoretical uncertainties.

Table 6.1: NLO PDF sets are available via LHAPDF6 with various assumptions on the value of $\alpha_s(M_Z)$. The upper rows list the already existing sets in LHC Run 1 and newer ones for Run 2 are listed in lower rows, along with the corresponding number of flavours N_f , the assumed masses M_t and M_Z of the top quark and the Z boson, respectively, the default values of $\alpha_s(M_Z)$, and the range in $\alpha_s(M_Z)$ variation available for fits.

Base set	N_F	M_t (GeV)	M_Z (GeV)	$\alpha_s(M_Z)$	$\alpha_s(M_Z)$ range
ABM11 [27]	5	180	91.174	0.1180	0.110 - 0.130
CT10 [107]	≤ 5	172	91.188	0.1180	0.112 - 0.127
MSTW2008 [108, 109]	≤ 5	10^{10}	91.1876	0.1202	0.110 - 0.130
NNPDF2.3 [110]	≤ 6	175	91.1876	0.1180	0.114–0.124
CT14 [24]	≤ 5	172	91.1876	0.1180	0.111–0.123
HERAPDF2.0 [28]	≤ 5	173	91.1876	0.1180	0.110–0.130
MMHT2014 [25]	≤ 5	10^{10}	91.1876	0.1200	0.108–0.128
NNPDF3.0 [26]	≤ 5	173	91.2	0.1180	0.115–0.121

6.1.1 NLO Correction Factors

The differences between LO predictions and NLO predictions give the effect of the higher-order contributions to the pQCD predictions. These are described by a NLO correction factor, k-factor, which is derived as the ratio of cross-sections at NLO accuracy to that at LO i.e.

$$\text{k-factor} = \frac{\sigma_{\text{NLO}}}{\sigma_{\text{LO}}} \quad (6.1)$$

The impact of the higher-order corrections is determined by the size of k-factor. The small size of k-factor indicates that the cross-section predictions are precisely described at the LO whereas the larger size hints the contributions from NLO. Figure 6.1 shows the k-factors of the NLOJET++ calculations, for inclusive 2-jet and 3-jet event cross-sections and their ratio R_{32} , using five different PDF sets. k-factor for R_{32} is obtained by taking the ratio of k-factors for inclusive 3-jet event cross-sections to that of inclusive 2-jet. The k-factors are similar for all the PDF sets in the lower region, but the differences increase in regions with larger $H_{T,2}/2$. It is observed that for inclusive 3-jet event cross-sections, k-factor jumps at lowest

$H_{T,2}/2$. This is because some jet configurations are kinematically forbidden near the p_T cut bin i.e. 150 GeV. Since the first few bins in $H_{T,2}/2$ (below 225 GeV) still suffer from these kinematical effects, the minimum value of $H_{T,2}/2$ studied is 300 GeV.

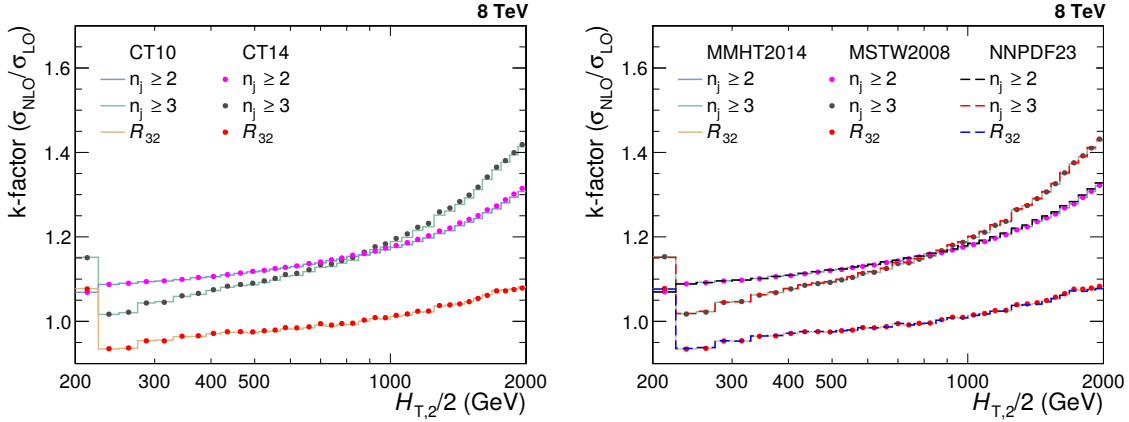


Figure 6.1: The k-factors of the NLOJET++ calculations, for inclusive 2-jet and 3-jet event cross-sections and their ratio R_{32} , using five different PDF sets.

6.1.2 Non-perturbative Corrections

The fixed-order pQCD NLO calculations predict the parton-level cross-section but lacks accuracy due to several effects. The partons which are emitted close to each other in phase space are not handled well in lower order perturbation theories and hence requires a parton shower (PS) correction. The scattering phenomena between partons within a colliding proton, other than the hard scattering, give rise to multi-parton interactions (MPI). The partons of the hard scattering forms colorless bound states called hadrons through a process of hadronization (HAD). The MPI and hadronization cannot be modelled well within the perturbative framework. Since the fixed-order NLO calculations do not include these additional soft QCD effects, these calculations cannot be compared directly to unfolded data. So the corrections for non-perturbative effects (NP) should be taken into account in NLO calculations. The ratio of cross-section predicted with a nominal event generation interfaced to

the simulation of UE contributions and to the one without hadronization and MPI effects gives the NP correction factors which are defined as :

$$C^{\text{NP}} = \frac{\sigma^{\text{PS+HAD+MPI}}}{\sigma^{\text{PS}}} \quad (6.2)$$

In the current study, the NP effects are estimated by using samples obtained from various MC event generators with a simulation of parton shower and underlying-event (UE) contributions. The leading order (LO), HERWIG++ with the default tune of version 2.3 and PYTHIA6 with tune Z2*, and the NLO POWHEG MC event generators are considered. The matrix-element calculation is performed with POWHEG interfaced to PYTHIA8 with tune CUETS1 for the UE simulation. The ratio, defined in Eq. 6.2, is obtained for each MC generator and is fitted by a power-law function defined in Eq. 6.3. Since this ratio obtained from different MC generators have large differences, so the average of the envelope, which covers all the differences, is taken as the correction factor which is then applied as bin-by-bin multiplicative factor to the parton-level NLO cross-section. The half of the envelope it is taken as the uncertainty on the NP correction factor.

$$f(H_{\text{T},2}/2) = a \cdot (H_{\text{T},2}/2)^b + c \quad (6.3)$$

The NP correction factors, $C_{3\text{-jet}}^{\text{NP}}$ and $C_{2\text{-jet}}^{\text{NP}}$ are calculated for $n_j \geq 2$ and $n_j \geq 3$ event cross-sections respectively and then their ratio gives the correction factor for R_{32} . The correction factors are shown in Fig. 6.2 for the inclusive 2-jet (top left) and 3-jet event cross-sections (top right), and for ratio R_{32} (bottom). At $H_{\text{T},2}/2 \sim 300$ GeV, the NP corrections amount to $\sim 4\text{-}5\%$ for inclusive 2-jet and 3-jet event cross-sections and $\sim 1\%$ for R_{32} , and decrease rapidly for increasing $H_{\text{T},2}/2$. On comparing the NP correction factors of R_{32} with that for individual cross-sections, it has been observed that the non-perturbative effects get reduced in R_{32} .

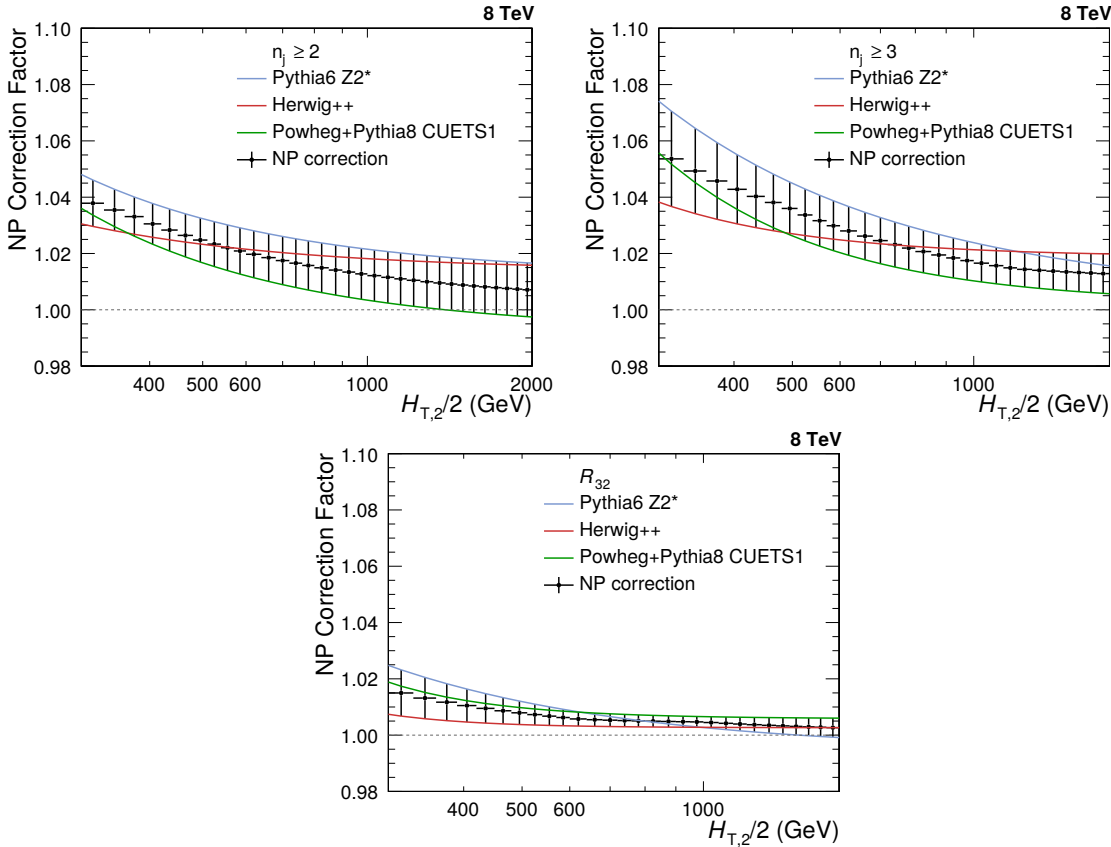


Figure 6.2: The nonperturbative (NP) corrections are presented as a function of $H_{T,2}/2$ for inclusive 2-jet (top left) and 3-jet (top right) event cross-sections, as well as their ratio R_{32} . These corrections are calculated from the leading order HERWIG++ with the default tune of version 2.3 (red line) and PYTHIA6 with tune Z2* (blue line); and the next-to-leading order POWHEG interfaced to PYTHIA8 with tune CUETS1 (green line) Monte Carlo event generators. The black solid circles give the average NP correction factor along with the uncertainty shown by the error bars.

6.1.3 Electroweak Corrections

In LHC, the center-of-mass energy of proton-proton collisions is well beyond the electroweak (EW) scale $\sim \mathcal{O}(100 \text{ GeV})$. At such a high energy, the impact of higher order EW corrections is much more with respect to QCD effects [111] and affect jet cross-sections at large $H_{T,2}/2$. The quark-quark scattering processes involving virtual exchanges of massive W and Z bosons contribute to electroweak (EW) corrections. The fixed-order QCD calculations do not include EW corrections and hence the NLO theory calculations are corrected for EW effects. The EW corrections have

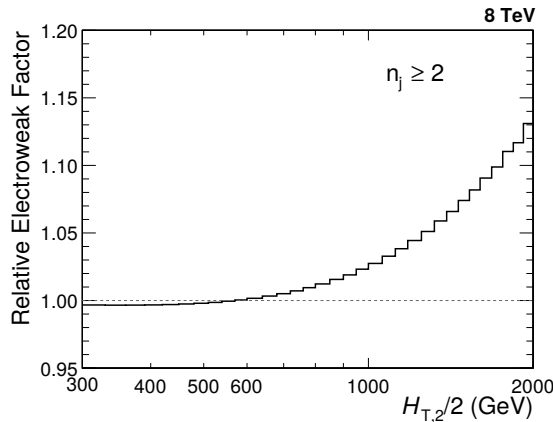


Figure 6.3: The electroweak (EW) corrections [112] in the phase space of the measurement are shown as a function of $H_{T,2}/2$ for inclusive 2-jet event cross-sections. These corrections are applied as a bin-by-bin correction factor to the fixed-order calculation of NLOJET++ as well as the MC predictions of MADGRAPH5+PYTHIA6. The EW correction factor increases up to 13% at high ends of $H_{T,2}/2$ and significantly improves the agreement between data and prediction.

been calculated for inclusive 1-jet and 2-jet case, in Ref. [112]. The EW correction factors in the phase space of the measurement are shown as a function of $H_{T,2}/2$ in Fig. 6.3 for inclusive 2-jet event cross-sections. These correction factor increases up to 13% at high ends of $H_{T,2}/2$ which are applied as a bin-by-bin correction factor to the fixed-order NLOJET++ calculations. To see the effects of EW corrections, a ratio of data to theory predictions obtained using CT10-NLO PDF set and corrected with NP effects without including EW corrections (left) and including EW corrections (right) is plotted for inclusive 2-jet event cross-sections in Fig. 6.4. On comparing both the figures, it is observed that the EW corrections significantly improve the agreement between data and prediction in the high $H_{T,2}/2$ region. EW corrections are not available yet for inclusive 3-jet production and hence not applied for inclusive 3-jet event cross-sections. The guess from theory side is that EW for inclusive 2-jet and 3-jet will be similar, so for R_{32} , it is assumed to be equal to the factor of 1. Since the EW effects are not taken care of in MC simulations so these corrections are applied to MC predictions also.

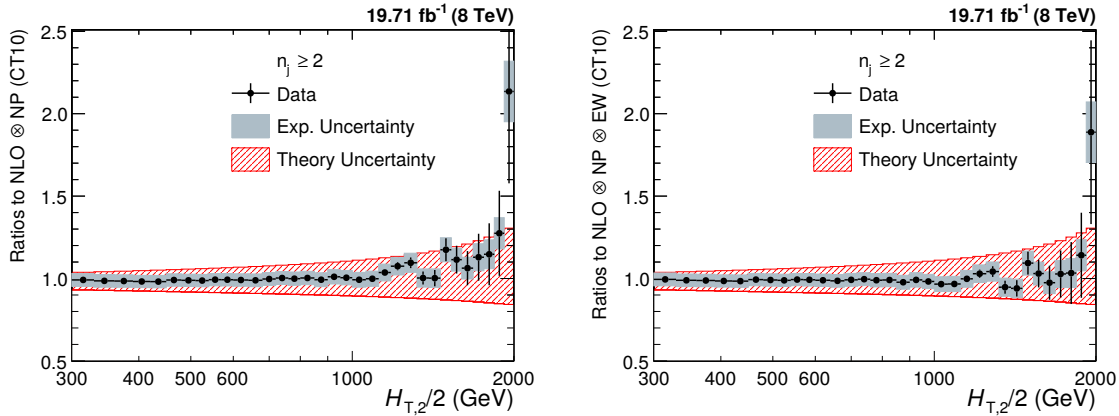


Figure 6.4: Ratio of data over theory obtained using the CT10-NLO PDF set and corrected with non-perturbative effects (NP) without including electroweak (EW) corrections (left) and including EW corrections (right) is shown for inclusive 2-jet event cross-sections. The error bars represents the statistical uncertainty of the data and the shaded rectangles represents the total experimental systematic uncertainty. The shaded band around unity indicate the total uncertainty of the theory. The EW corrections significantly improve the agreement between data and prediction in the high $H_{T,2}/2$ region.

6.2 Theoretical Uncertainties

The measurements are not only sensitive to experimental uncertainties but also to the theoretical uncertainties. The renormalization and factorization scale variations, PDF uncertainties and the non-perturbative corrections contribute to theoretical uncertainties which are described below :

6.2.1 Scale Uncertainty

In perturbative QCD calculations of cross-sections, one has to choose a renormalization (μ_r) and factorization (μ_f) scale. The dependence on scales is negligible if these calculations are performed for all orders of the perturbative series. But the perturbative series is truncated at NLO, so there is a scale dependence of the measurement which is covered by systematic uncertainty known as scale uncertainty. The scale uncertainty is evaluated with the conventional recipe of varying the default scale $H_{T,2}/2$ chosen for μ_r and μ_f independently in the following six combinations: $(\mu_r/H_{T,2}/2, \mu_f/H_{T,2}/2) = (1/2, 1/2), (1/2, 1), (1, 1/2), (1, 2), (2, 1)$ and $(2, 2)$. The

maximal upwards and downwards deviations in cross-section from the central prediction give the scale uncertainty. To calculate the scale uncertainty for cross-section ratio R_{32} , first R_{32} is obtained for each above mentioned scale choice and then its difference from central R_{32} is taken. The scale uncertainty calculated using CT10-NLO PDF set ranges from 5% to 13% and 11% to 17% for inclusive 2-jet and 3-jet events cross-sections respectively, and from 6% to 8% for R_{32} .

6.2.2 PDF Uncertainty

The calculation of jet cross-sections in proton-proton collisions relies upon the knowledge of PDFs. These PDF sets are determined by global fits to all the available deep inelastic scattering (DIS) and related hard scattering data from different experiments. The various sources affect the PDFs such as theory model, input parameters like the strong coupling constant α_S , the quark masses and the statistical and systematic uncertainty sources of the data included in the PDF fit. These sources contribute to PDF uncertainty which is evaluated according to the prescriptions given for each PDF set. The CT10-NLO PDF set [107, 113] employ the eigenvector method to evaluate the PDF uncertainties. The CT10-PDF set consists of $N_{\text{ev}} = 26$ eigenvectors with two PDF members per eigenvector k , which are varied upwards and downwards to generate a set of eigenvector pairs. The asymmetric uncertainties, ΔX^+ and ΔX^- , of a quantity X are given by Eq. 6.4 where X_0 is the central prediction, X_k^+ and X_k^- are the predictions using the upwards and downwards variation of each eigenvector k .

$$\begin{aligned}\Delta X^+ &= \sqrt{\sum_{k=1}^{N_{\text{ev}}} [\max(X_k^+ - X^0, X_k^- - X^0, 0)]^2} \\ \Delta X^- &= \sqrt{\sum_{k=1}^{N_{\text{ev}}} [\min(X_k^+ - X^0, X_k^- - X^0, 0)]^2}\end{aligned}\quad (6.4)$$

The symmetric uncertainty (ΔX^\pm) is given by half the difference of the upwards and downwards variations :

$$\Delta X^\pm = \sqrt{\sum_{k=1}^{N_{\text{ev}}} \left[\frac{X_k^+ - X_k^-}{2} \right]^2} \quad (6.5)$$

The CT10-NLO PDF set uncertainties are downscaled by a factor of 1.64 in order to have the uncertainties at the 68.3% confidence level $\text{CL}(1\sigma)$ instead of 90% $\text{CL}(2\sigma)$ such that to have a uniform treatment with respect to other PDF sets. The PDF uncertainty as derived with the CT10-NLO PDF set is the dominant source of uncertainty and ranges from 3% to 30% for inclusive 2-jet and from 4% to 32% for 3-jet cross-sections. For R_{32} , the ratio of predictions for inclusive 3-jet to that of 2-jet is taken for each eigen vector with upwards and downwards variations separately and then PDF uncertainty is calculated as done for individual cross-sections. The PDF uncertainty ranges and from 2% to 10% for cross-section ratio R_{32} .

6.2.3 Non-perturbative Uncertainty

As discussed in [6.1.2](#), the differences in the non-perturbative (NP) corrections calculated from various Monte Carlo event generators introduce the NP uncertainty which is of the order of 1% and 1 to 2% for inclusive 2-jet and 3-jet event cross-sections respectively, and < 1% for cross-section ratio R_{32} .

6.2.4 Total Theoretical Uncertainty

The total systematic theoretical uncertainties are obtained as the quadratic sum of the scale, PDF and NP uncertainties. Figure [6.5](#) presents the systematic theoretical uncertainties affecting the cross-section measurement for inclusive 2-jet (top left) and 3-jet events (top right) and the cross-section ratio R_{32} (bottom), using CT10-

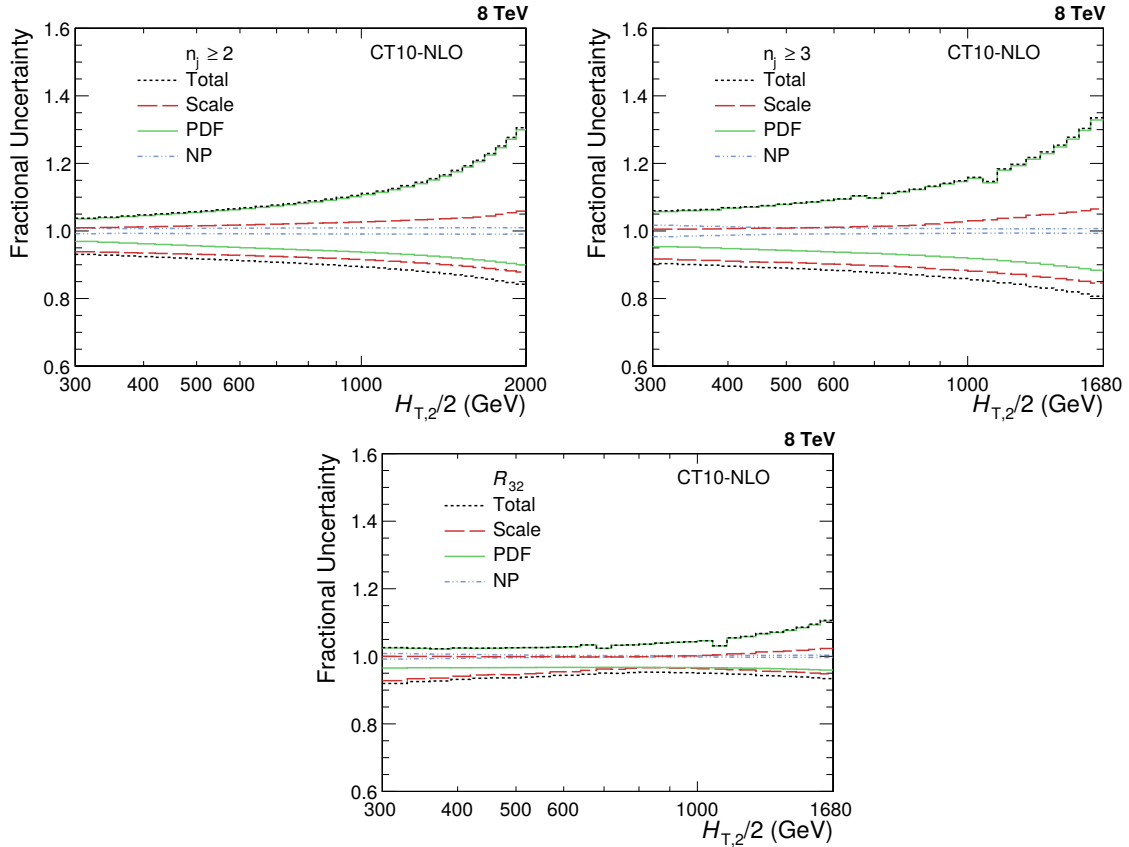


Figure 6.5: The systematic theoretical uncertainties affecting the cross-section measurement for inclusive 2-jet (top left) and 3-jet events (top right) and their ratio R_{32} (bottom). The scale (red dashed line), PDF (green line) and NP (blue dashed line) uncertainties as well as total uncertainty (black dashed line) obtained using CT10-NLO PDF set are shown. The total theoretical uncertainty is asymmetric and is dominated by PDF uncertainty.

NLO PDF set. The scale (red dashed line), PDF (green line) and NP (blue dashed line) uncertainties as well as total theoretical uncertainty (black dashed line) are shown. The total theoretical uncertainty is asymmetric and is dominated by PDF uncertainty which grows in magnitude with increasing value of $H_{T,2}/2$. Table 6.2 quotes the values of the theoretical uncertainty from each source as well as total uncertainty affecting the measurements. The bin-wise values of uncertainties (in %) from each source as well as total uncertainty are shown in Tables A.5, A.6 and A.7 for $n_j \geq 2$ and $n_j \geq 3$ event cross-sections and cross-section ratio R_{32} , respectively. The computation of the NLO predictions with NLOJET++ is also

subject to statistical fluctuations from the complex numerical integrations. For the inclusive 2-jet event cross-sections this uncertainty is smaller than about a per mille, while for the inclusive 3-jet event cross-section it amounts to 1-9 per mille. Hence the statistical uncertainty is not considered in the total theoretical uncertainty. The small dips at ~ 700 and 1000 GeV in the PDF uncertainty for inclusive 3-jet events cross-sections and cross-section ratio R_{32} is a feature of the CT10-NLO PDF set.

Table 6.2: Overview of all systematic theoretical uncertainties, obtained using CT10-NLO PDF set, affecting the measurement of cross-sections for inclusive 2-jet (left) and 3-jet events (middle) and cross-section ratio R_{32} (right).

Uncertainty Source	Inclusive 2-jet	Inclusive 3-jet	R_{32}
Scale	5 to 13%	11 to 17%	6 to 8%
PDF	3 to 30%	4 to 32%	2 to 10%
Non-perturbative (NP)	1%	1 to 2%	< 1%
Total	3 to 30%	5 to 34%	3 to 11%

6.3 Comparison of Theory to Data

After correcting the measurement for detector effects as well as NLO pQCD calculations for non-perturbative (NP) and electroweak (EW) effects, it is now feasible to compare the measured cross-sections with the theory predictions. Figure 6.6 shows the measured differential inclusive 2-jet and 3-jet event cross-sections as a function of $H_{T,2}/2$ after unfolding for detector effects. On the left, the measurements (points) are compared to the NLOJET++ predictions using the CT10-NLO PDF set (line), corrected for NP effects and in addition for EW effects in the 2-jet case. On the right, the comparison is made to the predictions from MADGRAPH5+PYTHIA6 (MG+P6) with tune Z2* (line), corrected for EW effects in the 2-jet case. The error bars give the total experimental uncertainty, given by the quadrature sum of the statistical and systematic uncertainties. On a logarithmic scale, the data are in well agreement with the NLO predictions over the whole range of $H_{T,2}/2$ from 300 GeV up to 2000

(2-jet) and 1680 GeV (3-jet) respectively.

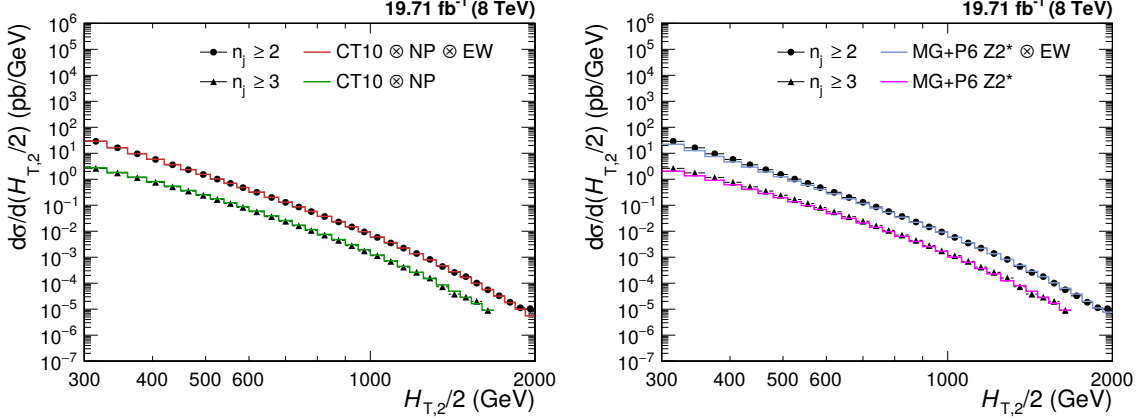


Figure 6.6: Comparison of the measured differential inclusive 2-jet and 3-jet event cross-sections as a function of $H_{T,2}/2$ to theoretical predictions. On the left, the data (points) are shown together with NLOJET++ predictions (line) using the CT10-NLO PDF set, corrected for non-perturbative (NP) and electroweak (EW) effects (2-jet) or only NP effects (3-jet). On the (right), the data (points) are compared to predictions from MADGRAPH5+PYTHIA6 (MG+P6) with tune $Z2^*$ (line), corrected for EW effects in the 2-jet case. The error bars give the total experimental uncertainty, given by the quadrature sum of the statistical and systematic uncertainties.

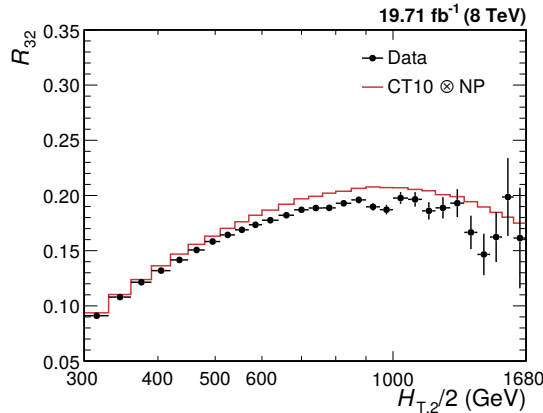


Figure 6.7: Cross-section ratio R_{32} as a function of $H_{T,2}/2$ calculated from data (solid circles) in comparison to that from NLO pQCD predictions obtained using the CT10-NLO PDF set corrected with non-perturbative (NP) corrections (line). The error bars correspond to the total experimental uncertainty derived as quadratic sum from all uncertainty sources.

Figure 6.7 shows the cross-section ratio R_{32} obtained from unfolded data data (solid circles) in comparison to that from NLO pQCD predictions obtained using the CT10-NLO PDF set corrected with NP corrections (line). The error bars here

represents the total experimental uncertainty derived as quadratic sum from all uncertainty sources. The deviations of measured R_{32} from the theoretical predicted value can be explained by the electroweak effects which are not considered yet because of their unavailability for inclusive 3-jet event cross-sections.

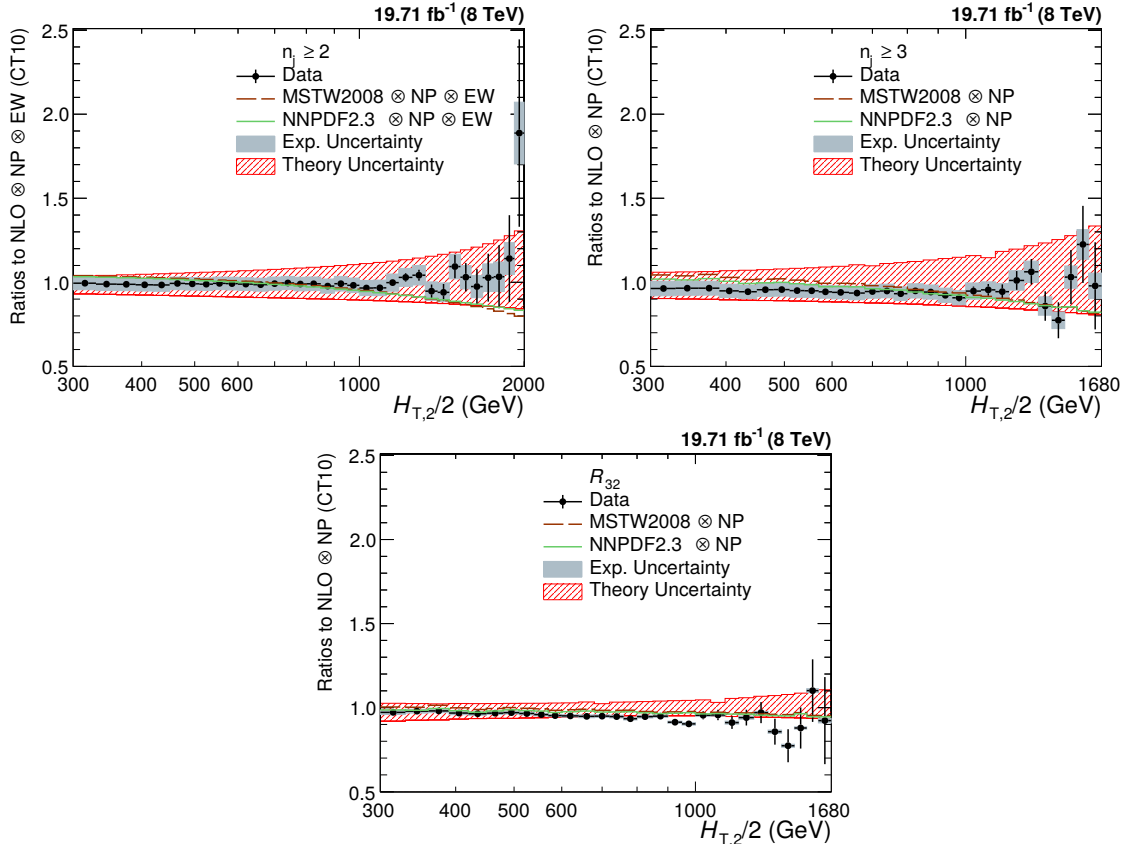


Figure 6.8: Ratio of data over theory using the CT10-NLO PDF set for inclusive 2-jet (top left) and 3-jet event cross-sections (top right) and their ratio R_{32} (bottom). The theory predictions are corrected for non-perturbative effects (NP) and also for electroweak effects (EW) for inclusive 2-jet only. For comparison predictions employing two other PDF sets, MSTW2008 and NNPDF2.3, are also shown. The error bars represents the statistical uncertainty of the data and the shaded rectangles represents the total experimental systematic uncertainty. The shaded band around unity indicate the total uncertainty of the theory.

For better visibility, the ratios of data over the theory at NLO are also studied in details. In Fig. 6.8, the ratios of data over NLOJET++ predictions using the CT10-NLO PDF set are shown for inclusive 2-jet (top left) and 3-jet event cross-sections (top right) as well as their ratio R_{32} (bottom). The data are well described by the predictions within their uncertainty, which is dominated at large $H_{T,2}/2$ by

PDF effects in the upwards and by scale variations in the downwards direction. A trend towards an increasing systematic excess of the 2-jet data with respect to theory, starting at about 1 TeV in $H_{T,2}/2$, is remedied by the inclusion of EWK corrections. In the 3-jet case the statistical precision of the data and the reach in $H_{T,2}/2$ is insufficient to observe any effect. The alternative PDF sets MSTW2008 and NNPDF2.3 exhibit a small underestimation of the cross-sections at high $H_{T,2}/2$.

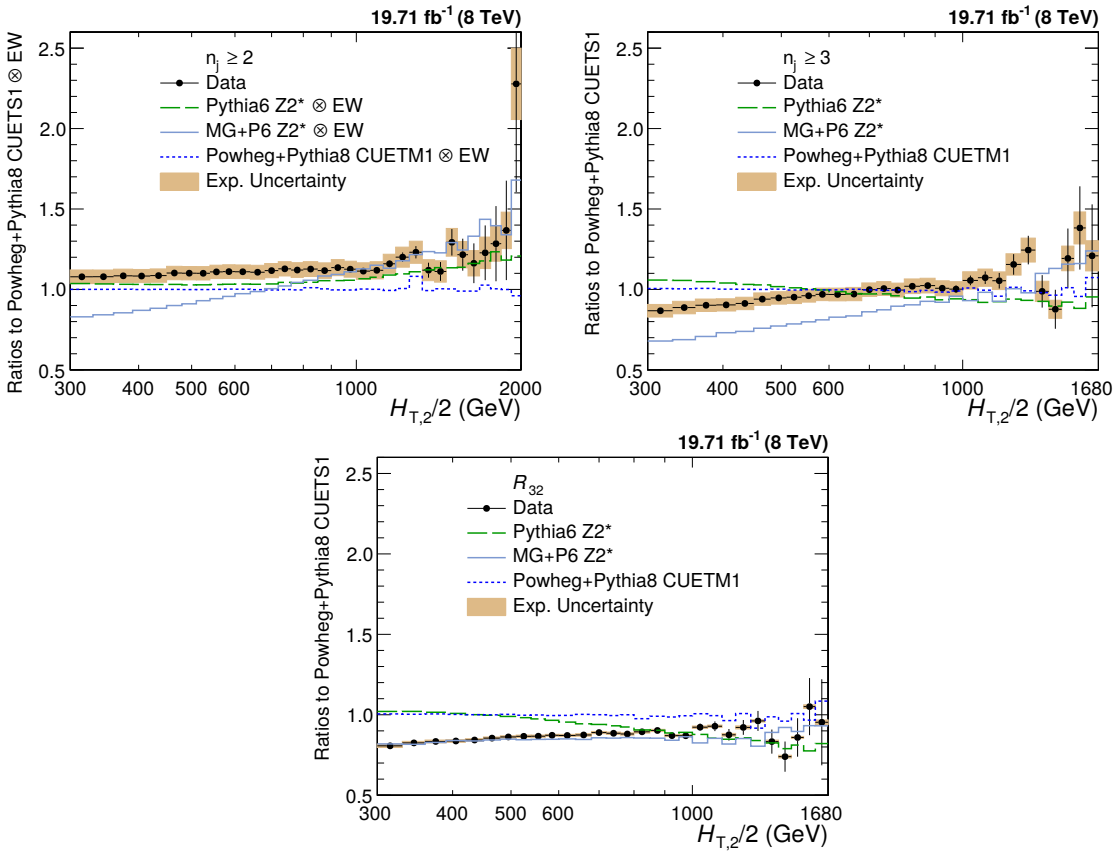


Figure 6.9: Ratio of data over the predictions from POWHEG+PYTHIA8 with tune CUETS1 are presented for inclusive 2-jet (top left) and 3-jet event cross-sections (top right) as well as their ratio R_{32} (bottom). For comparison the alternative tune CUETM1 of POWHEG+PYTHIA8, the tree-level multi-leg improved prediction by MADGRAPH5+PYTHIA6 with tune $Z2^*$, and the LO MC predictions from PYTHIA6 tune $Z2^*$ are shown as well. The error bars correspond to the statistical uncertainty of the data and the shaded rectangles to the total experimental systematic uncertainty. EW corrections have been accounted for in this comparison in the 2-jet case only.

The POWHEG framework providing a NLO dijet calculation matched to the parton showers of PYTHIA8 employed with the CUETS1 and CUETM1 tunes [73] is also

used for a comparison. The ratios of data over theory from POWHEG+PYTHIA8 with tune CUETS1 are shown for inclusive 2-jet (top left) and 3-jet event cross-sections (top right) as well as their ratio R_{32} (bottom) in Fig. 6.9. For comparison, the LO prediction from PYTHIA6 with tune Z2*, the tree-level multi-leg improved prediction by MADGRAPH5+PYTHIA6 with tune Z2*, and the matched NLO prediction from POWHEG+PYTHIA8 with tune CUETM1 are shown as well. EW corrections have been accounted for in this comparison in the 2-jet case only. Significant discrepancies, which are cancelled to a large extent in the ratio R_{32} , are visible in the comparison with the LO prediction from MADGRAPH5+PYTHIA6 with tune Z2*, in particular for small $H_{T,2}/2$. In contrast, the employed dijet MC POWHEG+PYTHIA8 better describe the 2-jet event cross-section, but fail for the 3-jet case.

The jet measurements at hadron colliders can be used to extract the strong coupling constant α_S , which is discussed in the next chapter.

Chapter 7

Determination of the Strong Coupling Constant

The inclusive jet production cross-section at hadron colliders mainly depends on the strong coupling constant α_S for a given center-of-mass energy. Hence the measurements of the inclusive jet cross-section and jet properties provide a direct probe to measure the strong coupling constant. The measurement of α_S has been already done by various experiments such as CMS [1, 91, 105, 114, 115], ATLAS [116], D0 [117, 118], H1 [119, 120], and ZEUS [121]. In this thesis, the measurements of differential inclusive 2-jet and 3-jet event cross-sections as well as the cross-section ratio R_{32} , as a function of $H_{\text{T},2}/2$ are used to extract the value of the strong coupling constant at the scale of the Z boson mass $\alpha_s(M_Z)$. The differential inclusive jet production cross-section up to at NLO is given by [122] :

$$\frac{d\sigma}{d(H_{\text{T},2}/2)} = \alpha_S^2(\mu_r) \hat{X}^{(0)}(\mu_f, H_{\text{T},2}/2) [1 + \alpha_S(\mu_r) K_1(\mu_r, \mu_f, H_{\text{T},2}/2)] \quad (7.1)$$

where $\frac{d\sigma}{d(H_{\text{T},2}/2)}$ is the differential inclusive jet production cross-section as a function of $H_{\text{T},2}/2$, μ_r and μ_f are the renormalization and factorization scales set equal to $H_{\text{T},2}/2$, $\alpha_S^2(\mu_r) \hat{X}^{(0)}(\mu_f, H_{\text{T},2}/2)$ is the leading order

(LO) contribution to the differential inclusive jet production cross-section and $\alpha_S^3(\mu_r)\hat{X}^{(0)}(\mu_f, H_{T,2}/2)K1(\mu_r, \mu_f, H_{T,2}/2)$ is the next-to-leading order (NLO) contribution. Equation 7.1 shows how the inclusive jet production cross-section varies with $\alpha_S(\mu_r)$.

7.1 Sensitivity of Measurements to $\alpha_s(M_Z)$

For a fixed choice of μ_r and μ_f , different input values of $\alpha_s(M_Z)$ to a PDF set will lead to different theory predictions of the differential cross-section distribution. This will give an estimate of the sensitivity of the theory predictions to the varying input value of $\alpha_s(M_Z)$. A comparison of the measured spectrum with the theory predictions obtained using all $\alpha_s(M_Z)$ inputs will give a hint of the input value of $\alpha_s(M_Z)$ for which the theory distribution has the closest matching with data. In this section, the sensitivity of the inclusive differential jet event cross-sections and cross-section ratio, R_{32} to varying input values of $\alpha_s(M_Z)$ for different PDF sets is demonstrated by plotting the ratios of data over theory predictions with central value of $\alpha_s(M_Z)$.

Figures 7.1, 7.2 and 7.3 present the ratio of data to the theory predictions, corrected for NP effects, for all variations in $\alpha_s(M_Z)$ available for the PDF sets CT10, CT14, MSTW2008, MMHT2014 and NNPDF2.3 at NLO evolution order as specified in Table 6.1, for inclusive 2-jet event cross-sections, inclusive 3-jet events cross-sections and ratio R_{32} respectively. The $\alpha_s(M_Z)$ value is varied in the range 0.112-0.127, 0.111-123, 0.110-0.130, 0.108-0.128 and 0.114-0.124 in steps of 0.001 for the CT10, CT14, MSTW2008, MMHT2014 and NNPDF2.3PDF sets, respectively. The error bars correspond to the total experimental uncertainty derived as quadratic sum from all uncertainty sources. The theory predictions are also corrected for EW effects for inclusive 2-jet events cross-section. A small slope increasing with $H_{T,2}/2$ is visible for most PDFs in both cross-sections. This effect is largely cancelled in

the cross-section ratio. R_{32} exhibits a flat behaviour with respect to the predictions for all five PDF sets in the whole range of $H_{T,2}/2$ up to 1680 GeV. Therefore, these data can be used to determine the strong coupling constant, although only up to 1 TeV for the cross-sections as long as electroweak corrections are not taken into account.

Moreover, the different sensitivity to $\alpha_s(M_Z)$ caused by the leading power in α_S in the expansion of the 2-jet inclusive ($\propto \alpha_S^2$) and the 3-jet inclusive cross-section ($\propto \alpha_S^3$), and their ratio ($\propto \alpha_S^1$) is clearly visible from the spread between the calculations for the smallest and largest value of $\alpha_s(M_Z)$ within the same PDF set when passing through Figures 7.1–7.3. This also demonstrates the potential of ratios R_{mn} with $m-n > 1$.

7.2 Determination of $\alpha_s(M_Z)$

As discussed in the previous section, the measured inclusive 2-jet and 3-jet event cross-sections and their ratio R_{32} can be used for a determination of the strong coupling constant $\alpha_s(M_Z)$. To extract the value of $\alpha_s(M_Z)$, a general fit procedure [1, 91, 115] has been followed and is described in the following section.

7.2.1 Fitting Procedure

The value of $\alpha_s(M_Z)$ is determined by minimizing the chi-square (χ^2) between the experimental measurements and the theoretical predictions. The χ^2 is given by the following equation :

$$\chi^2 = M^T C^{-1} M \quad (7.2)$$

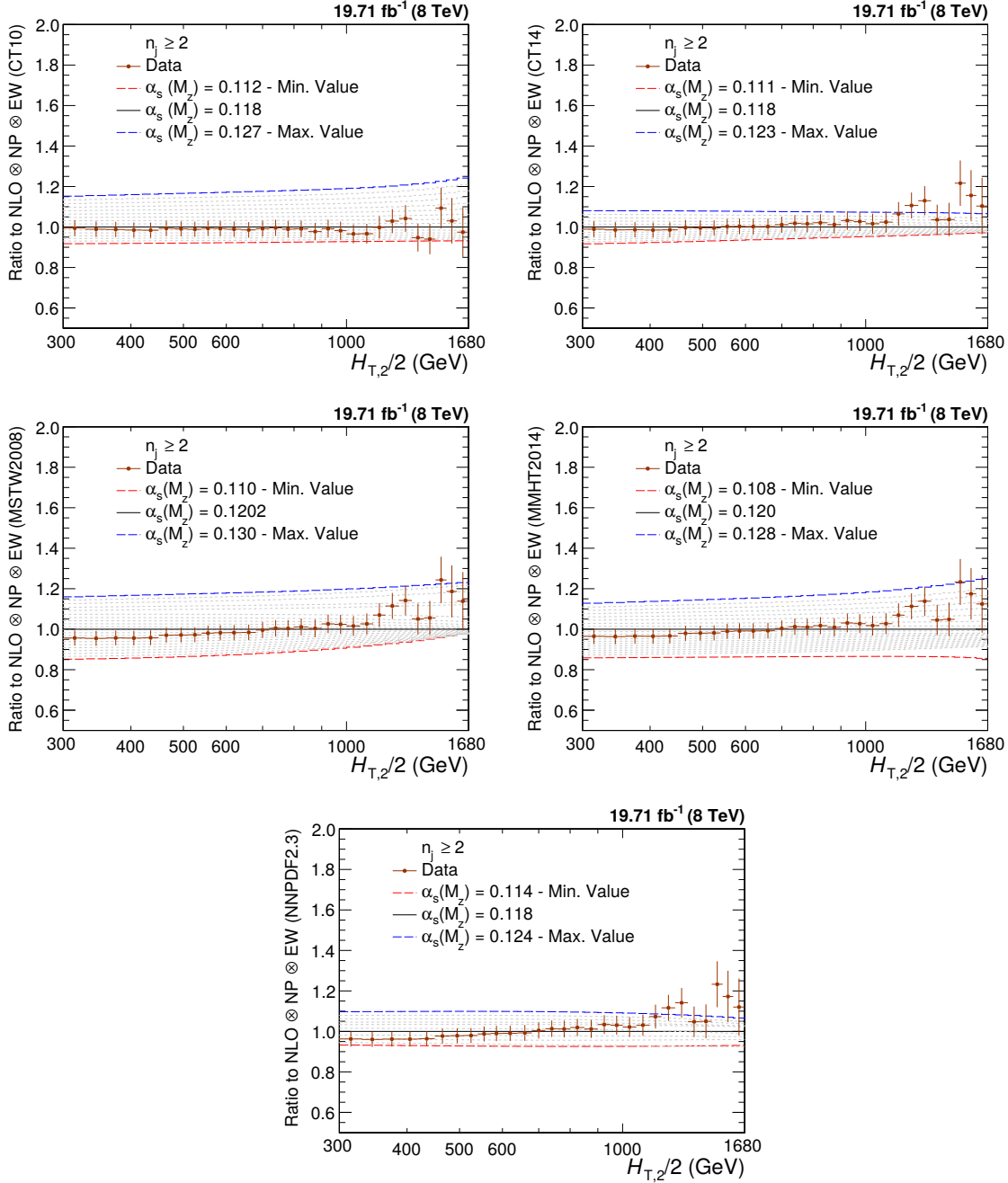


Figure 7.1: Ratio of the measured inclusive 2-jet differential cross-section to theory predictions using the CT10 (top left), the CT14 (top right), the MSTW2008 (middle left), the MMHT2014 (middle right) and NNPDF2.3 (bottom) NLO PDF sets for a series of values of $\alpha_s(M_Z)$. The $\alpha_s(M_Z)$ value is varied in the range 0.112-0.127, 0.111-0.123, 0.110-0.130, 0.108-0.128 and 0.114-0.124 in steps of 0.001 for the CT10, CT14, MSTW2008, MMHT2014 and NNPDF2.3 NLO PDF sets, respectively. The error bars correspond to the total experimental uncertainty. The theory predictions are corrected for non-perturbative (NP) and electroweak (EW) effects.

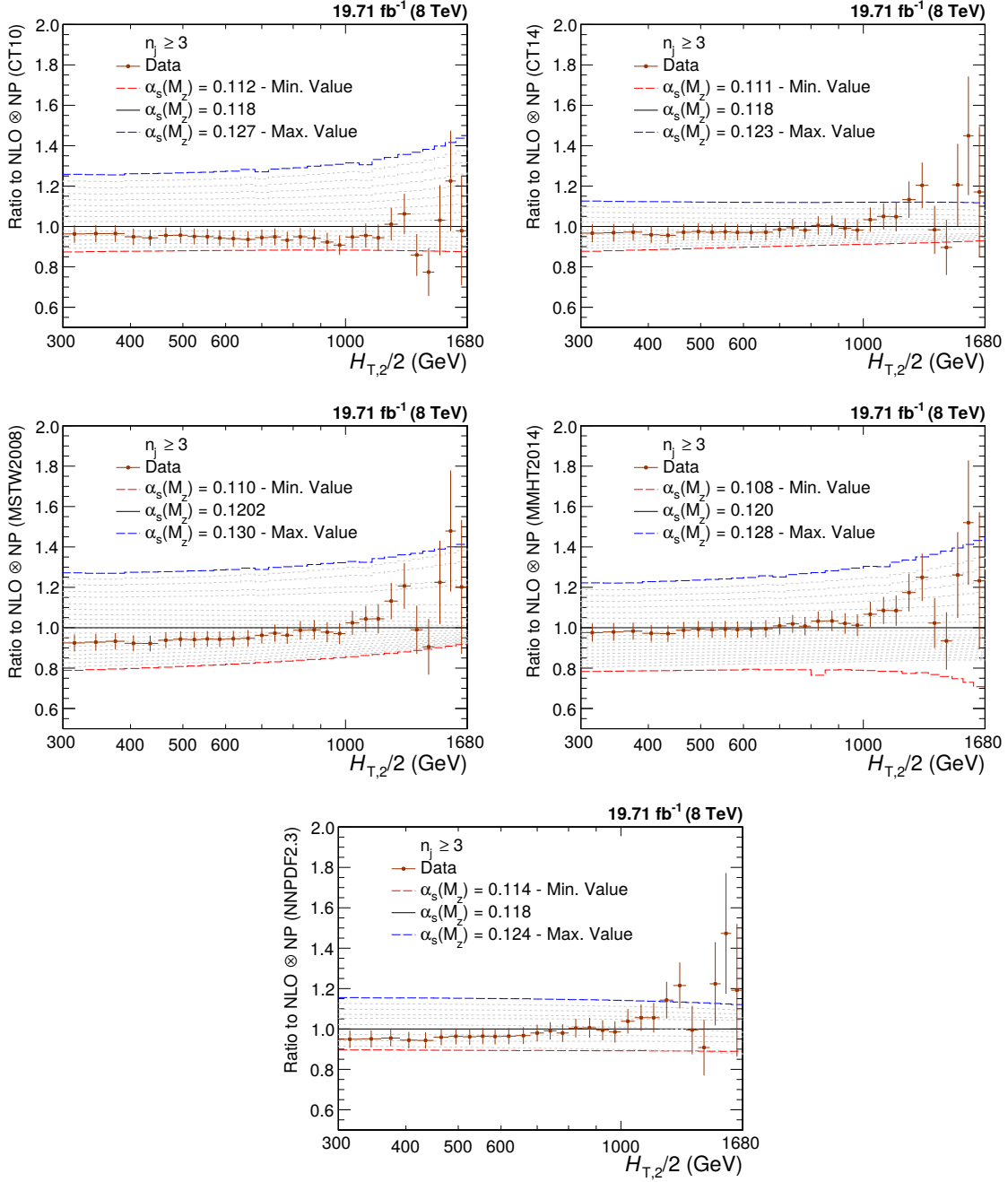


Figure 7.2: Ratio of the measured inclusive 3-jet differential cross-section to theory predictions using the CT10 (top left), the CT14 (top right), the MSTW2008 (middle left), the MMHT2014 (middle right) and NNPDF2.3 (bottom) NLO PDF sets for a series of values of $\alpha_s(M_Z)$. The $\alpha_s(M_Z)$ value is varied in the range 0.112-0.127, 0.111-0.123, 0.110-0.130, 0.108-0.128 and 0.114-0.124 in steps of 0.001 for the CT10, CT14, MSTW2008, MMHT2014 and NNPDF2.3 NLO PDF sets, respectively. The error bars correspond to the total experimental uncertainty. The theory predictions are corrected for non-perturbative (NP) effects.

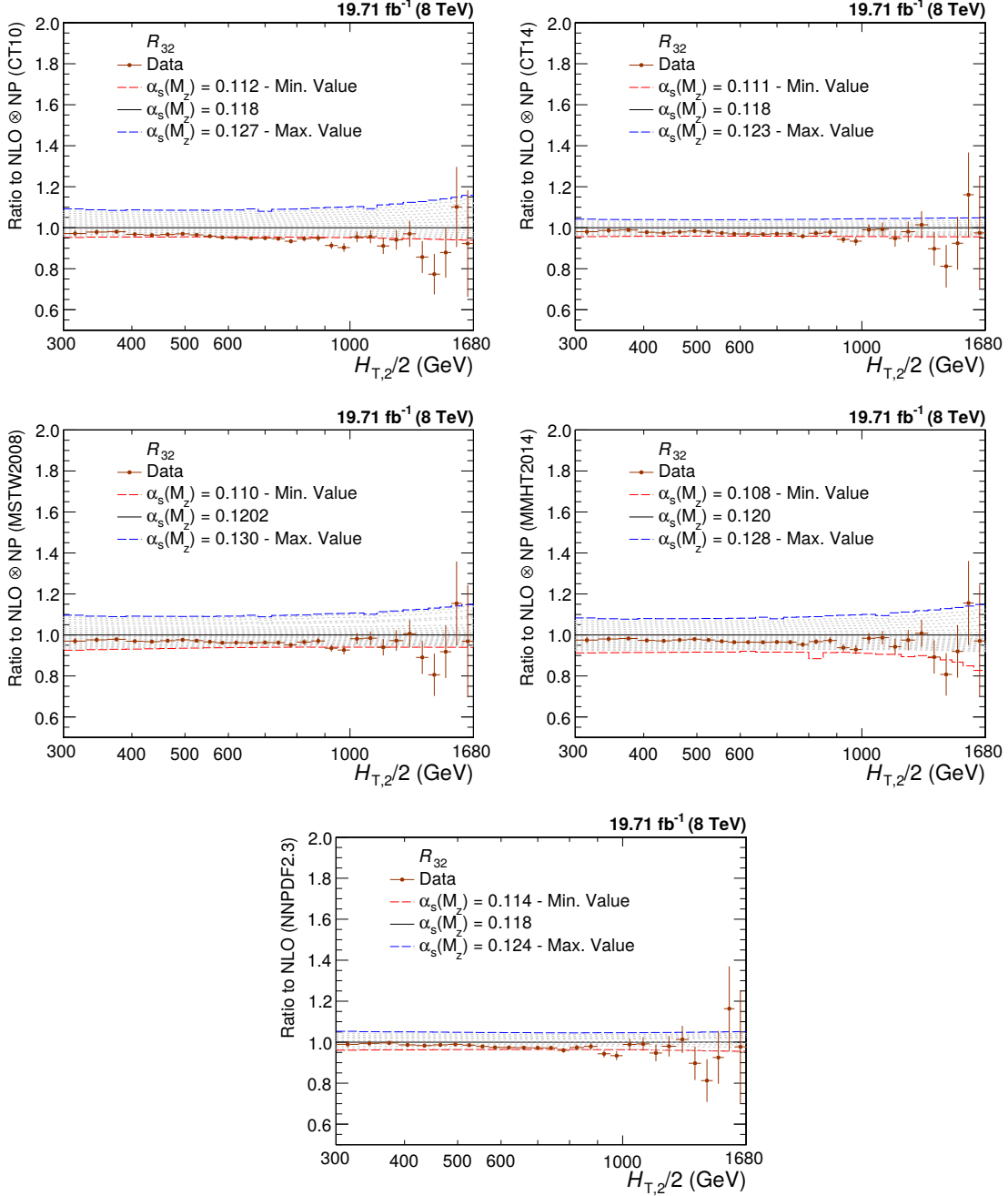


Figure 7.3: Ratio of the measured cross-section ratio, R_{32} to theory predictions using the CT10 (top left), the CT14 (top right), the MSTW2008 (middle left), the MMHT2014 (middle right) and NNPDF2.3 (bottom) NLO PDF sets for a series of values of $\alpha_s(M_Z)$. The $\alpha_s(M_Z)$ value is varied in the range 0.112-0.127, 0.111-0.123, 0.110-0.130, 0.108-0.128 and 0.114-0.124 in steps of 0.001 for the CT10, CT14, MSTW2008, MMHT2014 and NNPDF2.3 NLO PDF sets, respectively. The error bars correspond to the total experimental uncertainty. The theory predictions are corrected for non-perturbative (NP) effects.

where M is the vector of the differences between the data (D^i) and the theoretical values (T^i) in each bin i ,

$$M^i = D^i - T^i \quad (7.3)$$

and C is the covariance matrix including all experimental uncertainties as described in Sec. 5.6 and some theoretical uncertainties discussed in Sec. 6.2. The covariance matrix $C = C_{\text{exp}} + C_{\text{theo}}$ is defined as the sum of covariances of experimental and theoretical sources of uncertainty as follows :

$$C_{\text{exp}} = \text{Cov}^{\text{ExpStat}} + \sum \text{Cov}^{\text{JEC}} + \text{Cov}^{\text{Unfolding}} + \text{Cov}^{\text{Lumi}} + \text{Cov}^{\text{Residual}} \quad (7.4)$$

$$C_{\text{theo}} = \text{Cov}^{\text{TheoStat}} + \text{Cov}^{\text{NP}} + \text{Cov}^{\text{PDF}} \quad (7.5)$$

where the labelled covariance matrices account for the following effects:

- $\text{Cov}^{\text{ExpStat}}$: statistical uncertainty of the data including correlations introduced by the unfolding
- Cov^{JEC} : the jet energy corrections (JEC) systematic uncertainty
- $\text{Cov}^{\text{Unfolding}}$: the unfolding systematic uncertainty including the resolution (JER) and model dependence
- Cov^{Lumi} : the luminosity uncertainty
- $\text{Cov}^{\text{Residual}}$: a residual uncorrelated systematic uncertainty summarizing individual causes such as small trigger and identification inefficiencies, time dependence of the jet p_T resolution, and uncertainty on the trigger prescale factors
- $\text{Cov}^{\text{TheoStat}}$: statistical uncertainty caused by numerical integrations in the cross-section computations

- Cov^{NP} : the systematic uncertainty of the non-perturbative (NP) corrections
- Cov^{PDF} : the PDF uncertainties

While taking the differences between theory and data, the treatment of experimental and theoretical systematic uncertainties is crucial. The Unfolding, JEC, Lumi and PDF and NP systematic uncertainties are treated as 100% correlated among $H_{\text{T},2}/2$ bins. If δ_i is the total uncertainty on the differential cross-section, for the i -th $H_{\text{T},2}/2$ bin, for any of these fully correlated sources, then the i, j -th element of the corresponding covariance matrix is given by $\text{COV}_{ij} = \delta_i \times \delta_j$. The JEC, unfolding, and luminosity uncertainties are treated as multiplicative to avoid the statistical bias that arises when estimating uncertainties from data. In fits of the ratio R_{32} , the luminosity and residual uncorrelated uncertainties cancel completely. Partial cancellations between the other sources of uncertainty are taken into account in the fit.

The evaluation of PDF uncertainty depends on the individual PDF set as already discussed in Sec. 6.2.2. The PDF covariance matrix construction varies among different PDF sets. The CT10, CT14, MMHT2014 and MSTW2008 NLO PDF sets employ the eigenvector method to evaluate the PDF uncertainties as explained in Sec. 6.2.2. The number of eigenvectors (N_{ev}) with two PDF members per eigenvector for CT10, CT14, MMHT2014 and MSTW2008 NLO PDF sets are 26, 28, 25 and 20, respectively. The NNPDF2.3 PDF set comes with hundred different replicas (N_{rep}) instead of different eigenvectors, as for CT10 or CT14 PDF sets. The mean uncertainty is calculated as average uncertainty from 100 different replicas. Following the prescription given in [123], the PDF uncertainty is calculated as :

$$(\Delta X)^2 = \frac{1}{N_{\text{rep}} - 1} \sum_{k=1}^{N_{\text{rep}}} [X_k - \langle X_k \rangle]^2 \quad (7.6)$$

where ΔX is the uncertainty on predicted differential cross-section, X_k is the differ-

ential cross-section for k -th replica and $\langle X_k \rangle$ is the average differential cross-section from all the replicas.

Scale uncertainties of the pQCD predictions are taken into account by employing the offset method, i.e. by performing separate fits with varying scale factors as described in the Sec. 6.2.1. The largest upwards and downwards deviations from the default factors are defined as the uncertainty. At NLO such scale variations predominantly lead to smaller cross-sections and also a smaller ratio R_{32} as visible in Fig. 6.5. As a consequence the scale uncertainty in fits is equally asymmetric, where smaller cross-sections or ratios are compensated by an increase in the fitted value for $\alpha_s(M_Z)$.

7.2.2 Fit Results

To determine the value of the strong coupling constant at the scale of the Z boson mass $\alpha_s(M_Z)$, fits to the differential inclusive 2-jet and 3-jet events cross-sections are performed using five different NLO PDF sets : CT10, CT14, MSTW2008, MMHT2014 and NNPDF2.3. The range in $H_{T,2}/2$ is restricted to be between 300 GeV and 1 TeV to avoid the region close to the minimal p_T threshold of 150 GeV for each jet at low p_T and the onset of electroweak effects at high $H_{T,2}/2$, which are available for the dijet case only. The $\alpha_s(M_Z)$ results obtained from a simultaneous fit to all 19 $H_{T,2}/2$ bins in the above mentioned range are reported in Table 7.1. For comparison, a simultaneous fit to both cross-sections ignoring any correlations, and a fit to the cross-section ratio R_{32} , fully accounting for correlations is also performed and the results are tabulated in Table 7.2. The electroweak effects are assumed to cancel in the ratio as do the luminosity and the uncorrelated uncertainty.

All cross-section fits give compatible values for $\alpha_s(M_Z)$ in the range of 0.115–0.118 whereas for the ratio R_{32} somewhat smaller values are obtained. But for individual cross-sections, χ^2/n_{dof} values are small as compared to the cross-section

ratio R_{32} . A possible explanation is an overestimation of the residual uncorrelated uncertainty of 1% that is cancelled for R_{32} . If the fits are repeated with an assumed uncertainty of 0.25% instead, the χ^2/n_{dof} values lie around unity while the $\alpha_s(M_Z)$ values are still compatible with the previous results but with slightly reduced uncertainties.

Table 7.1: Determination of $\alpha_s(M_Z)$ from the inclusive 2-jet and 3-jet event cross-sections using five PDF sets at NLO. Only total uncertainties without scale variations are quoted. The results are obtained from a simultaneous fit to all 19 $H_{\text{T},2}/2$ bins in the restricted range of $0.3 < H_{\text{T},2}/2 < 1.0$ TeV.

PDF set	Inclusive 2-jets			Inclusive 3-jets		
	$\alpha_s(M_Z)$	$\pm \Delta \alpha_s(M_Z)$	χ^2/n_{dof}	$\alpha_s(M_Z)$	$\pm \Delta \alpha_s(M_Z)$	χ^2/n_{dof}
CT10	0.1174	0.0032	3.0/18	0.1169	0.0027	5.4/18
CT14	0.1160	0.0035	3.5/18	0.1159	0.0031	6.1/18
MSTW2008	0.1159	0.0025	5.3/18	0.1161	0.0021	6.7/18
MMHT2014	0.1165	0.0034	5.9/18	0.1166	0.0025	7.1/18
NNPDF2.3	0.1183	0.0025	9.7/18	0.1179	0.0021	9.1/18

Table 7.2: Determination of $\alpha_s(M_Z)$ from the inclusive 2-jet and 3-jet event cross-sections simultaneously and from their ratio R_{32} using five PDF sets at NLO. Only total uncertainties without scale variations are quoted. The results are obtained from a simultaneous fit to all 38 (left) and 19 (right) $H_{\text{T},2}/2$ bins in the restricted range of $0.3 < H_{\text{T},2}/2 < 1.0$ TeV. For comparison, correlations between the two cross-sections are neglected in the simultaneous fit on the left, but fully taken into account in the ratio fit on the right.

PDF set	Inclusive 2- and 3-jets			R_{32}		
	$\alpha_s(M_Z)$	$\pm \Delta \alpha_s(M_Z)$	χ^2/n_{dof}	$\alpha_s(M_Z)$	$\pm \Delta \alpha_s(M_Z)$	χ^2/n_{dof}
CT10	0.1170	0.0026	8.2/37	0.1141	0.0028	19./18
CT14	0.1161	0.0029	9.1/37	0.1139	0.0032	15./18
MSTW2008	0.1161	0.0021	11./37	0.1150	0.0023	21./18
MMHT2014	0.1168	0.0025	11./37	0.1142	0.0022	19./18
NNPDF2.3	0.1188	0.0019	15./37	0.1184	0.0021	12./18

To investigate how the electroweak (EW) corrections affect the fit results for $\alpha_s(M_Z)$, the range in $H_{\text{T},2}/2$ is extended to $0.3 < H_{\text{T},2}/2 < 1.68$ TeV. $\alpha_s(M_Z)$ values are obtained from fits to the inclusive 2-jet event cross-section in this range with or without EW correction factors and the results are presented in Table 7.3. The largest impact is a reduction in χ^2/n_{dof} , which indicates a better agreement when

EW effects are included. In addition, a tendency to slightly smaller $\alpha_s(M_Z)$ values is observed without the EW corrections. For the ratio R_{32} , it is expected that these effects are much reduced.

Table 7.3: Determination of $\alpha_s(M_Z)$ from the inclusive 2-jet event cross-section using five PDF sets at NLO without (left) and with (right) electroweak (EW) corrections. Only total uncertainties without scale variations are quoted. The results are obtained from a simultaneous fit to all 29 $H_{T,2}/2$ bins in the range of $0.3 < H_{T,2}/2 < 1.68$ TeV.

PDF set	without EW			with EW		
	$\alpha_s(M_Z)$	$\pm \Delta\alpha_s(M_Z)$	χ^2/n_{dof}	$\alpha_s(M_Z)$	$\pm \Delta\alpha_s(M_Z)$	χ^2/n_{dof}
CT10	0.1163	0.0034	15./28	0.1165	0.0032	14./28
CT14	0.1137	0.0033	24./28	0.1144	0.0033	17./28
MSTW2008	0.1093	0.0028	27./28	0.1133	0.0023	19./28
MMHT2014	0.1127	0.0032	32./28	0.1141	0.0032	21./28
NNPDF2.3	0.1162	0.0024	31./28	0.1168	0.0024	23./28

From Fig. 7.3 follows that only the PDF sets MSTW2008 and MMHT2014 provide a large enough range in $\alpha_s(M_Z)$ values to ensure fits without extrapolation. The other three PDF sets are at the limit such that reliable fits cannot be performed for all scale settings and/or bins in scale $Q = H_{T,2}/2$. Since many systematic uncertainties cancel completely or partially in the cross-section ratio R_{32} as compared to the individual cross-sections, R_{32} is used mainly to determine the value of $\alpha_s(M_Z)$. Table 7.4 give the complete results for MSTW2008 and MMHT2014 for the full range in $H_{T,2}/2$ of 300 GeV up to 1.68 TeV along with the corresponding components of PDF, scale, NP and total experimental except scale uncertainties are shown. In contrast to fits at NLO using cross-sections where the scale uncertainty recipe usually leads to a very asymmetric behaviour with larger downward uncertainties in the case, this is inverted for the fits to the cross-section ratio R_{32} . The scale uncertainty is the most dominant source of total uncertainty on $\alpha_s(M_Z)$. These values are determined with the central renormalization and factorization scales i.e. $\mu_r = \mu_f = H_{T,2}/2$. The values are also determined for the six scale factor combinations for the two PDF sets MSTW2008 and MMHT2014 and results are shown in Table 7.5.

The uncertainty decomposition for $\alpha_s(M_Z)$ determined from cross-section ratio R_{32} is performed in four sub-ranges of $H_{T,2}/2$ and the results are shown in Table 7.6. The statistical uncertainty of the NLO computation is negligible in comparison to any of the other sources of uncertainty. Electroweak corrections, significant only at high $H_{T,2}/2$, are assumed to cancel between the numerator and denominator.

Using the MSTW2008 PDF set, which dates from before the LHC start, the strong coupling constant finally is determined to

$$\begin{aligned} \alpha_s(M_Z) &= 0.1150 \pm 0.0010 \text{ (exp)} \pm 0.0013 \text{ (PDF)} \pm 0.0015 \text{ (NP)} {}^{+0.0050}_{-0.0000} \text{ (scale)} \\ &= 0.1150 \pm 0.0023 \text{ (all except scale)} {}^{+0.0050}_{-0.0000} \text{ (scale)} \end{aligned} \quad (7.7)$$

The MMHT2014 PDF set, although using LHC jet data to determine the PDF parameters, leads to a very similar result of

$$\begin{aligned} \alpha_s(M_Z) &= 0.1142 \pm 0.0010 \text{ (exp)} \pm 0.0013 \text{ (PDF)} \pm 0.0014 \text{ (NP)} {}^{+0.0049}_{-0.0006} \text{ (scale)} \\ &= 0.1142 \pm 0.0022 \text{ (all except scale)} {}^{+0.0049}_{-0.0006} \text{ (scale)} \end{aligned} \quad (7.8)$$

7.3 Running of the Strong Coupling Constant

The value of the strong coupling constant α_S depends on the energy scale Q and it decreases with the increase of scale Q . To study this dependence, the determination of α_S is carried out at different energies. The procedure to extract $\alpha_S(Q)$ is same as the one followed for the $\alpha_s(M_Z)$. To have different energy scales, the fitted $H_{T,2}/2$ range 300 - 1680 GeV is divided into four different sub-ranges as shown by the first column in Table 7.7. Each of the $H_{T,2}/2$ range is associated with a scale Q , which

Table 7.4: Determination of $\alpha_s(M_Z)$ from the ratio R_{32} using the two most compatible PDF sets MSTW2008 and MMHT2014 at NLO along with the corresponding components of PDF, scale, NP and total (except scale) experimental uncertainties. The results are obtained from a simultaneous fit to all 29 $H_{T,2}/2$ bins in the full range of $0.3 < H_{T,2}/2 < 1.68$ TeV.

PDF set	$\alpha_s(M_Z)$	exp	PDF	NP	all exc.	scale	χ^2/n_{dof}
MSTW2008	0.1150	± 0.0010	± 0.0013	± 0.0015	± 0.0023	$^{+0.0050}_{-0.0000}$	26./28
MMHT2014	0.1142	± 0.0010	± 0.0013	± 0.0014	± 0.0022	$^{+0.0049}_{-0.0006}$	24./28

Table 7.5: Determination of $\alpha_s(M_Z)$ from the ratio R_{32} in the $H_{T,2}/2$ range from 0.3 up to 1.68 TeV at the central scale and for the six scale factor combinations for the two PDF sets MSTW2008 and MMHT2014.

$\mu_r/H_{T,2}/2$	$\mu_f/H_{T,2}/2$	MSTW2008		MMHT2014	
		$\alpha_s(M_Z)$	χ^2/n_{dof}	$\alpha_s(M_Z)$	χ^2/n_{dof}
1	1	0.1150	26./28	0.1142	24./28
1/2	1/2	0.1165	77./28	0.1160	73./28
2	2	0.1200	18./28	0.1191	18./28
1/2	1	0.1150	53./28	0.1136	48./28
1	1/2	0.1150	30./28	0.1142	28./28
1	2	0.1155	23./28	0.1147	22./28
2	1	0.1180	19./28	0.1175	19./28

Table 7.6: Uncertainty decomposition for $\alpha_s(M_Z)$ from the determination of α_S from the jet event rate R_{32} in bins of $H_{T,2}/2$. The statistical uncertainty of the NLO computation is negligible in comparison to any of the other sources of uncertainty. Electroweak corrections, significant only at high $H_{T,2}/2$, are assumed to cancel between the numerator and denominator.

$H_{T,2}/2$ (GeV)	MSTW2008					MMHT2014				
	$\alpha_s(M_Z)$	exp	PDF	NP	scale	$\alpha_s(M_Z)$	exp	PDF	NP	scale
300-420	0.1157	± 0.0015	± 0.0014	± 0.0019	$^{+0.0053}_{-0.0000}$	0.1158	± 0.0014	± 0.0010	± 0.0019	$^{+0.0052}_{-0.0000}$
420-600	0.1153	± 0.0011	± 0.0014	± 0.0018	$^{+0.0057}_{-0.0000}$	0.1154	± 0.0011	± 0.0012	± 0.0017	$^{+0.0056}_{-0.0000}$
600-1000	0.1134	± 0.0013	± 0.0016	± 0.0019	$^{+0.0052}_{-0.0000}$	0.1140	± 0.0012	± 0.0012	± 0.0018	$^{+0.0045}_{-0.0000}$
1000-1680	0.1147	± 0.0029	± 0.0017	± 0.0018	$^{+0.0063}_{-0.0011}$	0.1154	± 0.0025	± 0.0014	± 0.0015	$^{+0.0056}_{-0.0011}$
300-1680	0.1150	± 0.0010	± 0.0013	± 0.0015	$^{+0.0050}_{-0.0000}$	0.1142	± 0.0010	± 0.0013	± 0.0014	$^{+0.0049}_{-0.0006}$

is the differential cross-section weighted average $H_{\text{T},2}/2$ scale from the inclusive 2-jet calculations and integrated over all the measured $H_{\text{T},2}/2$ bins contributing to that given $H_{\text{T},2}/2$ range. Let N_{bin}^j be the total number of measured $H_{\text{T},2}/2$ bins contributing to the j -th $H_{\text{T},2}/2$ range, then the corresponding scale Q_j , shown in second column of Table 7.7, is calculated as :

$$Q_j = \frac{\sum_{i=1}^{N_{\text{bin}}^j} H_{\text{T},2}^i \left[\frac{d\sigma}{d(H_{\text{T},2}/2)} \right]^i}{\sum_{i=1}^{N_{\text{bin}}^j} \left[\frac{d\sigma}{d(H_{\text{T},2}/2)} \right]^i} \quad (7.9)$$

The value of $\alpha_s(M_Z)$ is extracted in each $H_{\text{T},2}/2$ range. These extracted $\alpha_s(M_Z)$ values are evolved to the corresponding values $\alpha_s(Q)$ and are quoted in Table 7.7 along with the extracted $\alpha_s(M_Z)$ values and the total uncertainty. The evolution is performed for five flavours at 2-loop order with the RUNDEC program [124, 125]. The obtained $\alpha_s(Q)$ points (black solid circles) are shown as a function of scale Q in Fig. 7.4. The black solid line and the yellow uncertainty band are evolved using $\alpha_s(M_Z) = 0.1150 \pm 0.0023$ (all except scale) $^{+0.0050}_{-0.0000}$ (scale) obtained using MSTW2008 NLO PDF set. The world average [18] (dashed line) and results from other measurements of the CMS [1, 91, 105, 114, 115], ATLAS [116], D0 [117, 118], H1 [119, 120], and ZEUS [121] experiments are also imposed. The current measurement is in very good agreement within the uncertainty with other results obtained by previous experiments as well as with the world average value of $\alpha_s(M_Z) = 0.1181 \pm 0.0011$ derived in Ref. [18].

Table 7.7: Evolution of the strong coupling constant between the scale of the Z boson mass and the cross-section averaged $H_{T,2}/2$ scale $\langle Q \rangle$ for the separate determinations in each respective fit range. The evolution is performed for five flavours at 2-loop order with the RUNDEC program [124, 125].

$H_{T,2}/2$ (GeV)	$\langle Q \rangle$ (GeV)	$\alpha_s(M_Z)$	$\alpha_s(Q)$	No. of data points	χ^2/n_{dof}
300-420	340	$0.1157^{+0.0060}_{-0.0030}$	$0.0969^{+0.0041}_{-0.0021}$	4	2.8/3
420-600	476	$0.1153^{+0.0062}_{-0.0025}$	$0.0928^{+0.0039}_{-0.0016}$	6	6.1/5
600-1000	685	$0.1134^{+0.0059}_{-0.0028}$	$0.0879^{+0.0035}_{-0.0017}$	9	7.1/8
1000-1680	1114	$0.1147^{+0.0074}_{-0.0040}$	$0.0841^{+0.0039}_{-0.0021}$	10	5.4/9

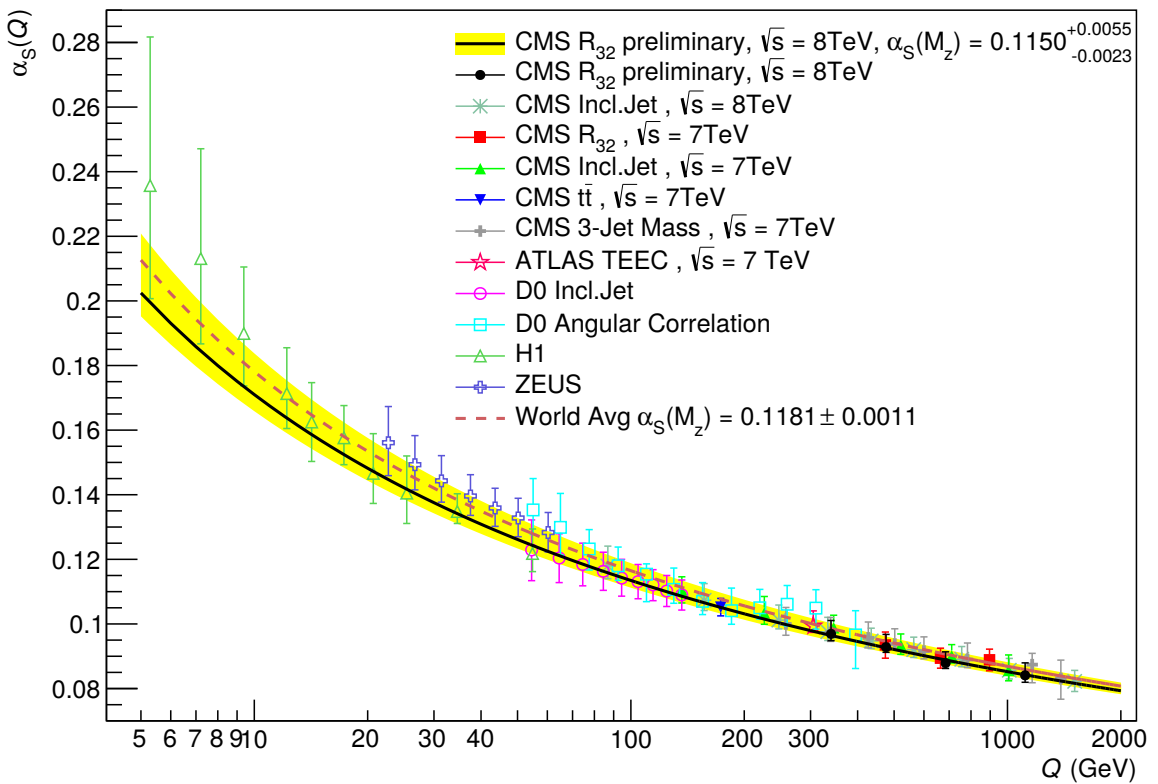


Figure 7.4: The running $\alpha_s(Q)$ as a function of the energy scale Q is shown as obtained by using the MSTW2008 NLO PDF set. The solid line and the uncertainty band are drawn by evolving the extracted $\alpha_s(M_Z)$ values using the 2-loop 5-flavour renormalization group equations as implemented in RUNDEC [124, 125]. The dashed line represents the evolution of the world average [18] and the black circles correspond to the $\alpha_s(Q)$ determinations presented in Table 7.7. Results from other measurements of CMS [1, 91, 105, 114, 115], ATLAS [116], D0 [117, 118], H1 [119, 120], and ZEUS [121] are superimposed.

Chapter 8

Summary

Inclusive multijet production cross-section measured precisely in terms of jet transverse momentum is one of the important observables in understanding physics at hadron colliders. It provides the essential information about the structure of parton through parton distribution functions (PDFs) and the precise measurement of the strong coupling constant α_S . The value of the strong coupling constant at the scale of the Z boson mass $\alpha_s(M_Z)$ can be determined using cross-section ratio instead of individual cross-sections because many uncertainties of theoretical and experimental origin cancel between numerator and denominator which reduces the dependence on PDFs, renormalization and factorization scales, luminosity etc.

In this thesis, a measurement of the inclusive 2-jet and 3-jet event cross-sections as well as the cross-section ratio R_{32} has been presented. The data sample has been collected from proton-proton collisions recorded with the CMS detector at a centre-of-mass energy of 8 TeV and corresponds to an integrated luminosity of 19.7 fb^{-1} . The jets are reconstructed with the anti- k_t clustering algorithm for a jet size parameter $R = 0.7$. The inclusive 2-jet and 3-jet event cross-sections are measured differentially as a function of the average transverse momentum of the two leading jets, referred as $H_{\text{T},2}/2$. The ratio R_{32} is obtained by dividing the differential cross-sections of inclusive 3-jet events to that of inclusive 2-jet one in

each bin of $H_{\mathrm{T},2}/2$. An appropriate selection criteria has been designed for choosing the best events for analysis. The measurements are performed at a central rapidity of $|y| < 2.5$ in a range of $0.3 < H_{\mathrm{T},2}/2 < 2.0 \text{ TeV}$ for inclusive 2-jet event cross-sections and $0.3 < H_{\mathrm{T},2}/2 < 1.68 \text{ TeV}$ for inclusive 3-jet event cross-sections and ratio R_{32} .

The measured cross-sections after correcting for detector effects by using an iterative unfolding procedure are compared to the perturbative QCD predictions computed, using NLOJET++ program, at next-to-leading order (NLO) accuracy and complemented with non-perturbative (NP) corrections that are important at low $H_{\mathrm{T},2}/2$. The data are found to be well described by NLO calculations. The upwards trend observed in the inclusive 2-jet and 3-jet data at high $H_{\mathrm{T},2}/2$ in comparison to the prediction at NLO QCD, is explained by the onset of electroweak (EW) corrections in the 2-jet case. For the 3-jet event cross-sections these corrections have not yet been computed yet. In the 3-jet to 2-jet cross-section ratio R_{32} , the EW corrections are assumed to cancel. In fact, NLO QCD provides an adequate description of R_{32} in the accessible range of $H_{\mathrm{T},2}/2$. In contrast, leading order (LO) tree-level Monte Carlo (MC) predictions obtained using MADGRAPH5 event generator interfaced to PYTHIA6 exhibit significant deviations. The sources of experimental and theoretical uncertainties are studied in details. The experimental uncertainty ranges from 4 to 32% for inclusive 2-jet event cross-sections, from 4 to 28% for 3-jet event cross-sections and from 1 to 28% for cross-section ratio R_{32} . It is dominated by the uncertainty due to the jet energy corrections (JEC) at lower $H_{\mathrm{T},2}/2$ values and by statistical uncertainty at higher $H_{\mathrm{T},2}/2$ values. The theoretical uncertainty ranges from 3 to 30% and 5 to 34% for inclusive 2-jet and 3-jet event cross-sections respectively and from 3 to 11% for ratio R_{32} . The PDF uncertainty derived with the CT10-NLO PDF set is the dominant source of theoretical uncertainty.

The inclusive multijet cross-sections being proportional to the powers of the strong coupling constant α_S ($\sigma_{n\text{-jet}} \propto \alpha_S^n$) are used to extract the value of the strong coupling constant at the scale of the Z boson mass $\alpha_s(M_Z)$. In cross-section ratio R_{32} which proportional to α_S , many uncertainties and PDF dependencies largely cancel and hence becomes the better tool to extract the value of $\alpha_s(M_Z)$. In this thesis, a fit of the ratio of the inclusive 3-jet event cross-section to that of 2-jet, R_{32} in the range $0.3 < H_{T,2}/2 < 1.68$ TeV using the MSTW2008 PDF set gives :

$$\begin{aligned}\alpha_s(M_Z) &= 0.1150 \pm 0.0010 \text{ (exp)} \pm 0.0013 \text{ (PDF)} \pm 0.0015 \text{ (NP)} {}^{+0.0050}_{-0.0000} \text{ (scale)} \\ &= 0.1150 \pm 0.0023 \text{ (all except scale)} {}^{+0.0050}_{-0.0000} \text{ (scale)}\end{aligned}$$

Very similar results are obtained using the MMHT2014 PDF set which gives :

$$\begin{aligned}\alpha_s(M_Z) &= 0.1142 \pm 0.0010 \text{ (exp)} \pm 0.0013 \text{ (PDF)} \pm 0.0014 \text{ (NP)} {}^{+0.0049}_{-0.0006} \text{ (scale)} \\ &= 0.1142 \pm 0.0022 \text{ (all except scale)} {}^{+0.0049}_{-0.0006} \text{ (scale)}\end{aligned}$$

The equally compatible values of $\alpha_s(M_Z)$ are determined with separate fits to the inclusive 2-jet and 3-jet event cross-sections provided the range in $H_{T,2}/2$ is restricted to $0.3 < H_{T,2}/2 < 1.0$ TeV. The extracted $\alpha_s(M_Z)$ values in sub-ranges of $H_{T,2}/2$ are evolved to corresponding $\alpha_S(Q)$ along with the error bars at different scales Q . The current measurement of $\alpha_s(M_Z)$ and the running of $\alpha_S(Q)$ as a function of Q is in well agreement within uncertainties with the world average value of $\alpha_s(M_Z) = 0.1181 \pm 0.0011$ [18] and already existing determinations performed by the CMS and other experiments.

The inclusion of the EW corrections in inclusive 2-jet event cross-sections become relevant at $H_{T,2}/2$ beyond 1 TeV. Their availability for 3-jet one and hence cross-section ratio R_{32} can improve the precision of the measurement of $\alpha_s(M_Z)$. Also as the theoretical calculations will be available for inclusive 4-jet event cross-sections, the various cross-section ratios such as $R_{43} \propto \alpha_S^1$ and $R_{42} \propto \alpha_S^2$ can be measured to extract the value of the strong coupling constant more precisely. Currently LHC is running at high center-of-mass energy of 13 TeV delivering a higher

instantaneous luminosity and this makes possible to access the extended phase space and perform the measurements with more accuracy.

Appendix A

A.1 Cross-section Ratio, R_{32}

Table A.1: Differential cross-sections ($\times 10^{-3}(\text{pb}/\text{GeV})$) and cross-section ratio R_{32} at detector level in each bin of $H_{\text{T},2}/2$, along with statistical uncertainty (in %).

Bin	2-jet cross-section	Stat. unc.	3-jet cross-section	Stat. unc.	Ratio R_{32}	Stat. unc.
300 - 330	29772.726	0.211	2640.629	0.707	0.089	+0.665 -0.661
330 - 360	16792.917	0.231	1773.485	0.704	0.106	+0.523 -0.521
360 - 390	9889.326	0.182	1176.544	0.526	0.119	+0.485 -0.483
390 - 420	5976.777	0.179	778.034	0.492	0.130	+0.206 -0.206
420 - 450	3731.760	0.067	522.624	0.180	0.140	+0.167 -0.167
450 - 480	2398.741	0.084	357.622	0.217	0.149	+0.201 -0.200
480 - 510	1570.192	0.104	246.051	0.262	0.157	+0.241 -0.241
510 - 540	1048.665	0.127	171.080	0.314	0.163	+0.288 -0.287
540 - 570	713.042	0.154	119.566	0.376	0.168	+0.344 -0.343
570 - 600	490.776	0.186	84.798	0.447	0.173	+0.407 -0.406
600 - 640	325.046	0.198	57.463	0.470	0.177	+0.427 -0.426
640 - 680	205.727	0.248	37.282	0.583	0.181	+0.529 -0.527
680 - 720	133.674	0.308	24.859	0.714	0.186	+0.646 -0.643
720 - 760	87.911	0.380	16.560	0.875	0.188	+0.791 -0.786
760 - 800	58.657	0.465	11.056	1.071	0.188	+0.968 -0.961
800 - 850	38.106	0.516	7.318	1.178	0.192	+1.063 -1.054
850 - 900	23.587	0.656	4.600	1.485	0.195	+1.339 -1.326
900 - 950	15.130	0.819	2.896	1.872	0.191	+1.694 -1.672
950 - 1000	9.696	1.023	1.812	2.366	0.187	+2.151 -2.116
1000 - 1060	6.026	1.185	1.186	2.670	0.197	+2.414 -2.371
1060 - 1120	3.668	1.518	0.716	3.436	0.195	+3.118 -3.046
1120 - 1180	2.327	1.906	0.437	4.398	0.188	+4.024 -3.903
1180 - 1250	1.419	2.260	0.265	5.227	0.187	+4.798 -4.627
1250 - 1320	0.853	2.915	0.165	6.623	0.194	+6.080 -5.811
1320 - 1390	0.477	3.898	0.080	9.492	0.169	+8.951 -8.355
1390 - 1460	0.263	5.249	0.042	13.131	0.160	+12.619 -11.449
1460 - 1530	0.192	6.143	0.029	15.811	0.151	+15.437 -13.698
1530 - 1600	0.104	8.362	0.021	18.570	0.203	+17.571 -15.536
1600 - 1680	0.060	10.314	0.009	26.726	0.149	+27.132 -22.170

A.2 Individual Sources of Jet Energy Correction Uncertainties

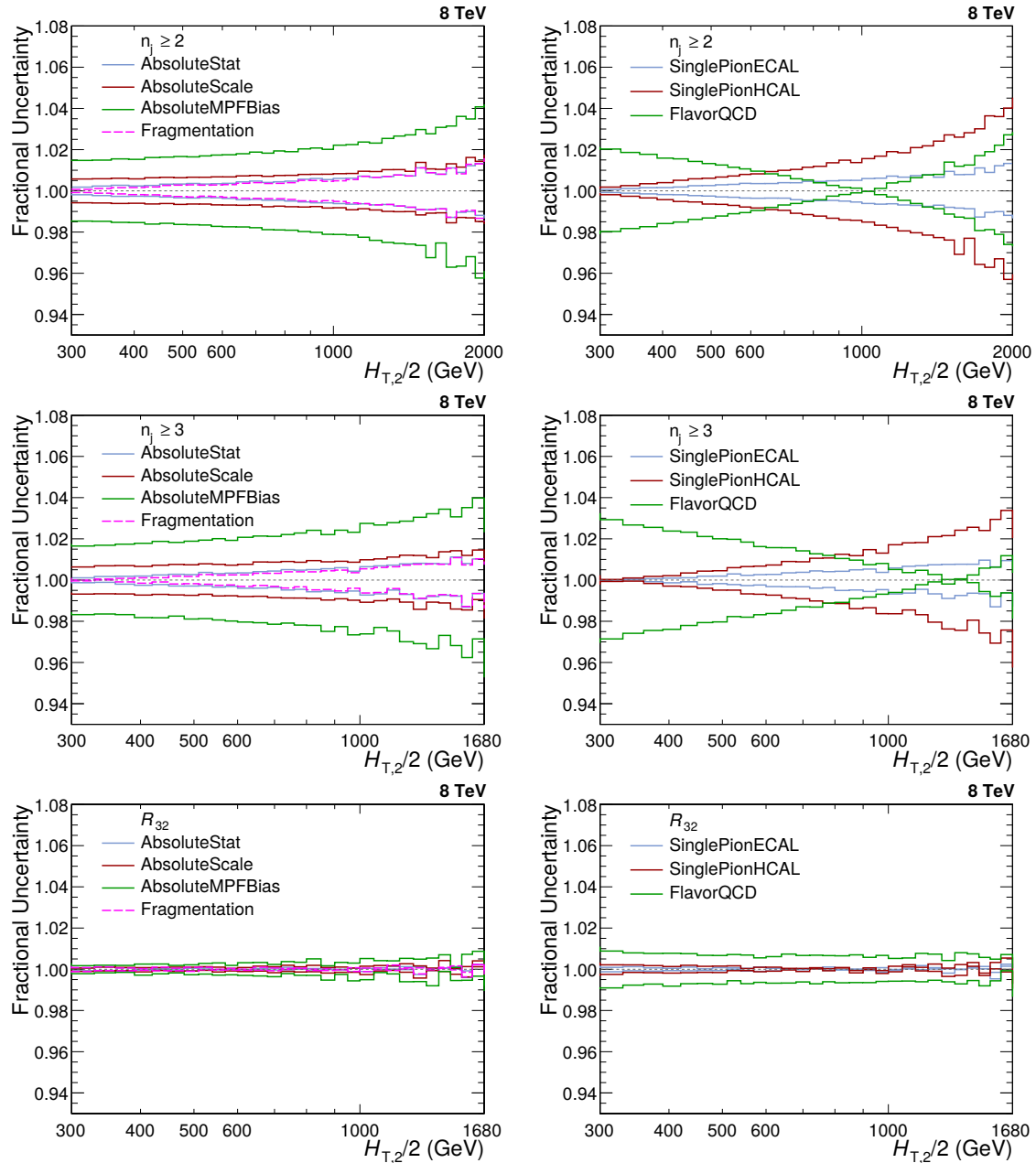


Figure A.1: The fractional jet energy correction (JEC) uncertainties from individual sources are shown for inclusive 2-jet (top) and 3-jet events cross-sections (middle); and cross-section ratio R_{32} (bottom). On left, JEC uncertainties are evaluated from AbsoluteStat (blue), AbsoluteScale (red), AbsoluteMPFBias (green) and Fragmentation (pink) sources whereas on right, these are evaluated from SinglePionECAL (blue), SinglePionHCAL (red) and FlavorQCD (green) sources.

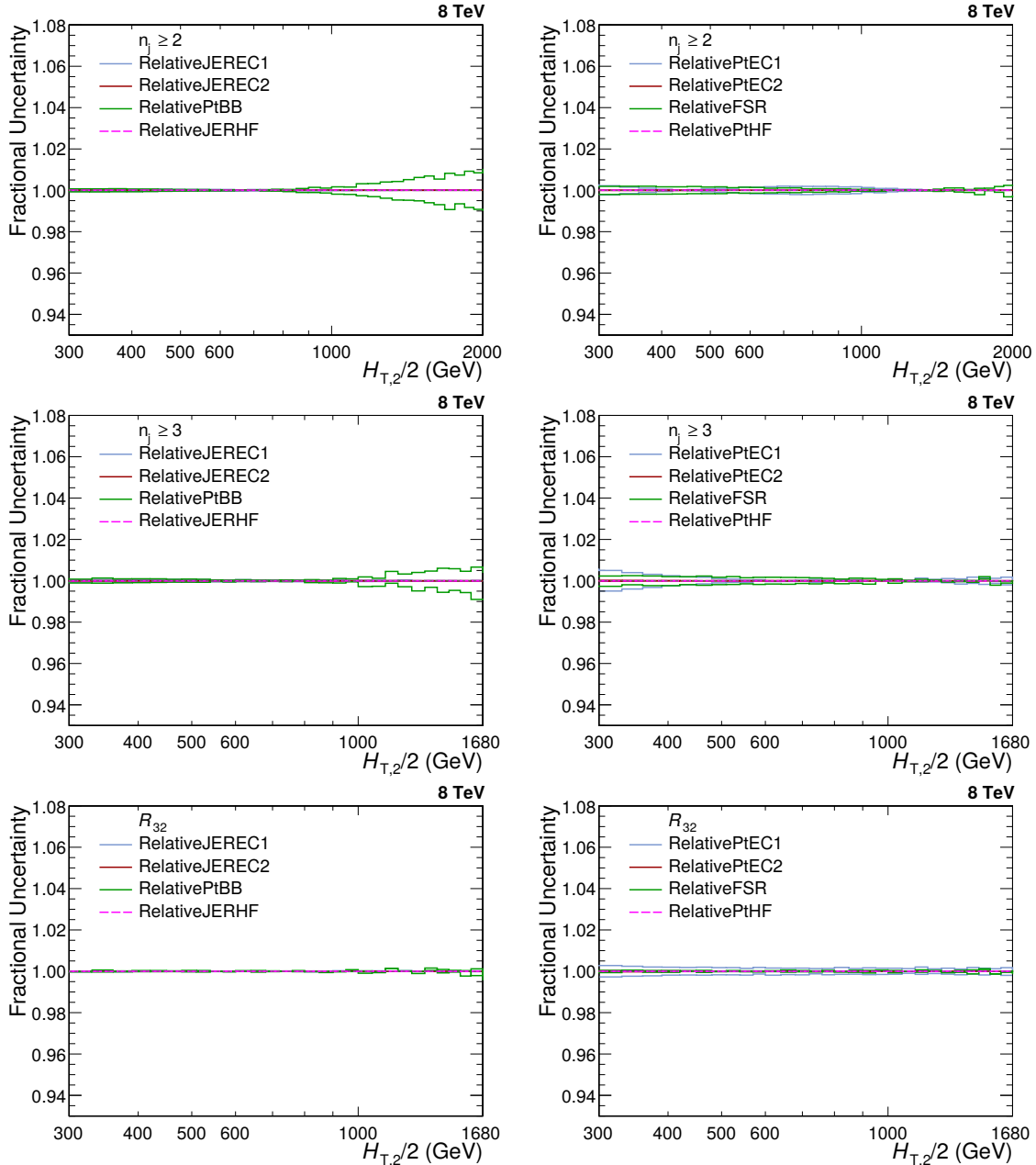


Figure A.2: The fractional jet energy correction (JEC) uncertainties from individual sources are shown for inclusive 2-jet (top) and 3-jet events cross-sections (middle); and cross-section ratio R_{32} (bottom). On left, JEC uncertainties are evaluated from RelativeJEREC1 (blue), RelativeJEREC2 (red), RelativePtBB (green) and RelativeJERHF (pink) sources whereas on right, these are evaluated from RelativePtEC1 (blue), RelativePtEC2 (red), RelativeFSR (green) and RelativePtHF (pink) sources.

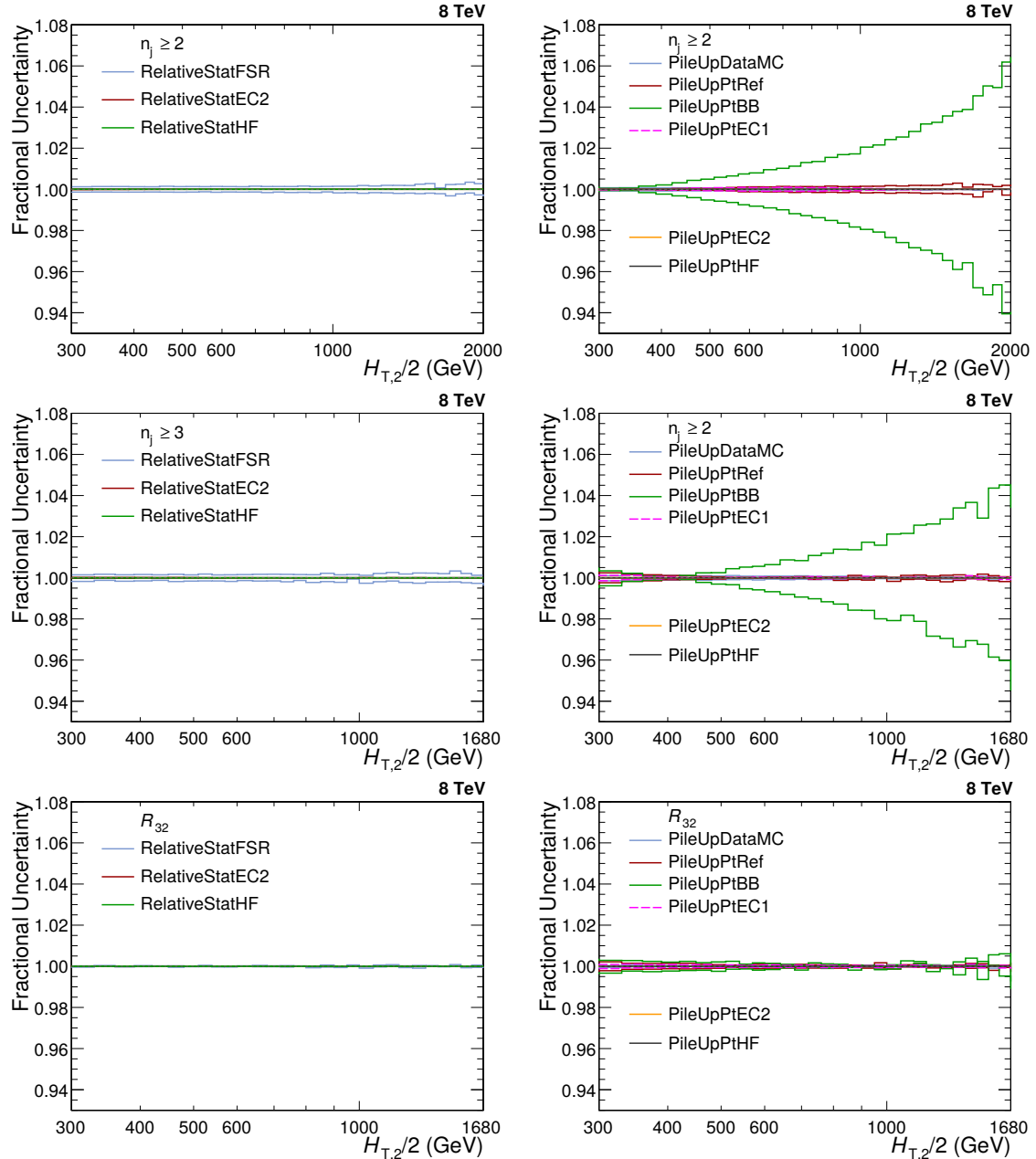


Figure A.3: The fractional jet energy correction (JEC) uncertainties from individual sources are shown for inclusive 2-jet (top) and 3-jet events cross-sections (middle); and cross-section ratio R_{32} (bottom). On left, JEC uncertainties are evaluated from `RelativeStatFSR` (blue), `RelativeStatEC2` (red) and `RelativeStatHF` (green) sources whereas on right, these are evaluated from `PileUpDataMC` (blue), `PileUpPtRef` (red), `PileUpPtBB` (green), `PileUpPtEC1` (pink), `PileUpPtEC2` (orange) and `PileUpPtHF` (black) sources.

A.3 Experimental Uncertainties

Table A.2: Experimental uncertainties (in %), from all sources as well as the total uncertainty, affecting the cross-section measurement in each bin of $H_{T,2}/2$ for inclusive 2-jet events.

Bin	Statistical	JEC	Unfolding	Lumi	Residual	Total
300 - 330	0.242	+2.612 -2.565	+0.948 -0.928	2.6	1.0	+3.942 -3.906
330 - 360	0.258	+2.507 -2.473	+0.976 -0.969	2.6	1.0	+3.882 -3.858
360 - 390	0.202	+2.504 -2.465	+0.779 -0.783	2.6	1.0	+3.831 -3.807
390 - 420	0.193	+2.363 -2.381	+0.905 -0.904	2.6	1.0	+3.768 -3.780
420 - 450	0.084	+2.448 -2.422	+0.904 -0.895	2.6	1.0	+3.818 -3.799
450 - 480	0.096	+2.440 -2.352	+0.797 -0.795	2.6	1.0	+3.789 -3.733
480 - 510	0.107	+2.427 -2.406	+0.728 -0.715	2.6	1.0	+3.767 -3.751
510 - 540	0.128	+2.425 -2.395	+0.835 -0.862	2.6	1.0	+3.789 -3.775
540 - 570	0.154	+2.425 -2.376	+0.687 -0.674	2.6	1.0	+3.760 -3.726
570 - 600	0.180	+2.497 -2.474	+0.839 -0.827	2.6	1.0	+3.838 -3.820
600 - 640	0.209	+2.495 -2.491	+0.744 -0.743	2.6	1.0	+3.819 -3.816
640 - 680	0.264	+2.582 -2.545	+0.912 -0.912	2.6	1.0	+3.915 -3.891
680 - 720	0.320	+2.691 -2.574	+0.763 -0.756	2.6	1.0	+3.961 -3.880
720 - 760	0.387	+2.690 -2.755	+0.705 -0.712	2.6	1.0	+3.955 -4.001
760 - 800	0.465	+2.858 -2.846	+0.859 -0.846	2.6	1.0	+4.109 -4.098
800 - 850	0.548	+2.889 -2.913	+0.783 -0.787	2.6	1.0	+4.126 -4.143
850 - 900	0.698	+3.145 -3.102	+0.961 -0.958	2.6	1.0	+4.366 -4.334
900 - 950	0.847	+3.298 -3.233	+0.828 -0.829	2.6	1.0	+4.476 -4.429
950 - 1000	1.041	+3.291 -3.330	+0.895 -0.872	2.6	1.0	+4.525 -4.549
1000 - 1060	1.268	+3.598 -3.569	+0.945 -0.956	2.6	1.0	+4.817 -4.798
1060 - 1120	1.611	+3.759 -3.756	+0.970 -0.967	2.6	1.0	+5.043 -5.040
1120 - 1180	1.985	+4.154 -4.053	+1.089 -1.080	2.6	1.0	+5.490 -5.413
1180 - 1250	2.406	+4.251 -4.313	+1.062 -1.070	2.6	1.0	+5.722 -5.770
1250 - 1320	3.101	+4.696 -4.624	+1.151 -1.144	2.6	1.0	+6.384 -6.330
1320 - 1390	4.157	+4.934 -4.979	+1.343 -1.341	2.6	1.0	+7.155 -7.186
1390 - 1460	5.270	+5.148 -5.104	+1.185 -1.177	2.6	1.0	+7.965 -7.936
1460 - 1530	6.360	+5.890 -5.652	+1.405 -1.406	2.6	1.0	+9.213 -9.063
1530 - 1600	8.183	+5.924 -6.311	+1.598 -1.590	2.6	1.0	+10.601 -10.821
1600 - 1680	10.630	+5.969 -5.655	+1.607 -1.592	2.6	1.0	+12.608 -12.461
1680 - 1760	13.864	+7.245 -7.603	+1.821 -1.839	2.6	1.0	+15.993 -16.161
1760 - 1840	18.192	+7.781 -7.820	+1.902 -1.906	2.6	1.0	+20.071 -20.087
1840 - 1920	22.612	+7.647 -7.537	+1.588 -1.590	2.6	1.0	+24.085 -24.050
1920 - 2000	29.530	+9.199 -9.469	+1.511 -1.505	2.6	1.0	+31.092 -31.172

Table A.3: Experimental uncertainties (in %), from all sources as well as the total uncertainty, affecting the cross-section measurement in each bin of $H_{T,2}/2$ for inclusive 3-jet events.

Bin	Statistical	JEC	Unfolding	Lumi	Residual	Total
300 - 330	0.796	+3.503 -3.475	+0.564 -0.552	2.6	1.0	+4.581 -4.558
330 - 360	0.781	+3.303 -3.186	+0.640 -0.633	2.6	1.0	+4.437 -4.350
360 - 390	0.583	+3.221 -3.094	+0.490 -0.496	2.6	1.0	+4.326 -4.233
390 - 420	0.531	+3.092 -3.149	+0.584 -0.584	2.6	1.0	+4.236 -4.278
420 - 450	0.224	+3.125 -2.996	+0.604 -0.592	2.6	1.0	+4.236 -4.140
450 - 480	0.248	+2.984 -2.890	+0.531 -0.528	2.6	1.0	+4.124 -4.056
480 - 510	0.269	+2.937 -2.963	+0.511 -0.512	2.6	1.0	+4.089 -4.108
510 - 540	0.318	+3.021 -2.797	+0.592 -0.612	2.6	1.0	+4.164 -4.007
540 - 570	0.375	+2.999 -2.935	+0.506 -0.500	2.6	1.0	+4.141 -4.094
570 - 600	0.434	+2.824 -2.906	+0.646 -0.620	2.6	1.0	+4.042 -4.096
600 - 640	0.497	+2.952 -2.956	+0.598 -0.604	2.6	1.0	+4.133 -4.136
640 - 680	0.617	+3.111 -3.001	+0.777 -0.786	2.6	1.0	+4.292 -4.215
680 - 720	0.739	+3.067 -2.984	+0.642 -0.611	2.6	1.0	+4.257 -4.194
720 - 760	0.895	+3.185 -3.111	+0.595 -0.607	2.6	1.0	+4.366 -4.313
760 - 800	1.068	+3.231 -3.166	+0.763 -0.774	2.6	1.0	+4.464 -4.419
800 - 850	1.250	+3.427 -3.295	+0.674 -0.687	2.6	1.0	+4.639 -4.544
850 - 900	1.578	+3.364 -3.540	+0.903 -0.898	2.6	1.0	+4.731 -4.857
900 - 950	1.961	+3.594 -3.524	+0.792 -0.793	2.6	1.0	+5.015 -4.965
950 - 1000	2.420	+3.603 -3.783	+0.846 -0.843	2.6	1.0	+5.226 -5.351
1000 - 1060	2.844	+4.164 -4.116	+0.916 -0.940	2.6	1.0	+5.834 -5.803
1060 - 1120	3.647	+4.038 -3.815	+0.963 -0.957	2.6	1.0	+6.188 -6.044
1120 - 1180	4.607	+4.278 -4.183	+1.084 -1.087	2.6	1.0	+6.961 -6.904
1180 - 1250	5.532	+4.894 -4.771	+1.074 -1.069	2.6	1.0	+7.967 -7.891
1250 - 1320	7.141	+5.144 -5.273	+1.222 -1.217	2.6	1.0	+9.312 -9.383
1320 - 1390	10.207	+5.542 -5.642	+1.414 -1.428	2.6	1.0	+12.027 -12.076
1390 - 1460	13.831	+5.630 -5.265	+1.257 -1.256	2.6	1.0	+15.242 -15.111
1460 - 1530	15.578	+5.576 -5.491	+1.546 -1.551	2.6	1.0	+16.850 -16.822
1530 - 1600	18.729	+6.409 -7.019	+1.718 -1.716	2.6	1.0	+20.063 -20.266
1600 - 1680	26.465	+7.017 -6.255	+1.775 -1.765	2.6	1.0	+27.578 -27.393

Table A.4: Experimental uncertainties (in %), from all sources as well as the total uncertainty, affecting the measurement of cross-section ratio R_{32} , in each bin of $H_{\mathrm{T},2}/2$.

Bin	Statistical	JEC	Unfolding	Total
300 - 330	0.741	+1.059 -1.097	+0.754 -0.751	+1.496 -1.522
330 - 360	0.587	+0.954 -0.923	+0.685 -0.689	+1.313 -1.292
360 - 390	0.519	+0.902 -0.855	+0.594 -0.593	+1.199 -1.163
390 - 420	0.236	+0.907 -0.952	+0.439 -0.438	+1.035 -1.074
420 - 450	0.192	+0.900 -0.835	+0.360 -0.361	+0.988 -0.930
450 - 480	0.209	+0.788 -0.802	+0.307 -0.308	+0.872 -0.884
480 - 510	0.245	+0.795 -0.867	+0.254 -0.235	+0.870 -0.931
510 - 540	0.287	+0.852 -0.682	+0.264 -0.268	+0.937 -0.787
540 - 570	0.326	+0.807 -0.803	+0.193 -0.189	+0.891 -0.887
570 - 600	0.397	+0.656 -0.774	+0.199 -0.219	+0.792 -0.898
600 - 640	0.447	+0.763 -0.797	+0.150 -0.154	+0.897 -0.926
640 - 680	0.573	+0.861 -0.781	+0.153 -0.140	+1.045 -0.979
680 - 720	0.663	+0.766 -0.787	+0.147 -0.164	+1.024 -1.042
720 - 760	0.774	+0.842 -0.769	+0.118 -0.118	+1.149 -1.097
760 - 800	0.970	+0.800 -0.729	+0.115 -0.096	+1.263 -1.218
800 - 850	1.116	+0.873 -0.775	+0.115 -0.104	+1.422 -1.363
850 - 900	1.436	+0.770 -0.896	+0.069 -0.069	+1.631 -1.694
900 - 950	1.716	+0.704 -0.752	+0.050 -0.051	+1.855 -1.874
950 - 1000	2.156	+0.824 -0.897	+0.089 -0.045	+2.310 -2.336
1000 - 1060	2.554	+0.812 -0.870	+0.045 -0.040	+2.680 -2.698
1060 - 1120	3.244	+0.792 -0.658	+0.018 -0.027	+3.339 -3.310
1120 - 1180	4.121	+0.985 -0.757	+0.025 -0.043	+4.237 -4.191
1180 - 1250	4.990	+1.031 -0.848	+0.023 -0.041	+5.095 -5.062
1250 - 1320	6.456	+0.750 -1.087	+0.079 -0.079	+6.500 -6.548
1320 - 1390	8.990	+1.112 -1.144	+0.080 -0.099	+9.059 -9.063
1390 - 1460	12.699	+1.157 -0.815	+0.076 -0.078	+12.751 -12.725
1460 - 1530	13.926	+0.768 -1.235	+0.143 -0.145	+13.948 -13.981
1530 - 1600	16.903	+1.050 -1.258	+0.120 -0.127	+16.936 -16.950
1600 - 1680	28.070	+1.471 -0.859	+0.178 -0.177	+28.109 -28.084

A.4 Theoretical Uncertainties

Table A.5: Theoretical uncertainties (in %), calculated using CT10-NLO PDF set from all sources as well as the total uncertainty, affecting the cross-section measurement in each bin of $H_{T,2}/2$ for inclusive 2-jet events.

Bin	Scale	PDF	NP	Total
300 - 330	+0.942 -6.149	+3.566 -3.090	0.825	+3.780 -6.931
330 - 360	+1.035 -6.289	+3.906 -3.342	0.736	+4.107 -7.159
360 - 390	+1.159 -6.438	+4.232 -3.573	0.696	+4.442 -7.396
390 - 420	+1.220 -6.536	+4.551 -3.794	0.723	+4.767 -7.592
420 - 450	+1.326 -6.660	+4.857 -3.997	0.745	+5.089 -7.802
450 - 480	+1.421 -6.776	+5.153 -4.186	0.765	+5.399 -8.001
480 - 510	+1.512 -6.888	+5.444 -4.365	0.782	+5.704 -8.192
510 - 540	+1.566 -6.967	+5.721 -4.527	0.797	+5.984 -8.347
540 - 570	+1.666 -7.082	+6.000 -4.682	0.810	+6.279 -8.528
570 - 600	+1.731 -7.172	+6.269 -4.825	0.822	+6.555 -8.683
600 - 640	+1.805 -7.271	+6.597 -4.979	0.833	+6.890 -8.852
640 - 680	+1.930 -7.416	+6.978 -5.143	0.845	+7.289 -9.064
680 - 720	+2.007 -7.527	+7.364 -5.295	0.856	+7.680 -9.243
720 - 760	+2.113 -7.663	+7.749 -5.437	0.865	+8.078 -9.436
760 - 800	+2.196 -7.781	+8.140 -5.569	0.873	+8.476 -9.609
800 - 850	+2.323 -7.945	+8.573 -5.706	0.881	+8.926 -9.822
850 - 900	+2.389 -8.062	+9.082 -5.863	0.889	+9.433 -10.008
900 - 950	+2.499 -8.227	+9.600 -6.018	0.896	+9.961 -10.232
950 - 1000	+2.631 -8.402	+10.134 -6.166	0.902	+10.509 -10.460
1000 - 1060	+2.738 -8.569	+10.747 -6.343	0.908	+11.127 -10.700
1060 - 1120	+2.853 -8.751	+11.431 -6.526	0.914	+11.817 -10.955
1120 - 1180	+2.992 -8.970	+12.183 -6.727	0.919	+12.579 -11.250
1180 - 1250	+3.135 -9.194	+13.019 -6.944	0.924	+13.423 -11.558
1250 - 1320	+3.324 -9.469	+14.004 -7.189	0.929	+14.423 -11.925
1320 - 1390	+3.434 -9.677	+15.080 -7.444	0.933	+15.494 -12.244
1390 - 1460	+3.629 -9.976	+16.223 -7.700	0.937	+16.650 -12.637
1460 - 1530	+3.760 -10.224	+17.505 -7.980	0.940	+17.929 -13.004
1530 - 1600	+3.894 -10.471	+18.891 -8.258	0.943	+19.311 -13.368
1600 - 1680	+4.107 -10.813	+20.496 -8.560	0.946	+20.925 -13.824
1680 - 1760	+4.421 -11.101	+22.481 -8.905	0.949	+22.931 -14.263
1760 - 1840	+4.921 -11.461	+24.654 -9.251	0.951	+25.158 -14.760
1840 - 1920	+5.404 -11.813	+27.143 -9.607	0.953	+27.692 -15.256
1920 - 2000	+5.867 -12.154	+29.986 -9.973	0.955	+30.570 -15.751

Table A.6: Theoretical uncertainties (in %), calculated using CT10-NLO PDF set from all sources as well as the total uncertainty, affecting the cross-section measurement in each bin of $H_{T,2}/2$ for inclusive 3-jet events.

Bin	Scale	PDF	NP	Total
300 - 330	+0.539 -8.294	+5.716 -4.657	1.692	+5.986 -9.662
330 - 360	+0.550 -8.577	+5.977 -4.779	1.516	+6.191 -9.935
360 - 390	+0.599 -8.709	+6.187 -4.987	1.363	+6.363 -10.128
390 - 420	+0.719 -8.948	+6.751 -5.223	1.228	+6.900 -10.433
420 - 450	+0.799 -9.145	+7.031 -5.395	1.110	+7.162 -10.676
450 - 480	+0.847 -9.247	+7.404 -5.578	1.005	+7.520 -10.845
480 - 510	+0.847 -9.294	+7.837 -5.717	0.937	+7.938 -10.951
510 - 540	+0.922 -9.436	+8.198 -5.884	0.921	+8.301 -11.158
540 - 570	+0.974 -9.566	+8.529 -6.000	0.904	+8.632 -11.328
570 - 600	+1.086 -9.786	+8.970 -6.156	0.886	+9.079 -11.595
600 - 640	+1.107 -9.852	+9.402 -6.297	0.866	+9.506 -11.724
640 - 680	+1.278 -10.101	+10.310 -6.526	0.842	+10.423 -12.055
680 - 720	+1.384 -10.342	+9.682 -6.618	0.820	+9.815 -12.305
720 - 760	+1.415 -10.404	+11.051 -6.826	0.798	+11.170 -12.469
760 - 800	+1.547 -10.615	+11.565 -7.009	0.777	+11.694 -12.744
800 - 850	+1.679 -10.804	+12.242 -7.185	0.755	+12.379 -12.997
850 - 900	+2.085 -11.134	+13.097 -7.461	0.731	+13.282 -13.422
900 - 950	+2.475 -11.432	+13.889 -7.703	0.709	+14.125 -13.804
950 - 1000	+2.655 -11.608	+14.614 -7.915	0.688	+14.869 -14.066
1000 - 1060	+3.025 -11.926	+15.576 -8.173	0.667	+15.881 -14.473
1060 - 1120	+3.299 -12.189	+14.250 -8.441	0.645	+14.641 -14.840
1120 - 1180	+3.741 -12.584	+17.984 -8.787	0.625	+18.380 -15.361
1180 - 1250	+3.969 -12.843	+19.324 -9.127	0.625	+19.737 -15.768
1250 - 1320	+4.663 -13.452	+21.246 -9.517	0.642	+21.761 -16.490
1320 - 1390	+4.878 -13.702	+22.884 -9.899	0.657	+23.407 -16.916
1390 - 1460	+5.242 -14.095	+24.854 -10.332	0.670	+25.410 -17.489
1460 - 1530	+5.582 -14.464	+27.170 -10.733	0.682	+27.746 -18.024
1530 - 1600	+6.003 -14.907	+29.741 -11.165	0.692	+30.349 -18.637
1600 - 1680	+6.503 -15.418	+32.855 -11.617	0.702	+33.500 -19.317

Table A.7: Theoretical uncertainties (in %) calculated using CT10-NLO PDF set from all sources as well as the total uncertainty, affecting the measurement of cross-section ratio R_{32} , in each bin of $H_{T,2}/2$.

Bin	Scale	PDF	NP	Total
300 - 330	+0.038 -7.203	+2.458 -3.463	0.822	+2.592 -8.035
330 - 360	+0.027 -6.626	+2.317 -3.378	0.734	+2.431 -7.474
360 - 390	+0.024 -6.449	+2.149 -3.367	0.656	+2.247 -7.304
390 - 420	+0.084 -5.894	+2.411 -3.383	0.586	+2.482 -6.821
420 - 450	+0.113 -5.532	+2.345 -3.362	0.523	+2.405 -6.494
450 - 480	+0.109 -5.409	+2.390 -3.357	0.467	+2.438 -6.383
480 - 510	+0.073 -5.442	+2.506 -3.327	0.416	+2.541 -6.392
510 - 540	+0.107 -5.168	+2.559 -3.326	0.371	+2.588 -6.157
540 - 570	+0.112 -5.010	+2.586 -3.292	0.330	+2.609 -6.004
570 - 600	+0.163 -4.576	+2.729 -3.292	0.292	+2.750 -5.645
600 - 640	+0.146 -4.565	+2.824 -3.270	0.253	+2.839 -5.621
640 - 680	+0.198 -4.163	+3.368 -3.298	0.236	+3.382 -5.316
680 - 720	+0.155 -3.754	+2.352 -3.247	0.227	+2.368 -4.968
720 - 760	+0.196 -3.842	+3.267 -3.268	0.219	+3.280 -5.049
760 - 800	+0.126 -3.523	+3.366 -3.272	0.212	+3.375 -4.813
800 - 850	+0.110 -3.368	+3.596 -3.261	0.206	+3.604 -4.693
850 - 900	+0.048 -3.351	+3.909 -3.309	0.200	+3.915 -4.714
900 - 950	+0.116 -3.504	+4.148 -3.334	0.196	+4.154 -4.841
950 - 1000	+0.127 -3.511	+4.300 -3.335	0.192	+4.306 -4.846
1000 - 1060	+0.282 -3.683	+4.604 -3.357	0.204	+4.617 -4.988
1060 - 1120	+0.436 -3.779	+3.079 -3.375	0.224	+3.118 -5.071
1120 - 1180	+0.732 -3.982	+5.430 -3.452	0.241	+5.485 -5.276
1180 - 1250	+0.813 -4.031	+5.835 -3.511	0.258	+5.897 -5.352
1250 - 1320	+1.303 -4.414	+6.626 -3.591	0.275	+6.759 -5.697
1320 - 1390	+1.403 -4.471	+7.036 -3.659	0.290	+7.180 -5.785
1390 - 1460	+1.564 -4.590	+7.657 -3.778	0.304	+7.822 -5.953
1460 - 1530	+1.765 -4.738	+8.438 -3.853	0.316	+8.626 -6.115
1530 - 1600	+2.040 -4.972	+9.306 -3.962	0.328	+9.532 -6.366
1600 - 1680	+2.313 -5.179	+10.381 -4.075	0.339	+10.641 -6.599